UiO : Department of Physics
University of Oslo

Influence of Mn Stoichiometry on the Structure and Thermoelectric Properties of $CaMn_{1+y}O_{3\pm\delta}$

Monika Løberg

Master's Thesis, Spring 2017

Abstract

The energy consumption of present day society is ever increasing and the sources for more and cleaner energy is sought for. A possible contributor are thermoelectric generators, which convert parts of a heat flux directly into electrical energy. Unfortunately, the efficiency of current generators is too low for large scale commercialization, and new and better materials must be designed.

In the present master project, the performance of n-type thermoelectric oxide $CaMn_{1+y}O_{3\pm\delta}$ is attempted improved by creating precipitates within the nano-range. The precipitates could be anticipated to enhance phonon scattering, thereby lowering thermal conductivity and enhance the overall thermoelectric properties of the material. A sample series of $CaMn_{1+y}O_{3\pm\delta}$, with composition y = 0, 0.020 , 0.036, 0.074 and 0.10, has been synthesised by solid state reaction and the microstructure and thermoelectric properties were characterized.

Secondary phase, $CaMn_2O_4$, precipitates were found from X-ray diffraction and Scanning Electron Microscopy in the size range 5-10 µm. Further investigations into the presence of nano-precipitates were performed by Transmission Electron Microscopy finding no areas enriched in manganese within the $CaMnO_3$ matrix. Electrical resistivity and Seebeck coefficient were measured from room temperature up to 600°C finding a resistivity ranging from 20 - 100 mOhm cm and Seebeck coefficient from -300 to -200 μVK^{-1}, showing no trend with manganese content. Thermal conductivity measurements were performed, showing a thermal conductivity between 2.3 - 3.6 $Wm^{-1}K^{-1}$, however no trend with varying manganese content was observed. Further, the obtained thermoelectric data was compared with samples fabricated using a different synthesis method, yielding similar results and no significant variations was observed. The absence of a Mn-dependency in all transport parameters was carefully confirmed by a thorough investigation of potential experimental influences, like sample porosity, impurity level and measurement uncertainty. Finally, the results are qualitatively rationalized using a simple Callaway model for the thermal conductivity.

The concluding remarks are that all manganese excess will manifest as secondary phase $CaMn_2O_4$ and no manganese rich precipitates will exist within the $CaMnO_3$ matrix. The variation in manganese content does not influence the thermoelectric properties of $CaMn_{1+y}O_{3\pm\delta}$.

Acknowledgements

This thesis is submitted as a part of the masters degree in Material Science and Nanotechnology by the Department of Physics at the University of Oslo. The project has been performed in the research group Structure Physics from August 2015 to May 2017.

Firstly I would like to express my gratitude to my three supervisors, Anette E. Gunnæs, Kjell Wiik and Matthias Schrade for invaluable guidance and encouragement. Furthermore I would like to thank Phoung D. Nguyen, Domas Birenis, Øystein Prytz, Patricia Carvalho and Annett Thøgersen for their teaching and advice.

This master project has been part of the national coordinated THELMA project, and I would like to thank its members for rewarding discussion and valuable input, especially Sathya Prakash Singh, Nicola Kanas, Temesgen Debelo Desissa and Truls Norby. I would also like to thank Anna Siemiatkowska and Sandeep Gorantla at Wroclaw Research Centre EIT+ for collaborations and help with FIB sample preparations.

A very special thanks is given to the very special members of the Structure Physics group for all laughter, cheering and coffee breaks, and to the members of MENA class of 2013. You have made these years memorable.

And as always, thanks to my family, to my mom and my Børre for always rooting for me. To my dad who taught me to be curious and creative. To my brother and sister, my biggest role models. To all my friends who have been patient and encouraging. And to my dear Sondre, for believing I can do more than I can, and for always supporting me. Kjære, du er mitt eventyr.

Contents

Chapter 1

Introduction

The energy consumption of present day society is ever increasing and the need to find a more environmentally friendly way of transforming energy is desired. In all power production and in many industrial processes as much as 2/3 of the energy is lost as heat [1, 2]. If the energy lost as heat could be harvested and recovered, the efficiency of power production would increase, which would benefit the industry and make a huge positive impact on the environment [3].
This is possible using thermoelectric generators which convert heat directly into electricity without any moving parts or harmful emissions. This makes thermoelectric generators great contributors to meeting the modern societies wants and needs for more and cleaner energy.

1.1 The Thermoelectric phenomena

The thermoelectric phenomena are the conversion of heat and voltage, and are described by three reversible effects, the Seebeck, Peltier, and Thomson effect. In addition related phenomena arises when a magnetic field is present, known as the Nernst and Ettingshausen effect. Transport of charge and heat also induce irreversible effects, such as Joule heating, resistive heating caused by current flow, and *thermal conduction*, the flow of heat in a temperature gradient.

1.1.1 The Seebeck effect

In 1821 the German scientist Thomas Johann Seebeck found that a compass needle was deflected when placed near a closed loop of two dissimilar conductors kept at different temperatures [4] implying the presence of an electric current inducing a magnetic field. When a thermoelectric material is placed under a temperature gradient some the free charge carriers at the hot end will diffuse to the colder side, hence induce a voltage difference over the sample, illustrated in figure (1.1). This phenomena is known as the *Seebeck effect*.

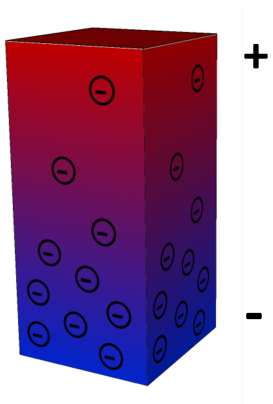

Figure 1.1: Illustration of distribution of charge in a thermoelectric material placed in a temperature gradient, ΔT, inducing a voltage, ΔV, across the sample.

The magnitude of the induced voltage in a given temperature gradient is a material property and named the Seebeck coefficient of the material.

$$\alpha = \frac{\Delta U}{\Delta T} \tag{1.1}$$

Where α is the Seebeck coefficient, ΔT the temperature difference and ΔU the induced voltage difference.

1.1.2 Peltier effect

When the process is reversed and an electric current is applied, a temperature difference is observed. This is called the *Peltier effect* and was discovered in 1835 by the French physicist Jean Charles Athanase Peltier, 12 years after Seebeck discovered the Seebeck effect [5]. The direction of the current determines whether the heat is liberated or absorbed at which end of the material, and will take the opposite effect if the current is reversed. The amount of heat, ΔQ, is proportional to the electrical current flowing, I, related as

$$\Delta Q = \Pi \, \mathrm{I} \tag{1.2}$$

where Π is the *Peltier coefficient* of the material expressing heat carried per unit charge.

1.1.3 Thomson effect

In 1851 William Thomson Lord Kelvin, related the Seebeck and Peltier effects through temperature, $\Pi = \alpha T$. This was later known as the *Kelvin relation*. Thomson also established the existence of a third thermoelectric effect, *the Thomson effect*. The Thomson effect arises when

a current is applied to a conductor held with ends at different temperatures and is the reversible heating or cooling of the conductor [6]. The rate of heat absorbed or rejected is a response to the loss or gain of energy of the charge carriers moving with or against the temperature flux, respectively. The heat rejected or absorbed is expressed as

$$\Delta Q = \tau I t \Delta T \tag{1.3}$$

where τ is the Thomson coefficient, I the electrical current, ΔT the temperature difference and t the time elapsed.

1.2 Thermoelectric generator

When connecting a p- and n-type thermoelectric material, electrically in series and thermally in parallel, an electric current will flow when placed in a temperature gradient. A module made up of several p- and n-legs are called a thermoelectric generator (TEG).

1.2.1 Efficiency of a thermoelectric generator

Even though thermoelectric generators have great potential, most devices have too low efficiency to be economically competitive. One still find thermoelectric generators in use in installations, where reliability is more important than cost, such as in deep space mission [7].

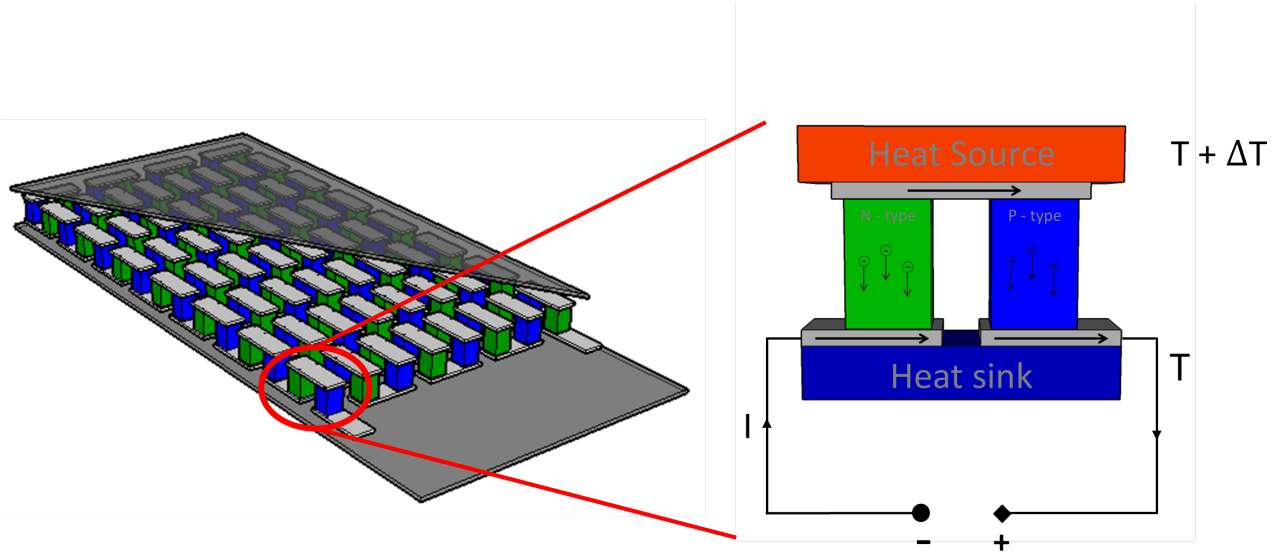

Figure 1.2: An illustration of a thermoelectric generator (left) and a thermoelectric module (right)

However, an improvement of the efficiency is crucial for large scale implementation and commercialisation of thermoelectric generators. The efficiency of a thermoelectric generator is given by [8]

$$\eta = \frac{T_{hot} - T_{cold}}{T_{hot}} \cdot \frac{\sqrt{1 + ZT_{aver}} - 1}{\sqrt{1 + ZT_{aver}} + T_{cold}/T_{hot}} \tag{1.4}$$

where T_{hot}, T_{cold} are the temperature on the hot and cold side and T_{aver} the average temperature. The first term represent the *Carnot efficiency*, while ZT is the *figure-of-merit* of the p-n-couple, a collection of the material properties determining the efficiency of the generator.

1.3 Thermoelectric Figure-of-merit

The thermoelectric figure-of-merit, ZT, is a collection of the material properties determining for the efficiency of a thermoelectric module. Higher values of ZT correspond to more efficient thermoelectric modules. The figure-of-merit for the module as a whole, ZT, can be expressed as an average of the figure-of-merit of the p- and n- type materials individually, zT, expressed as

$$zT = \frac{\alpha^2 \sigma T}{\kappa_l + \kappa_e} \tag{1.5}$$

where α is the Seebeck coefficient and σ the electrical conductivity. The product of these make up the *power factor* of the material, $\alpha^2\sigma$. The nominator describes the thermal conductivity of the material which is a sum of the contributions from lattice vibrations, κ_l, and heat transported by the charge carriers, κ_e.

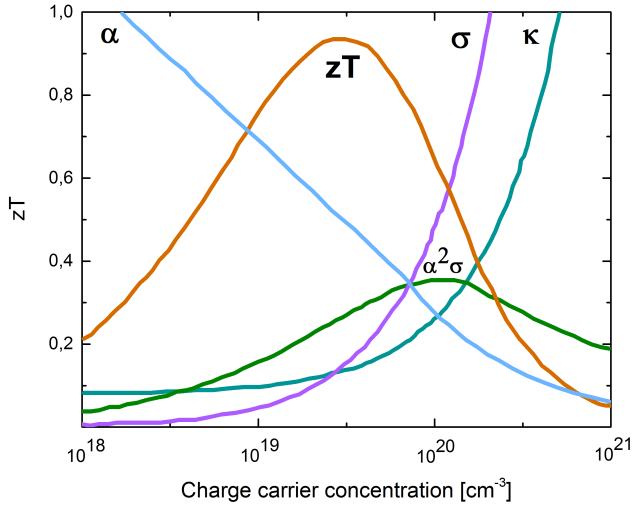

Figure 1.3: zT, α, σ, κ and $\alpha^2\sigma$ as a function of charge carrier concentration, adapted from [9].

High values of zT, reaching 1 and higher, can be obtained by a large thermopower, high electrical conductivity and large Seebeck coefficient together with a low thermal conductivity. These properties are interrelated and changing one will affect the other. This relation between the material properties is illustrated in figure (1.3). While the electrical conductivity, σ, is proportionally related to the carrier concentration, the Seebeck coefficient, α, is inversely proportional, and an increase in electrical conductivity by doping, would decrease the Seebeck coefficient. The overall power factor, $\alpha^2\sigma$, will have a maximum at a certain carrier concentration, estimated to $\sim 10^{20}\,\mathrm{cm}^{-3}$, specific for each material system. In addition, an increase in carrier concentration would increase the electrical contribution to the thermal conductivity, κ_e, lowering the overall figure-of-merit, zT. The electrical conductivity, σ, and the electronic contribution to thermal conductivity from the charge carriers, κ_e, are related through *Wiedemann Franz law* [10]

$$\kappa_e = \sigma L T \tag{1.6}$$

where T is the operating temperature and the proportionally constant L is the *Lorentz number*, often $\mathrm{L} = 2.45{\cdot}10^{-8}\,\mathrm{WK}^{-2}$, but is shown to vary with temperature, carrier concentration and scattering mechanisms [11]. The only property which is not strongly related to the others is the lattice thermal conductivity, κ_l, which in recent year has been thoroughly investigated and attempted lowered by tailoring of crystal structure.

1.4 Thermoelectric materials and strategies of improvement

New thermoelectric materials have been extensively searched for and studied the last 10-15 years and zT of various material system has been reported. A summery published by Chen & Ren, supplemented by Snyder & Toberer, is presented in figure (1.4), showing a selection of studied materials with corresponding zT as a function of temperature [12]. The materials showing the highest zT values, having the most promising TE properties are typically unstable, toxic and/or scarce, such as the conventional materials based heavily on the p-block elements Te, Sb and Pb [13–15]. The search for new materials being applicable at higher temperatures with higher efficiency, in addition to being a more environmentally friendly options has been substantial. Flexible structures which are easily tailored by substitution or void filling such as skutterudites and clathrates have been thoroughly investigated [13–15] showing zT above 1.

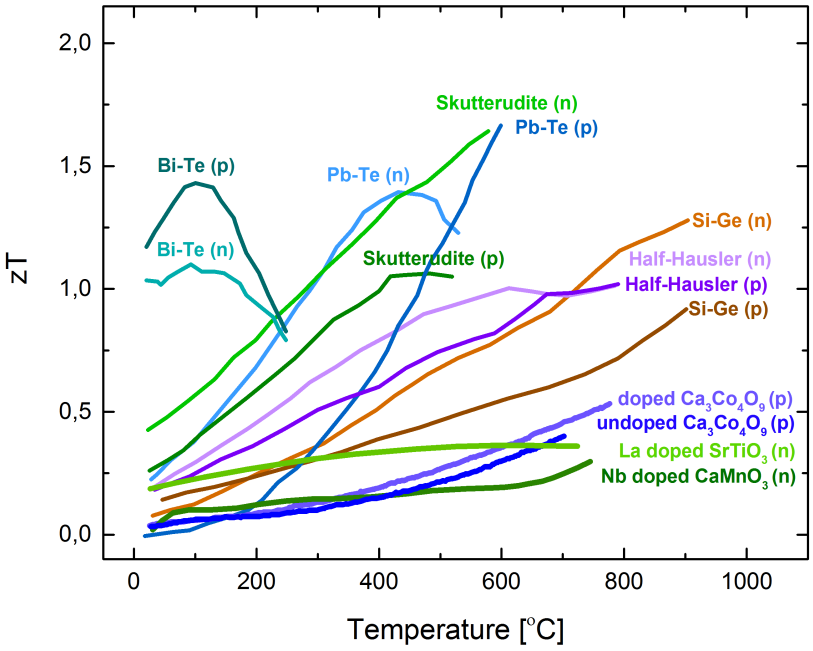

Figure 1.4: zT as a function of temperature for some reported p- and n-type thermoelectric materials, adapted from [9, 12].

Nanostructural approaches with embedding of nanodots, through templating and nanocasting have shown significant improvement of zT [16–19]. For a broader picture of the recent activity in thermoelectric material research the reader is referred to references [9, 15, 20, 21]. By separating the electronic and thermal conductivity into a glasslike thermal, and crystalline like electrical conductivity, known as the phonon-glass electron-crystal approach, the overall thermoelectric properties can be enhanced. This is shown in p-type layered cobalt oxides, such as Na_xCoO_2 and $Ca_3Co_4O_9$, where electronic transport happens in CoO_2 layers while misfit layers of calcium cobalt serve as scattering centres for phonons [22–24].
Thermoelectric oxides were long neglected as potential thermoelectric materials due to the ionic character of their bonding and hence low charge carrier mobility. Also the fairly high thermal conductivity due to strong bonding of light elements presented them as unsuitable. However, in 1997, Terasaki *et al.* reported low resistivity and large Seebeck coefficient in Na_xCoO_2, which led to new interest in oxide based TE-materials [25]. Oxides offer high temperature stability in addition to being cheap, abundant and non-toxic, which are crucial properties to enable large scale commercialization [20, 26–28].

1.4.1 Calcium manganite $CaMnO_3$

Among the most promising n-type oxides is calcium manganite, $CaMnO_3$, attracting attention due to a high Seebeck coefficient and relatively low thermal conductivity. The ideal perovskite is a cubic structure with chemical stoichiometry ABO_3 where A and B are transition metal cations, usually divalent on A-site (A^{+2}) and tetravalent on B-site, (B^{+4}) [29]. The space group is represented by $Pm\bar{3}m$ (221), however symmetry is often reduced by tilting of the BO_6 octahedral resulting in tetragonal (upon cooling) and orthorhombic structures, with space groups $R\bar{3}c$ (167) and Pnma (62) respectively [29].

Below $\sim 700\,^{\circ}C$ the material is stable as orthorhombic structure [30]. Upon cooling, the transition from cubic to orthorhombic structure will happen by elongation of one of the unit cell axis. This is illustrated in figure (1.5), where the low temperature, green unit cell is elongated in b-axis direction, relative to the high temperature, cubic, blue unit cell. The direction of elongation from the cubic cell is arbitrary, which might result in additional distortion and the creation of small areas with different but related orientation. The electrical conductivity of $CaMnO_3$ is fairly low, but tunable by doping on both A- and B-site [30–36]. Reported values of zT show for 10 at% La doped on A-site, $zT = \sim 0.13$, and for 4 at% W substituted on B-site, $zT = \sim 0.18$, reported by Thiel *et al.* [34]. Kabir *et al.* also reported zT for W 1 at% and 5 at% substituted on B-site with $zT = \sim 0.14$ and $zT = \sim 0.11$ at 1070 K, respectively. However, the zT values reported by Kabir *et al.* were corrected for porosity for the thermal conductivity, which might show to be crucial when comparing samples. Recent studies showing Nb-doped $CaMnO_3$ with zT of 0.32 at 1070K [35]. Doping of $CaMnO_3$ has also shown to lower the thermal conductivity due to mass-disorder scattering [36, 37].

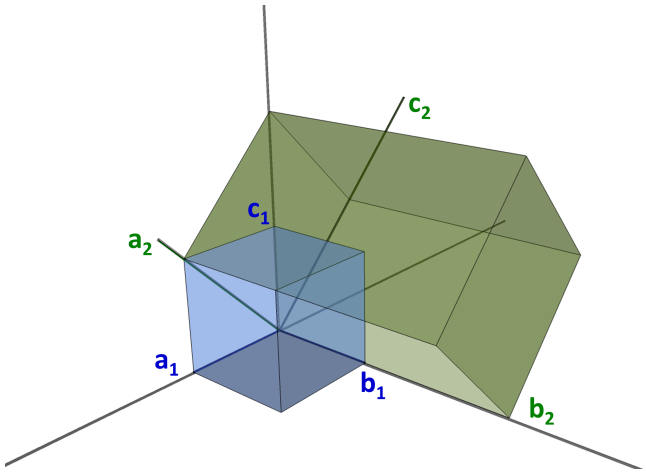

Figure 1.5: Illustration of the relation between high temperature cubic and low temperature orthorhombic structure.

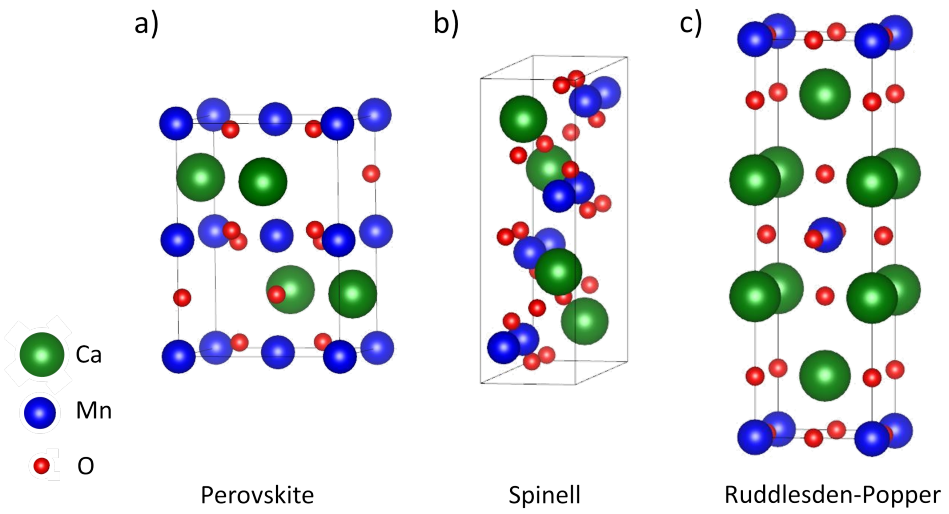

Figure 1.6: Illustration of a a) Perovskite, b) Spinel and c) Ruddlesden-Popper structure where green sphere is Ca, blue is Mn and red is O.

$CaMnO_3$ is also known to have largely varied oxygen content over broad atmospheres [38], but also forming significant levels of oxygen vacancies in air [30]. Thus the material has been investigated as cathode in solid state fuel cells and oxygen storage material, membrane reactor and gas sensors [39–42]. The defect chemistry of $CaMnO_{3\pm\delta}$ has been proposed by Goldyreva *et al.*, showing oxygen vacancies leading to compensation by electronic defects and hence an increase in electrical conductivity [43]. Transport properties has been reported to be be dominated by small polaron hopping [38], with activation energies of 0.21 eV to 0.12 eV with oxygen nonstrochiometry, δ, ranging from 0.14 to 0.03. A structural change to another space group is first observed when δ approaches 0.5 [44].

To further enhance zT of $CaMnO_3$, efforts have been made to lower the thermal conductivity by promoting scattering centres for phonons by tailoring the structure. The focus on layered structure variants has shown reduction in thermal conductivity in similar materials [37, 45, 46]. Also implementing nano inclusions and nano-precipitates has been reported to significantly reduce the thermal conductivity in several material systems [47–50].

From the phase diagram, Appendix A, one might expect precipitation of secondary phase, $Ca_4Mn_3O_{10}$, for Mn deficient samples and $CaMn_2O_4$, for Mn rich samples. Ruddlesden Popper phase, $Ca_4Mn_3O_{10}$, figure (1.6) c), can be viewed as a layered perovskite $(CaO)(CaMnO_3)_n$ where n denotes the number of perovskite unit cells between CaO layers, yielding individual space groups for the different n [29, 46, 51]. Samples with Mn excess are predicted to take the spinel phase, $CaMn_2O_4$, figure (1.6) b), which has a tetragonal structure with space group Pbcm (57) [29, 52]. Crystal data of $CaMnO_3$ and $CaMn_2O_4$ are presented in Appendix B and C, respectively.

1.5 Motivation for project

Even though $CaMnO_3$ is among the most promising n-type thermoelectric oxides, with zT reaching $\sim$0.3, the performance of the material must be further enhanced to enable commercialisation. In this project varying the Mn stoichiometry for $CaMn_{1+y}O_{3\pm\delta}$ with $0 < y < 7.47$ to promote nano-precipitates to lower the thermal conductivity is attempted. Two different synthesis routes have been applied to investigate the influence on microstructure and to investigate if Mn over-stoichiometry manifest as nano-precipitates inside the host phase. Small grains of the host lattice and secondary phase precipitates may act as efficient phonon scattering centres, which could reduce the thermal conductivity of the $CaMn_{1+y}O_{3\pm\delta}$ without disturbing the electronic properties.

Chapter 2

Theory

In this chapter the background of principles discussed in this thesis is presented. First a brief introduction to electrical transport and the Seebeck coefficient is given before a couple of defect chemistry considerations are made. Further a presentation of the theory of phonons and thermal conductivity is given, before a background to crystallography, diffraction and electron microscopy are presented.

2.1 Crystallography

Many physical and chemical properties of materials are determined by the arrangement of atoms, the crystal structure, of the material, making crystallography essential to fully understand materials.

The structure of crystalline materials can be described by the smallest repeating element, the crystal basis, fixed to discrete lattice points in arrangement in a vector space. This makes up the crystal lattice and can be represented by one of the 14 *Bravais lattices* which together with the basis defines the unit cell, the building block of the crystal structure. The lattice can be expressed as follows

$$\mathbf{T} = u\mathbf{a} + v\mathbf{b} + w\mathbf{c} \tag{2.1}$$

where $\mathbf{a}$, $\mathbf{b}$ and $\mathbf{c}$ are the *basis vectors* and u, v and w integers. The volume spanned by $\mathbf{a}$, $\mathbf{b}$ and $\mathbf{c}$ defines the unit cell of the lattice with edge lengths a, b and c which together with the angles between them give the unit cell parameters of the crystal system. The internal symmetry of the crystal can be described by combination of axes of rotation and mirror planes which intersect at a point within the unit cell. The total of 32 possible combination of symmetry elements make up the point group of crystals which when combined with the symmetry of the lattice yields 230 distinctive symmetry groups, called space groups. Every crystal structure has one space group

giving a precise description of the crystal structure of the material.

2.1.1 Reciprocal space

The crystal is invariant under translation, $\mathbf{T}$, of the basis to all lattice points, expressed by equation (2.1). So are the physical properties such as electron number density, $n(r)$, where n is a periodic function with periods $\mathbf{a}, \mathbf{b}$ and $\mathbf{c}$ yielding that $n(\mathbf{r}+\mathbf{T}) = n(\mathbf{r})$. Performing a Fourier analysis, equation (2.2), is often convenient due to access of the properties related to the Fourier components of the analysis.

$$n(\mathbf{r}) = \sum_{g} n_{\mathbf{g}} \exp(i2\pi\mathbf{g}\cdot\mathbf{r}) \tag{2.2}$$

giving the allowed reciprocal vectors, $\mathbf{g}$, under the translation $\mathbf{T}$, representing lattice points in reciprocal space. The reciprocal lattice vector, $\mathbf{g}$, is defined as

$$\mathbf{g} = h\mathbf{a}^* + k\mathbf{b}^* + l\mathbf{c}^* \tag{2.3}$$

where h, k and l are integers, named *Miller Indices*, and $\mathbf{a}^*$, $\mathbf{b}^*$ and $\mathbf{c}^*$ are the reciprocal basis vectors defined from the real space basis vectors as

$$\mathbf{a}^* = \frac{\mathbf{b}\times\mathbf{c}}{V}, \qquad \mathbf{b}^* = \frac{\mathbf{a}\times\mathbf{c}}{V}, \qquad \mathbf{c}^* = \frac{\mathbf{a}\times\mathbf{b}}{V} \tag{2.4}$$

Where V is the unit cell volume $V = a\cdot(b\times c)$. The dot product of the real and reciprocal basis vectors $a^*\cdot a = b^*\cdot b = c^*\cdot c = 1$ and all others are equal to 0 thus allowing us to relate the reciprocal lattice to the real lattice.

2.1.2 Directions and atomic planes in the crystal

Directions in a unit cell are described by vector notation based on the crystal system and is denoted $[uvw]$. Equivalent directions are denoted $\langle uvw\rangle$. The reciprocal lattice points are equivalent to the the reflections of the crystal planes and the distance between the points equivalent to the interplanar distance. The atomic planes in a crystal are described by the *Miller indices*, h, k and l, referred to when discussing the reciprocal vector $\mathbf{g}$ in the previous section. Equivalent planes are indicated with curly brackets, $\{hkl\}$. The direction which is orthogonal to all other planes is the *Zone Axis (ZA)*.

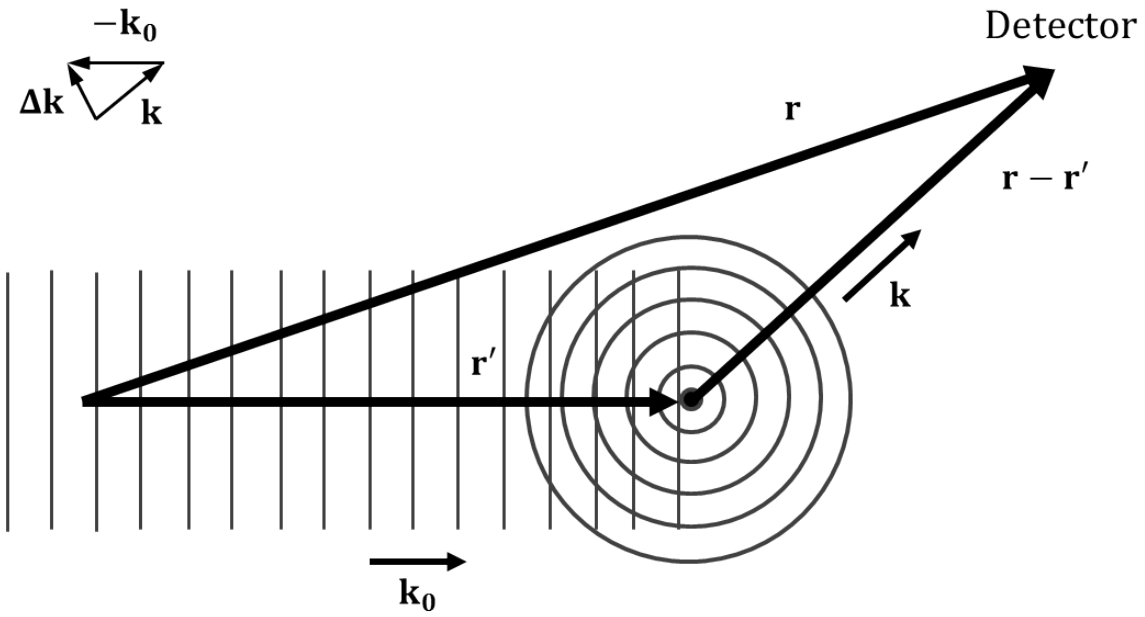

Figure 2.1: Illustration of an elastic scattering event adapted from [53].

2.2 Elastic scattering

In this section an introduction to elastic scattering and diffraction are given. Only the basic concepts are presented and the interested reader is referred to reference [53] for further details. The process of *scattering* describes the interaction between two objects which causes one or both to deviate from their initial trajectory. Scattering processes can be either elastic, with no transfer of energy, or inelastic with transfer of energy. In this thesis two main types of scattering will be discussed, the scattering of phonons, section 2.6.1, and electrons. The theory of both scattering events are based on the same physics, however the focus of this section will be on the elastic scattering of electrons.

An illustration of an elastic scattering event is presented in figure (fig:Elasticscattering2). In the following discussing of an elastic scattering event the following assumptions are made. 1) The electron source is located sufficiently far away from the scattering event, so that the incident wave can be viewed as a plane wave described as

$$\psi_{ins}(k_0, r) = Ae^{2\pi i k_0 r} \tag{2.5}$$

where $\mathbf{k_0}$ is the wave vector of the incident wave, $\mathbf{r}$ is the position of the scattering centre and A is a scaling factor, the amplitude. The second assumption is that 2) the scattered wavelet can be viewed as a spherical wave, described as $\psi(k, r = r')$, and is detected sufficiently far away, at position $\mathbf{r'}$, so that it can be viewed as a plane wave upon detection, with wave vector

k. Further the amplitudes $1/r$ dependency is neglected. The expression for the scattered wave, equation (2.6), is a product of the incident wave at R_j, the scattering strength of the atom, f_j, and the phase factor of the plane wave travelling from R_j to r'.

$$\begin{aligned}\Psi_j(k, r{=}r') &= \Psi(k_0, r{=}R_j) \cdot f_j \cdot e^{2\pi i(r'-R_j)} \\ &= A\, f_j\, e^{2\pi i(k\cdot r')}\, e^{2\pi i \Delta k \cdot R_j}\end{aligned} \tag{2.6}$$

When extending the theory to a crystal, the total scattered wave is a sum of the wavelets from each individual atom in the crystal, expressed as follows

$$\Psi_{scatt}(k, r{=}r') = \sum_{j=0}^{N} A\, f_j\, e^{2\pi i(k\cdot r')}\, e^{2\pi i \Delta k \cdot R_j}. \tag{2.7}$$

By assuming that the detector is located far enough away from them scattering events, all wave vectors can be approximated to equal, and the expression for the scattered wave will simplify to

$$\Psi_{scatt}(k, r{=}r') = C \sum_{j=0}^{N} f_j\, e^{2\pi i \Delta k \cdot R_j}. \tag{2.8}$$

The scattering strength of an atom, *the atomic form factor*, f_j, varies with atomic number, Z, wavelength, λ, and scattering angle, θ. The *Structure factor* of a material is the sum over the contribution from all atoms in the unit cell

$$F(\theta) = C \sum_{j=0}^{N} f_j\, e^{2\pi i \Delta k \cdot R_j} \tag{2.9}$$

2.2.1 Diffraction

Diffraction is the phenomena where the phase relation between elastic scattered waves, from individual atoms in a periodic arrangement, causes strong constructive or destructive interference at specific scattering angles. The concept is equivalent for electron, neutron and X-ray diffraction. Constructive interference occurs under *Laue conditions*, when the wave vector transfer $\mathbf{\Delta k}$ is equal to a reciprocal lattice vector $\mathbf{g}$,

$$\mathbf{\Delta k} = g. \tag{2.10}$$

From the geometry of a scattering process, illustrated in figure (fig:Elasticscattering2), $|\Delta k|$ can be expressed as $|\Delta k| = 2\mathbf{k}\sin\theta$. For elastic scattering $|\mathbf{k_0}| = |\mathbf{k}| = 1/\lambda$ and the inter-planar distance between a family of plane $\{hkl\}$ is thus given as $d_{hkl} = 1/\mathbf{g}_{hkl}$ showing the equivalence

to Bragg's law

$$2d\sin\theta = \lambda n. \tag{2.11}$$

By squaring the structure factor, eq (2.9), the intensity of the reflections from the atomic planes in the crystal, I, can be predicted as follows

$$I = |F_{hkl}(\theta)|^2 = |\sum_{j}^{\infty} f_j(\theta)\exp^{2\pi i(hx_j+ky_j+lz_j)}|^2 \tag{2.12}$$

where *hkl* is the Miller index of the atomic planes being investigated and x_j , y_j and z_j are the atom position in the unit cell. The definition of the structure factor assumes *kinematic conditions*, that the electron is only scattered once when travelling through the sample. This requires thin samples, approximately in the range of the mean free path of the electron, ∼10 nm. When these conditions are not met, the electrons experiences several scattering events, referred to as *dynamic conditions*. Under dynamic conditions, multiple scattering results in observable intensities from reflections which should be extinct according to the structure factor. If more than one grain contribute to the diffraction pattern, additional sets of reflections might be observed.

2.3 Electrical conductivity

In this section a brief introduction to the basic theory of electrical conductivity will be given. The reader is encouraged to study references [10, 54] if a deeper understanding of the concept is desired.

The free electron theory assumes a gas of electrons in a metal, uninfluenced by other electrons and moving freely with random motion. By the realization that electrons can be described as wave and the introduction of quantum mechanics the behaviour of electrons is shown to be quantized by their wave vector and hence their energy, here described in one dimension.

$$E_n = \frac{k^2h^2}{8\pi^2m} \tag{2.13}$$

where E_n is the energy of an electron with wave vector $k = 2\pi/\lambda$ where λ is the electrons wavelength and m the mass of the electron. The number of energy states, $N(E)$, in any particular energy range, dE, for a volume V, gives the *density of states function*

$$N(E) = 2\pi V\big(\frac{8m}{h^2}\big)^{3/2}E^{1/2} \tag{2.14}$$

Similar to the expression for energy (eq (2.13)) the density of states function has a parabolic shape where the number of energy levels and energy states increase with increasing values of k. The energy levels are populated according to the Pauli Exclusion and the Aufbau principle with the highest filled energy state constituting the *Fermi energy*. At temperatures above absolute zero electrons close to the Fermi energy might gain energy and be excited to higher energy states. The statistics describing the distribution of electrons across the different states are called *Fermi-Dirac statistics* and express the probability P that an energy level, E, will be occupied in the *Fermi function* as follows

$$P(E) = \frac{1}{\exp\left(\frac{E-E_F}{k_B T}\right) + 1} \tag{2.15}$$

where E_F is the Fermi energy. For the free electron model it is assumed that the electron moves in constant potential which is not the case for a real crystal where the potential is periodic in compliance with the crystal structure. If the potential is weak or the wave length of the electron is long the wavefunction will be similar as that of a free electron. However, electrons with wavelengths equal to the atomic plane spacings of the structure will be influenced by the periodic potential, occurring at quantized values of the wave number

$$k_{scattered} = \pm\frac{n\pi}{d} \tag{2.16}$$

where n is an integer and d the spacing of atomic planes. This quantification of allowed wave vectors results in forbidden energy intervals and the discontinuities mark the boundaries of the *Brillouin zone*, thus because of the wave vectors dependency upon the electrons velocity and momentum the Brilloiun zone is also often referred to as *velocity* or *momentum space*. The allowed energy levels result in bands of allowed energy intervals, where the occupied and unoccupied bands are referred to as the valence and conduction band, respectively. For metals the two bands overlap, while there for semiconductors are a gap between them, known as the *band gap* of the material. If the band gap exceeds 2 eV the material is regarded as an insulator. When the metal is at normal equilibrium the velocities sum to zero and no net current is flowing. However, when an external force, such as an electric field, $\mathbf{E}$, is applied each electron experience a force, $-e\mathbf{E}$ thus a change in the wave vector $\mathbf{\Delta k}$. The total velocities no longer sum to zero and a current is flowing through the material which could be expressed as

$$I = neAv \tag{2.17}$$

where n is the number of mobile electrons, e the electric charge, A the cross sectional area of the sample and v the drift velocity of the electrons expressed as

$$v = a\tau \tag{2.18}$$

where a is the acceleration of electrons in an electric field, $a = eE/m_e^*$ and τ the *relaxation time*. The relaxation time describes the time between scattering events, further defined as the *mean free path*, the distance between the scattering events divided by the electron velocity at the Fermi energy, v_F, yielding $\tau = \Lambda/v_F$. By substituting the expression for acceleration into equation (2.18) the expression for the drift velocity is obtained

$$v = \frac{eE\tau}{m_e^*} \tag{2.19}$$

with the expression for the total current

$$I = \frac{ne^2AE\tau}{m_e^*} \tag{2.20}$$

and by applying *Ohms law* one obtains an expression for the resistivity and thus the conductivity

$$\frac{1}{\rho} = \sigma = \frac{ne^2\tau}{m_e^*} \tag{2.21}$$

The velocity gained by the electrons in an electric field is often expressed in terms of the mobility of the electrons

$$v = \mu E \tag{2.22}$$

and by comparing to the drift velocity expressed in equation (2.19) the drift mobility is

$$\mu = \frac{e\tau}{m_e^*} \tag{2.23}$$

where the conductivity and mobility for electrons then relates as follows

$$\sigma = ne\mu_e \tag{2.24}$$

2.3.1 Transport via localised states

The transport mechanism described so far considers only idealised transport, where charge carriers move itinerantly within bands and scattered back to equilibrium within a scattering time τ. This is not the case for polar solids, solids with ionic character to their bonding. In polar solids the charge carriers will interact with the lattice as it moves through the solid, causing localized deformations. This is illustrated in figure (2.2).
The charge carrier together with the deformation that follows, the electron-phonon interaction, can be treated as a quasi-particle named a *polaron*. If the electron-phonon interaction is week, the deformation is distributed over a significant volume in the crystal, the polaron is a large polaron, and is treated theoretically as a regular band electron with increased effective mass m^*. If the interaction is strong, the potential caused by the deformation might trap the charge carrier, requiring additional activation energy for it to move to the next localized state. This is called *thermally activated hopping conduction* between localized states. In this case the mobility of a carrier can be expressed as [55]

$$\mu(T) = \frac{\mu_0}{T} \exp(-\frac{E_a}{k_B T}) \tag{2.25}$$

where E_a is the activation energy for hopping, k_B the Boltzmann constant and T the temperature. By assuming that the mobility is independent on the defect concentrations, a plot of $\log(\sigma T)$ versus inverse temperature in K, with constant atmosphere, yields a straight line relationship. This type of plot is called an *Arrhenius plot* where the intercept is equal to $\log(\mu_0)$, and the activation energy,E_a, can be extracted from the slope, giving useful information about the nature of conductivity in the material.

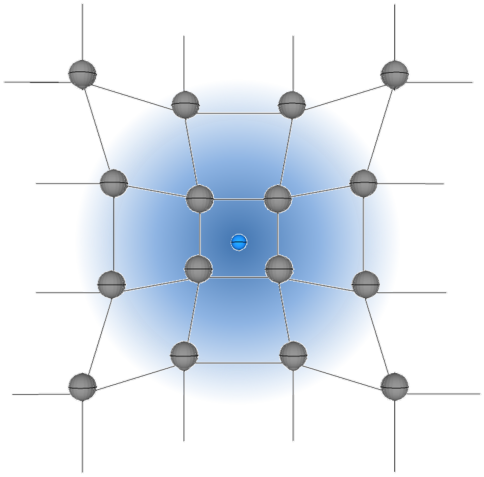

Figure 2.2: Illustration of a polaron with lattice distortions as the electron moves through the lattice.

2.4 Seebeck coefficient

The thermoelectric effects like the Seebeck, Peltier and Thompson effect express the relation between the flow of heat and current linked through the Kelvin relations. The kinetic energies and therefore the velocities of the electrons near the Fermi energy in the hot end will be greater than the electrons in the cold, resulting in a net diffusion of charge carriers towards the cold causing a voltage difference over the sample. Assuming weak electron-electron and electron-phonon interaction, the Seebeck coefficient for electrons and holes in semiconductors can be expressed as, respectively, [54]

$$\alpha_e = \left(\frac{k_B}{e}\right)\left[5/2 \ln\left(\frac{N_c}{n}\right) + a_e\right] \tag{2.26}$$

$$\alpha_h = \left(\frac{k_B}{e}\right)\left[5/2 \ln\left(\frac{N_v}{p}\right) + a_h\right] \tag{2.27}$$

Where N_c and N_v are the density of states for the conduction and valence band, respectively, k_B is the Boltzmann constant and n and p are the concentration of mobile electron and holes respectively. The correction terms a_e and a_h take into account thermal resistivity due to various scattering events.

The sign and magnitude of the Seebeck coefficient provide useful information of the material. If the Seebeck coefficient is negative the dominant charge carriers are electrons and if it is positive the dominant charge carriers are holes. The Seebeck coefficient is inversely related to the carrier concentration, thus the absolute Seebeck coefficient will be lower for higher concentrations of electrons or holes. By assuming high temperatures and estimating the entropy of the system, an expression for the charge carrier concentration might be derived [54]. This relation is known as *Heikes formula*,

$$\alpha = -\frac{k_B}{e} \cdot \ln\left(\frac{1-c}{c}\right), \tag{2.28}$$

where c is the fraction of defects. The Seebeck coefficient is sensitive to the change in carrier concentrations and might be a strong tool for estimating changes in carrier concentration upon doping of materials.

2.5 Defect chemistry

This chapter is written on the basis of the theory presented in lectures and lecture notes of "Defects and Transport in Crystalline Materials" by Truls Norby [55].
In crystalline materials, atoms are arranged periodically, repeated in every directions. However there might always be deviations from this perfect arrangement, called *defects*, influencing the functional and mechanical properties of materials. Defects are fundamental for the diffusion of atoms and ions, due to a perfect crystal not inhabiting long range transport. Understanding and control of defects and defect concentrations in materials are therefore essential when designing functional materials. The classification of defects are done with basis in their dimension, as follows.

- Zero dimension defects limited to one lattice point: vacancies, interstitials, substitutions and electronic defects.
- One dimensional defects: dislocation, row of vacancies and line precipitations.
- Two dimensional defects, planar defects: surfaces, grain boundaries and stacking faults.
- Three dimensional defects often referred to as volume defects: precipitates, cracks and foreign inclusions.

When writing defect reactions three laws of conservation must be met. 1) Conservation of mass, hence the number and types of atoms must be the same before and after the reaction, 2) Conservation of charge, with the perfect lattice as a reference and 3) conservation of ratio of structural sites, the ratio of anion to cation sites must be constant. Thus upon creation of new defects or structural sites, the change in mass, charge or structural sites must be compensated by another defects such as interstitials, vacancies and/or electronic defects.

Kröger-Vink notation

Several notations for describing defects exist, the one used throughout this thesis will be the Kröger-Vink notation, described by Kröger and Vink in 1956 [56]. The general notation is A_s^c where A is the chemical specie, s the site relative to the host structure and c is the effective charge of the defect, the sites original charge subtracted by the real charge of the defect. A positive charge is denoted "$\bullet$", a negative charge " $'$ " and a neutral charge "x". A vacancy is represented with a v instead of a chemical symbol and a interstitial element will be subscripted with an i instead of the related structural site.

2.5.1 Defects in $CaMnO_3$

A defect chemistry model for $CaMnO_3$ is presented by Goldyreva *et al.* [43]. Two origins of charge carriers are reported 1) formation of oxygen vacancies compensated by (localised) electrons, eq (2.29), and 2) intrinsic ionisation, thermal excitation of electrons across the band gap, eq (2.30).

$$O_O^x + 2Mn_{Mn}^x = \frac{1}{2}O_2(g) + v_O^{\bullet\bullet} + 2Mn'_{Mn} \tag{2.29}$$

$$2Mn_{Mn}^x = Mn'_{Mn} + Mn_{Mn}^{\bullet} \tag{2.30}$$

By evaluating the concentration of intrinsic charge carriers from electron band structure model, eq (2.30),

$$n = p = (K_i')^{1/2} = \sqrt{N_C N_V}\exp(-E_g/2RT) \tag{2.31}$$

an n = 0.02 - 0.03 at 1000-1200 K with $E_g = 0.7eV$ if obtained, which corresponds to an oxygen loss $\delta = 0.03$. The charge carriers compensating the oxygen vacancy concentration are then estimated as $n = 2\delta \sim 0.06$ [43, 57]. The excitation of charge carriers corresponds to the transition of electrons for half filled t_{g2} to e_g of Mn^{4+} so that all charged states of Mn, Mn^{3+} (Mn'_{Mn}), Mn^{4+} (Mn_{Mn}^x) and Mn^{5+} ($Mn_{Mn}^{\bullet}$) occur at equilibrium.

Dislocations One dimensional linear defects where some of the atoms are misaligned, are named *dislocations* and cause lattice distortion in their vicinity. A plane of atoms, which terminates within the crystal is called an *edge dislocation*. Whereas when a whole area of a crystal is shifted one atomic distance relative to another area, the dislocation is termed a *screw dislocation*. Dislocations are seldom pure edge or screw but a mix of the two, named *mixed dislocations*, and the lattice distortion associated with it a combination. The direction and magnitude of the lattice distortion is expressed by a *Burgers vector* denoted **b**.

Grain boundaries Interfaces separating regions in the material such as external interfaces, grain boundaries, phase boundaries or stacking faults can be viewed as two dimensional defects. These regions will have various degrees of crystallographic misalignment. *Low angle grain boundaries* can be described in terms of dislocation arrays, where aligned edge dislocations result in *tilt boundary* with an orientation angle θ. Aligned screw dislocation results in *twist boundaries* with an orientation parallel to the boundary. Grain boundaries with mirror plane lattice symmetry occurs in defined crystallographic planes and directions, and are named *twin boundaries*. *Stacking faults* are found where the repeating structure is interrupted by an extra close packed plane in the stacking sequence of the structure. Associated with each of these two-dimensional defects are interfacial energies, affecting the properties of the material.

2.6 Thermal conductivity

In this section a brief introduction to thermal conductivity and the theory of phonon and phonon scattering will be given. The basic solid state physics is found in any introductory solid state physics book, here mainly referred to reference [10, 54, 58].
Thermal conductivity is the transport of thermal energy from one place to another in response to a temperature gradient. Transport of heat occurs in three ways 1) convection, 2) conduction and 3) radiation, and an objects ability to carry heat is termed the thermal conductivity of the matter. Heat can also be transported through a material in a response to an external force, such as the electric field in the thermoelectric effect, the Peltier effect. In general, heat transport in solids appears only by conduction and can be described by *Fourier's law* under steady state conditions as [59]

$$j_x = -\kappa \frac{dT}{dx} \tag{2.32}$$

where j_u is the flux of thermal energy, κ the thermal conductivity and dT/dx the temperature gradient through the material. The minus sign defines a positive heat flow in the direction of decreasing temperature. Heat conduction in solids is composed of different contributions, such as motion of charge carriers, transfer of energy between vibrating adjacent atoms, electromagnetic waves, spin waves or other excitations. The total thermal conductivity can be written as as sum of its components

$$\kappa_{tot} = \sum_i \kappa_i \tag{2.33}$$

where i is the excitation mechanism. Even though the magnitude and temperature dependency varies largely between materials, mainly due to structure complexity, lattice imperfections, grain size and anisotropic lattice forces, some general tendencies are recognizable. For materials with many charge carriers, such as metals, the significant contributions is from the motion of free electrons. Even though the motion of electrons is random, energized electrons will transfer excess energy to nearby electrons by collision, and the thermal energy will be distributed through the material. In materials with a high concentration of charge carriers, such as metals, most of the heat is transported by the charge carriers. Whereas in materials with a low concentration of charge carriers, such as semiconductors and insulators, the majority of the heat is transported by lattice vibrations.

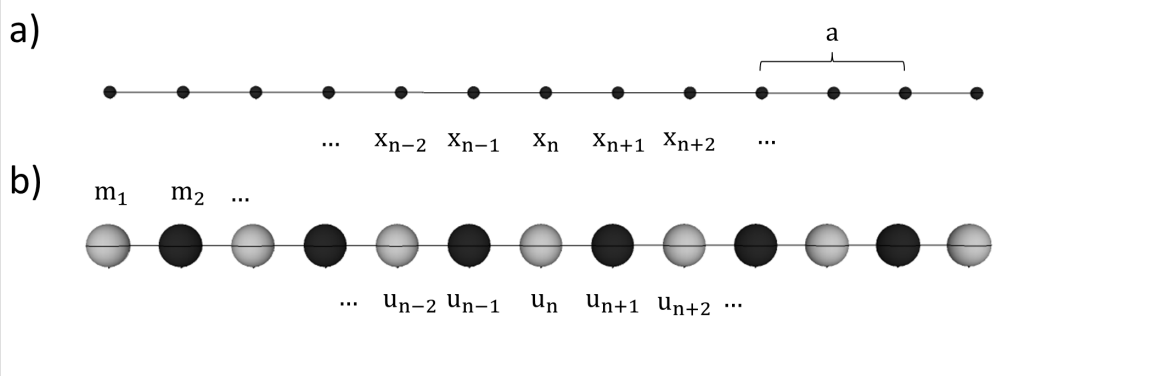

Figure 2.3: Illustration of a one dimensional atom chain.

2.6.1 Phonons

The quantum of the lattice vibrations is termed a *phonon* derived from the Greek word "$\phi\omega\nu\acute{\eta}$ translating to sound or voice. A phonon is a quasi particle of collectively excited atoms or molecules. Atoms vibrates about their equilibrium position to smaller or lager extent. The magnitude of the vibration is strongly dependant on their energy, mainly decided by the temperature, but strongly coupled to the nature and motion of their neighbouring atoms.

2.6.2 Phonon mechanical properties

The vibrational motion of the atoms around their equilibrium position can be viewed by a simple model as balls on springs, considered as harmonic oscillators with ground state energy and vibration. A one dimensional crystal lattice of similar atoms is illustrated in figure (2.3), with similar mass, $m_1 = m_2$, positioned at x_n, with atomic distance, a. The forces acting on the n-th atom can be described by an extension of *Hooke's law*, $F = Cu_n$, where u_n is the displacement of atom n, and C is the spring constant of their bonding. The force acting on the atom is then described by the difference in displacement u between atom n and it's neighbours u_{n+1} and u_{n-1} as follows

$$F_n = C(u_{n+1} - u_n) + C(u_{n-1} - u_n). \tag{2.34}$$

The displacement can then be described by plane waves for a harmonic oscillator

$$u_n = u_0 e^{i(qx_n - \omega t)} \tag{2.35}$$

where q is the phonon wave vector, ω is the vibrational frequency and t gives the time dependency. The allowed wave vectors are then given by the discrete wave vectors as follows [10]

$$q = \frac{2\pi}{N} n_i \qquad \text{where} \quad n_i = 0, \pm 1, \pm 2, \pm 3, \ldots \tag{2.36}$$

where N is the number of atoms in the crystal and n_i is an integer. The total number of phonon modes are equal to the number of atoms in the unit cell, times the number of atoms in the crystal in three dimensions. Translational symmetry allows all possible modes to be described within the first Billouin zone yielding the boundary conditions for q $[-\pi/a, \pi/a]$. Applying Newtons second law to equation (2.34) for the motion of the n-th atom, by the expression for acceleration $a = d^2u_n/dt^2$, and equation (2.35), we obtain

$$-m\omega^2 = c(e^{iqa} + e^{-iqa} - 2) \tag{2.37}$$

$$-m\omega^2 = c(-2 + 2\cos(qa)) = -4c\sin^2\left(\frac{qa}{2}\right) \tag{2.38}$$

The displacement terms u_n cancel each other out, subsequently also does the time dependency. Through this relation we obtain the dispersion relation of phonons, by inserting $\omega_0 = \sqrt{\frac{4C}{m}}$, as

$$\omega(q) = \omega_0 \left|\sin\left(\frac{qa}{2}\right)\right| \tag{2.39}$$

revealing the dispersion relations illustrated in figure (2.4) a). The sinusoidal have a periodicity when increasing the wave vector q by $2\pi/a$; therefore, the phonon dispersion can be described in the interval of $-\pi/a \leq q \leq \pi/a$.

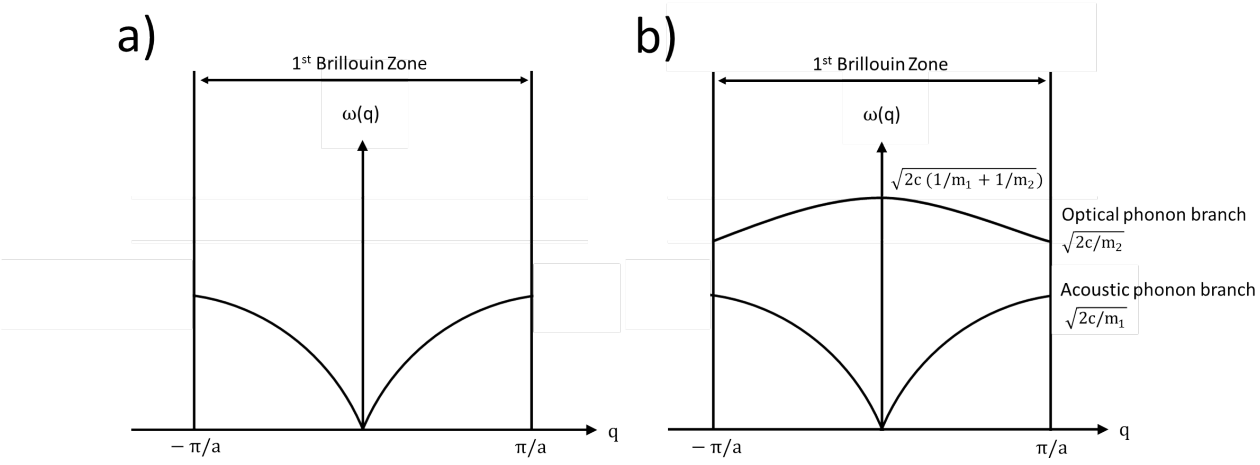

Figure 2.4: Illustration of the dispersion relation of acoustical and optical phonons.

When introducing a diatomic lattice in one dimension where the atoms have different mass or charge, illustrated in figure (2.3) with unequal mass $m_1 \neq m_2$, two displacement expressions exist. By the same approach as for a monoatomic lattice the dispersion relation for the diatomic lattice is obtained as follows

$$\omega^2 = c\Big[\frac{1}{m_1} + \frac{1}{m_2} \pm \sqrt{\Big(\frac{1}{m_1} + \frac{1}{m_2}\Big)^2 \frac{4}{m_1 m_2} sin^2 \frac{qa}{2})}\Big] \tag{2.40}$$

The boundary conditions are then given as

$$\omega = \begin{cases} \sqrt{2c/m_2} \\ \sqrt{2c/m_1}. \end{cases} \tag{2.41}$$

whereas when q approches zero the phonon frequency approches

$$\omega \to \begin{cases} \sqrt{2c\,(1/m_1 + 1/m_2)} \\ 0. \end{cases} \tag{2.42}$$

The dispersion relation for a diatomic lattice is illustrated in figure (2.4) b), now showing two bands, where the modes existing in the lower frequency branch are named *acoustic vibrations* or *acoustic phonons* and the higher *optical vibrations* or *optical phonons*. For the acoustic phonon all the atoms vibrates in phase with the same amplitude and direction, as in an acoustic sound wave, illustrated in figure (2.5 (a)). For an optical phonon, neighbouring atoms vibrates in opposite phase, illustrated in figure (2.5 (b)), the lighter atom vibrates with a larger amplitude so that the over all mass distortion is zero.

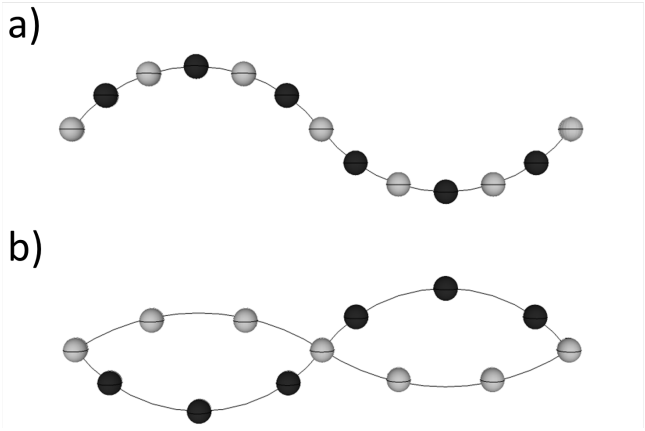

Figure 2.5: Illustration of a 1D a) acoustic phonon and b) optical phonon wave.

Atoms moving in phase result in low frequency acoustic phonons and will carry the most amount of heat, whilst atoms moving in opposite phase yields high-frequency optical phonons carrying less heat. The reason optical phonons carry little heat is due to their low group velocities. However, they do affect the heat conduction by interacting with other phonons. In more complex unit cells, the phonon branches will also be more complex, and a common simplification through the Debye model is often applied. While Einstein in 1906 [60] described the vibration of atoms as isolated harmonic oscillators vibrating at the same frequency, Debye proposed an improvement to the model, in 1912, by including the interactions between the vibrating atoms [10,61] yielding a linear and isotropic phonon dispersion. To describe the heat carried by phonons, and hence the thermal conductivity, the heat capacity, introduced in the next section, must be included.

2.6.3 Heat capacity

The heat capacity of a material is described as the amount of energy, δQ, needed to change the temperature of something by δT. The heat capacity is generally expressed as

$$C = \frac{\Delta Q}{\Delta T} \tag{2.43}$$

The *Dulong-Petit law*, developed form experiments, states that the specific heat capacity under constant volume is equal to $3k_B$/atom, displaying good agreement with experiments at high temperature but revealed to be failing at lower. By introducing quantum mechanics Einstein described in 1906 the thermal vibration as isolated harmonic oscillator vibrating at the same frequency, a model later improved by Debye [10, 60, 61]. The background for the Debye approximation is derived in Appendix E, but has it basis in introducing the interactions between adjacent atoms. By introducing the *Debye temperature* $\theta_D = \hbar\omega_D/k_B$ and *Debye frequency* $\omega_D = (3N/4\pi V)^{1/3}v_s$, where N/V is the number density, and v_s the speed of sound in the crystal, the Debye model can be expressed as

$$C(x)dx = \frac{3k_B}{2\pi^2 v_s^3}\Big(\frac{k_B}{\hbar}\Big)^3 T^3 \frac{x^4 e^x}{(e^x-1)^2}dx \tag{2.44}$$

where $x = \hbar\omega/k_BT$. The law of Dulong-Petit and the Debye approximation for the heat capacity is illustrated in figure (2.6) revealing a good agreement at high temperatures, with a $3k_B$/atom dependency.

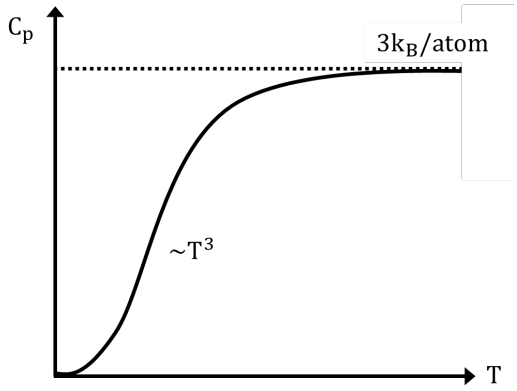

Figure 2.6: Illustration of the heat capacity as a function of temperature by Dulong-Petit law and Debye approximation.

2.6.4 Phonon distribution and heat transport

An investigation into how a crystal stores energy has been made, and it is now time to see how heat is transported. The amount of thermal energy carried by each phonon with wave vector **q** is dependent upon its frequency, ω_q, and group velocity, v_g, related as $v_g = \omega_q/dq$. The functional relation between the frequency and wave vector for each branch, v_g, called the dispersion relation expressed as

$$N_0(\vec{q}) = \frac{1}{\exp(\hbar\omega_{\vec{q}}/k_B T) - 1} \tag{2.45}$$

When the system is disturbed out of its equilibrium distribution, N^0, by added energy, denoted N, scattering events will drive the system back to equilibrium, restoring the phonon distribution to its equilibrium distribution N_0 with a characteristic scattering time τ. This is in analogy with electrical transport described in section 2.3. The rate of change due to scattering processes is expressed by the Boltzmann equation in presence of a temperature gradient as follows

$$\frac{N_{\vec{q}} - N^0_{\vec{q}}}{\tau_q} = -(\vec{v}_g \cdot \vec{\nabla} T)\frac{\delta N^0_{\vec{q}}}{\delta T} \tag{2.46}$$

where N is the distribution function, $\vec{v}_g$ the group velocity and T the temperature. A phonon mode carries heat flux equal to the product of the average phonon energy and group velocity resulting in a total heat flux carried by all phonons can be expressed as

$$\vec{Q} = \sum_{\vec{q}} N_{\vec{q}} \hbar\omega_{\vec{q}} \vec{v}_g \tag{2.47}$$

By relating the heat carried by the phonons, equation (2.47) to the Boltzmann equation, equation (2.46) the lattice thermal conductivity can be derived and expressed as follows

$$\kappa_L = \frac{1}{3}\int_0^{\theta_D/T} C(x)vl(x)dx \tag{2.48}$$

where $x = \hbar\omega/k_BT$ and $l(x)$, the mean free path of the phonon, expressed as $l(x) = v\tau(x)$. The full derivation is found in Appendix F. The temperature dependency of the thermal conductivity is thus determined by the product of the temperature dependence of the specific heat of the material, discussed above, and the group velocity. The group velocity is described by harmonic bonds and assumed to be constant for most solids, no T dependency. The term not yet discussed is the temperature dependency of the mean free path $l(x)$ determined by the temperature dependency of the relaxation time of the system. The total relaxation time is a sum of contributions from several phonon modes and their different scattering events. The total relaxation time can be expressed as a sum of the contribution from the different processes known as *Matthiesen's rule*

$$\tau_q^{-1}(x) = \tau_U^{-1} + \tau_{MD}^{-1} + \tau_B^{-1} + \tau_{EP}^{-1}\ldots \tag{2.49}$$

where τ_U^{-1}, τ_{MD}^{-1}, τ_B^{-1} and τ_{EP}^{-1} is the Umklapp scattering, mass-disorder, boundary and electron-phonon scattering, respectively. Less prominent scattering mechanisms exist, but is beyond the scope of this work, and only the mechanisms mentioned here will be further discussed.

Three phonon interaction

To study the full picture of the thermal conductivity the inclusion of phonon interaction must be made. Phonon interaction is the source of intrinsic thermal resistance and neglecting to include them leads to the description of an infinite thermal conductivity, which is not the case for any solid. Four interaction for a simplified three phonon case exist

(i) excitation of three phonons
(ii) annihilation of three phonons
(iii) creation of one and annihilation of two and
(iv) creation of two and annihilation of one phonon.

Requiring conservation of energy make (i) and (ii) irrelevant when discussing scattering processes. Scattering process (iii) and (iv) are illustrated in figure (2.7).

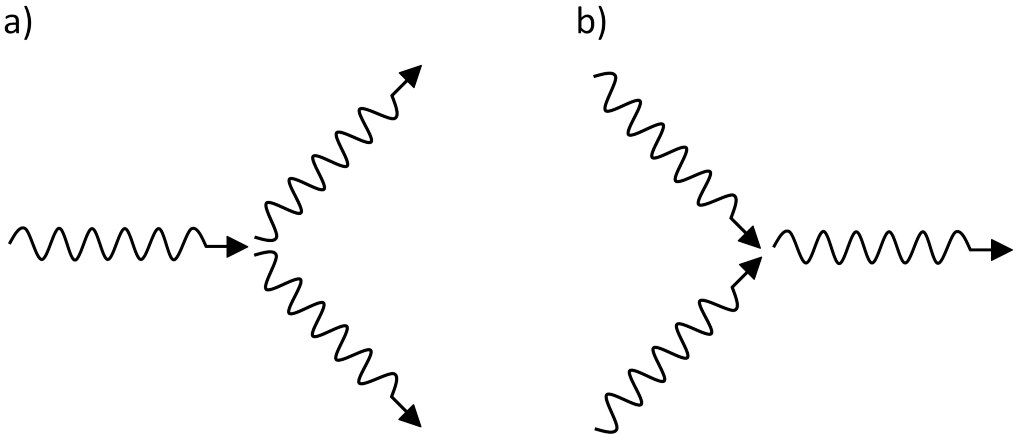

Figure 2.7: Illustration of phonon scattering events where a) one phonon is created by the annihilation of two and b) two phonons are created by annihilation of one

Phonons are considered to be quasi-particles, thus they do not have any momentum or mass. However, phonons do have a line of direction, and their movement in a crystal can be described with a *crystal momentum*, $p = \hbar q$. If a scattering event results in a phonon with wave vector inside the first Brioullion zone, the scattering process is termed *normal* scattering or *N-process* with conserved crystal momentum. If the resulting wave vector terminates outside the first Brioullion zone, it could be described by a wave vector inside the first Brioulloin zone translated back by a reciprocal lattice vector g. Both situations are illustrated in figure (2.8). The latter process is named *Umklapp* scattering, or *U-process*, where the crystal momentum is not conserved but transferred to the lattice. This give rise to thermal resistance.

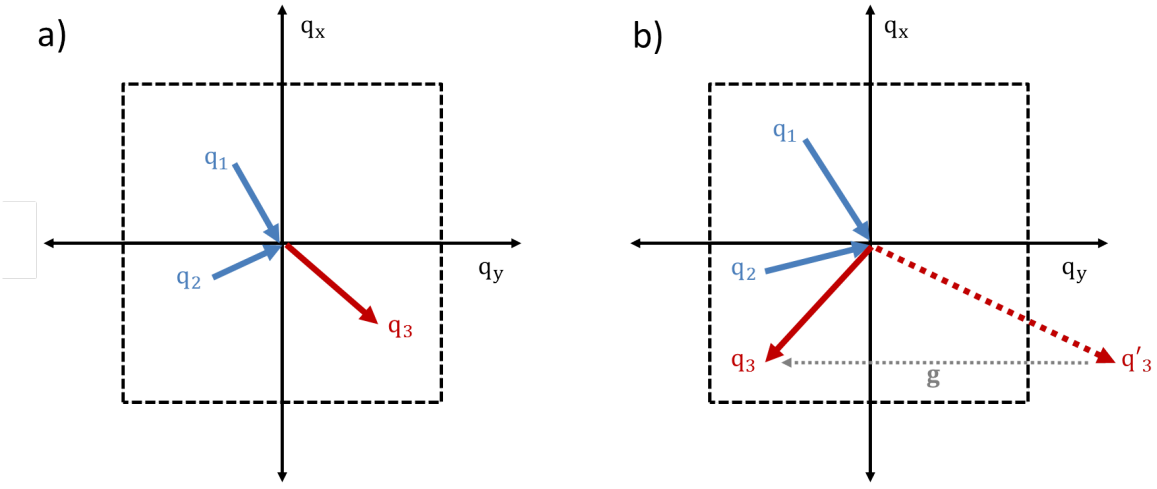

Figure 2.8: Illustration of a a) Normal and b) Umklapp scattering process.

2.6.5 Scattering mechanisms

In this section calculation of relaxation times, $\tau(\omega)$, is presented for different scattering processes to evaluate the total lattice thermal conductivity. Several models for this has been presented in litterature, however, in this work only the Callaway model will be discussed further [62–68].

Umklapp scattering

The relaxation time for anharmonic Umklapp scattering is adapted from the model proposed by Slack *et al.* as

$$\tau_U^{-1}(\omega) = \frac{\hbar\gamma^2 T}{\bar{m} v_s^2 \theta_D}\, exp(-\frac{\theta_D}{3T})\, \omega^2 \tag{2.50}$$

where θ_D is the Debye temperature, $\bar{m}$ the average atomic mass, γ the *Grüneisen parameter* and v_s the speed of sound in the material. The Grüneisen parameter is related to the effect that the volume change with temperature of the crystal lattice has on the vibrational properties [10]. γ is further assumed to be $\gamma = 1$ for the qualitative discussions in this work.

Mass-disorder scattering

The general term mass-disorder scattering covers scattering processes due to lattice point defects such as impurities; being a vacancy, substituted atoms with different mass or charge, or linear defects such as dislocations or nano-precipitates. Following the work of Klemens [69, 70] the relaxation time for point defect scattering can be expressed as

$$\tau_{MD}^{-1} = \frac{V}{4\pi v_s^3}\, (\Gamma_M + \Gamma_S)\, \omega^4 \tag{2.51}$$

where V is the atomic volume, v_s the speed of sound in the material and Γ_M and Γ_S are scattering parameters of mass and strain variance, respectively. The scattering parameters can be described as [70]

$$\Gamma_M = \frac{(\frac{\bar{m}}{\bar{M}})^2 c_i\, (\frac{m_i - \bar{m}}{\bar{m}})^2}{3} \tag{2.52}$$

where, $\bar{m}$ is the average atmoic mass, c_i the relative concentration and m_i the atomic mass on of the defect lattice position. $\bar{M}$ is the average mass over all atoms [62,63,65]. In a similar way the strain variance parameter, Γ_S can be described, replacing the local mass difference, $(m_i - \bar{m})^2$, with the local atomic size difference $[\epsilon\,(r_i - \bar{r})^2]$. Here, ϵ is an empirical material constant. Also the volume of the defect might determined which phonon frequencies are scattered more strongly, and might be a way to target specific phonon frequencies.

Boundary scattering

Phonons might also be scattered at the boundary of the crystal, either at the sample surface or at internal grain boundaries. This is most prominent at lower temperatures where the mean free path of the phonons exceeds the boundary of the crystal, yielding boundary scattering as the dominant scattering mechanism. The model first presented by Casimir in 1938 for the relaxation time of boundary scattering is widely used and accepted in literature as [71]

$$\tau_B^{-1} = v_g L^{-1} \tag{2.53}$$

where v_g is the phonon group velocity, thus frequency dependent, and L the dimension of the crystal. The model is a simple approximation, the relaxation time is only based on the time the phonon uses to move trough a grain.
It is shown that with increasing surface roughness the thermal conductivity is further reduced [72] and a correction factor F is multiplied by the dimension factor, L, of the crystal [73]. However this will not be regarded in this project and F is equal to 1.

Electron-Phonon scattering

Phonons might scatter of mobile charge carriers, known as Electron-Phonon scattering for n-type conductors. Electron-phonon scattering might occur in samples with relatively high carrier concentrations. A simplified expression for the electron-phonon scattering mechanisms was derived from the theory of Ziman [73] as follows

$$\tau_B^{-1} = \frac{E_{def}^2 (m^*)^2 \omega}{2\pi\hbar^3 \rho v_s} \tag{2.54}$$

where m^* is effective mass of an electron and the deformation potential E_{dist}, ω is the phonon frequency and ρ the density of the structure.

2.6.6 Electronic contribution to the thermal conductivity

Electrons moving in a potential will also carry heat. By considering an electron gas and the Fermi-Dirac function, equation (2.14), described in section (2.3), the heat capacity of an electron gas can be expressed by equation [10]

$$C_{el} = \frac{1}{2}\pi^2 N k_B \frac{T}{T_F} \tag{2.55}$$

where with N number of electron states derived from the expression of the density of states, k_B the Boltzmann constant and T and T_F the temperature and the Fermi temperature, respectively. For more details on the derivation see reference [58]. The thermal conductivity of a Fermi gas then follows from 2.55 with the insertion of the Fermi energy $E_F = \frac{1}{2}mv_F^2$ where m is the mass and v_F^2 the electron velocity at the Fermi surface

$$\kappa_{el} = \frac{\pi^2 n k_B^2 T \tau}{3m} \tag{2.56}$$

where n is the electron concentration and τ the relaxation time of the electrons. The ratio between the electronic conductivity and the electronic contribution for the thermal conductivity can then be found by dividing equation (2.56) by the expression for the electric conductivity, equation (2.21)

$$\frac{\kappa_{el}}{\sigma} = \frac{\pi^2 n k_B^2 T \tau / 3m}{n e^2 \tau / m_e^*} = \frac{\pi^2}{3}\Big(\frac{k_B}{n}\Big)^2 T = LT \tag{2.57}$$

where, L, is the *Lorenz number*, $\approx 2.45 \times 10^{-8}$ W/deg^2, introduced in section (1.3) revealing Wiedeman Frantz law.

$$\kappa_{el} = \sigma L T \tag{2.58}$$

relating the electronic contribution to the thermal conductivity from the electric conductivity. A widely used way to determine the lattice thermal conductivity is subtracting the electronic contribution found through Wiedemann Franz law from the total thermal conductivity.

2.6.7 Effect of porosity and correction models

As discussed in the previous sections the scattering of phonons at lattice perfections contributions to the overall lowering of thermal conductivity. Porosity of samples will thus be influential to the thermal conductivity. When comparing samples it is therefore beneficial to eliminate the contribution form porosity to reveal the true difference in thermal conductivity. Several models have been presented in literature to correct for affect of porosity, [74–76] but only a few will be applied and discussed in this thesis. The commonly accepted expression for *porosity factor*, Φ, chosen in this work is

$$\Phi = \frac{\rho_0 - \rho}{\rho_0}\, 100\% \tag{2.59}$$

where ρ_0 is the density of a fully dense material and ρ the density of the porous sample. Although it is known that charge carrier transport is also affected by porosity only the effect on thermal conductivity is discussed in this section due to the focus of the project being on that.

Model presented by Klemens *et al.* : An early theoretical treatment by Maxwell where spherical pores were assumed, and the convection in them ignored [77]

$$\kappa_{porous} = \kappa_{dense}(1 - \frac{3}{2}\Phi) \tag{2.60}$$

Model presented by Schlichting *et al.* : Investigation done by Schlichting, based on the theory of Klemens, present another model for porosity correction also assuming spherical pores and uniform distribution [75, 78]

$$\kappa_{porous} = \kappa_{dense}(1 - \frac{4}{3}\Phi) \tag{2.61}$$

The Maxwell-Garnett model : A modified Maxwell-Garnett model for porosity correction based on reference [77,79]. The model is a rough assumption which assumes isotropy and neglect pore geometry and convection

$$\kappa_{eff} = \kappa_d \, \frac{2 - 2\Phi}{2 + \Phi} \tag{2.62}$$

where κ_{eff} is the effective and κ_d the thermal conductivity of the dense material.

Cracking would also heavily affect the thermal conductivity of samples, however, to obtain a good understanding of this, an extensive study has to be made. Unfortunately this is beyond the scope of this project and will not be presented. The interested reader is referred to references [80–82].

2.7 Electron microscopy

This section will give a brief introduction to the field of electron microscopy and present some of the main types of instruments and techniques. The section is based on the theory presented by Fultz & Howe [53], Williams & Carter [83] and Brandon & Kaplan [84].
An electron microscope uses beams of high energy electrons to illuminate the specimen. High energy electrons are emitted from an electron gun and accelerated to voltages of a few to several hundred kV. Two main types of electron microscopes are illustrated in figure (2.9), a a) Scanning electron microscope (SEM) (left) and Transmission electron microscope (TEM) (right). In both microscopes, electromagnetic lenses focuses the electrons through a complex lens system onto the specimen. In a SEM, backscattered electrons are detected and the sample can be several cm thick, whereas in a TEM the electrons transmit, and are detected below, the specimen. TEM investigations require thin, electron transparent specimen, preferably less than 100 nm. When the high energy electrons interact with the specimen several types of signals are generated, illustrated in figure (2.10). The signals can be detected in various ways, yielding information about specimen composition, morphology, electronic properties, and structure.

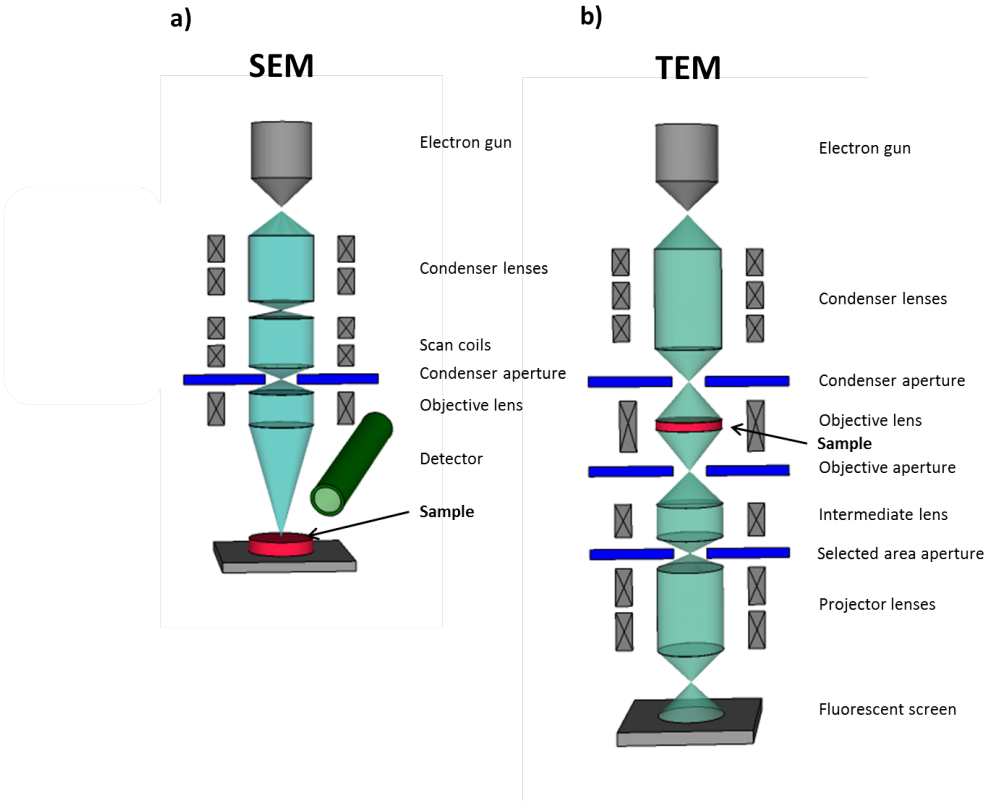

Figure 2.9: Illustrations of a a) SEM and b) TEM column, where the main components are shown

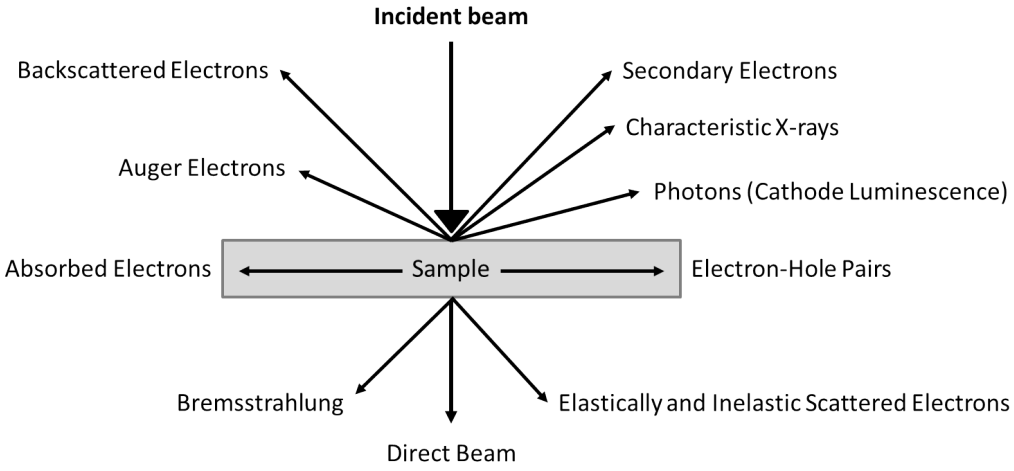

Figure 2.10: Illustration of some possible signals generated when a high energy electron beam interacts with a specimen

2.7.1 Scanning Electron Microscopy (SEM)

In a Scanning Electron Microscope a converged beam of electrons is scanned over a sample. The volume probed by the incoming beam, the *interaction volume*, is increasing upon increasing acceleration voltage and decreasing with increasing atomic number, Z, and density of the sample. The resolution obtained in a SEM is limited by the focused beam probe size on the sample surface, which is dependent upon lens aberration and the beam current. *Backscattered electrons* are electrons scattered at high angles thus have a high probability of escaping the sample surface. The number of backscattered electrons increase with average atomic number of the sample, $\bar{Z}$, hence the composed image is sensitive to different phases and thickness. Also crystal orientations will affect the number of backscattered electrons allowing orientation sensitive images to be obtained, named *electron backscattered diffraction (EBSD)* imaging. *Secondary electrons* are emitted when electrons, from atoms close to the sample surface, are excited and gain sufficient energy to escape the sample. Secondary electrons are divided into two categories, the ones that are generated when electron beam enters the sample, and those generated by high energy backscattered electrons. The mean free path limits the excitations to near surface electrons, yielding an image sensitive to morphology and topography.

2.7.2 Transmission Electron Microscopy (TEM)

In a Transmission Electron Microscope (TEM) the electrons transmit the specimen and is collected below the specimen stage. By inserting apertures, biprisms, or different detectors in the beam path, several types of imaging and spectroscopy techniques can be performed.

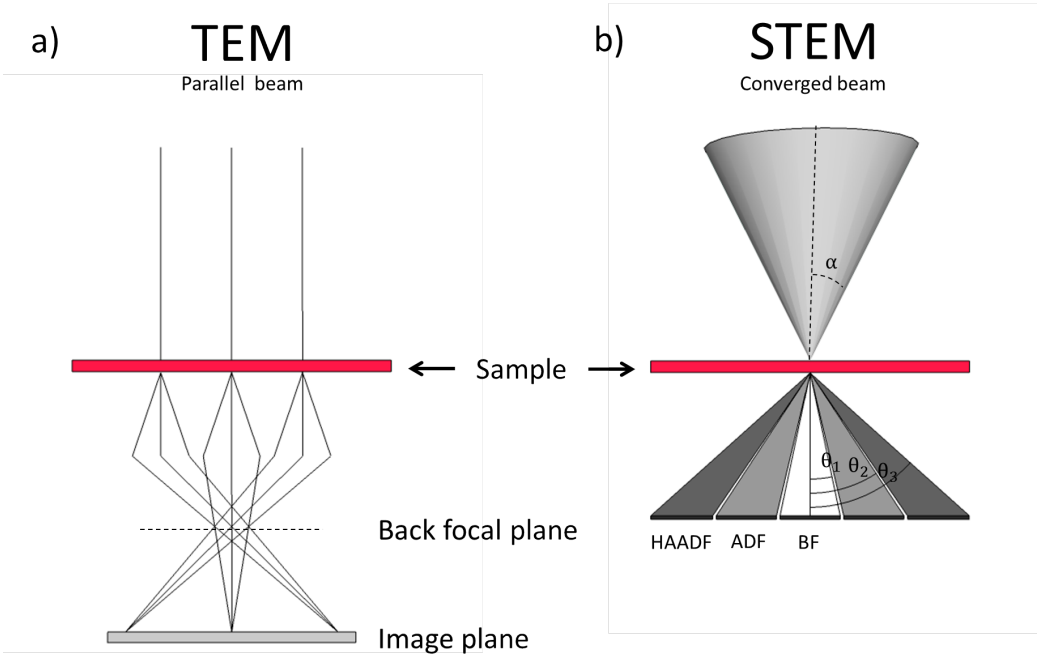

Figure 2.11: Ray diagram for a) TEM operation mode with parallel incoming beam and b) STEM operation mode with a converged beam, where α ia the convergence semi-angle.

This makes TEM a versatile and powerful tool for microstructural characterisation. The microscope can be operated in two main modes, with a parallel incoming beam, *Transmission Electron Microscopy* (TEM), or a converged beam scanning over the specimen or staying in one spot, *Scanning Transmission Electron Microscopy* (STEM). These two modes of operation are illustrated in figure (2.11). In both modes one can either image or the back focal plane or the image plane as indicated in figure (2.11).

Forward scattered and transmitted electrons are either viewed on a florescence screen or digitally imaged by use of a CCD camera. If the TEM is operated in STEM mode, the STEM detector is inserted in the beam pathand the imaging is acquired digitally. Direct transmitted electrons and electrons scattered to low angles are detected by an Annular Bright Field (ABF) detector while electrons scattered away from the optical axis are detected by Annular Dark Field (ADF) or High-Angle Annular Dark Field (HAADF) detectors. On the instrument used in the current project, the florescence screen can be lifted allowing the electrons to travel into the Gatan imaging filter (GIF). Located before the GIF is a magnetic prism dispersing the electrons according to their energy. This allows detection of electrons as a function of electron loss to be obtained, called electron-energy loss spectroscopy (EELS). By inserting a slit in the focal plane of the magnetic prism, selecting energy intervals corresponding to electron energy losses, an *energy filtered image* is obtained. By selecting intervals associated with specific energy loss processes

chemical mapping and identification of loss process can be obtained. The EELS spectra can also reveal qualitative information about local bonding environment, dielectric properties, band gaps and more.

Selected area diffraction (SAD)

A selected area diffraction pattern (SADP) is obtained when the microscope is operated in TEM mode and a small area on the specimen is selected by a selected area aperture. The selected area aperture is inserted in the image plane, indicated in figure (2.11), and typically have diameter of 1-10 μm. By changing the strength of the intermediate lenses, the back focal plane is projected, and the spot pattern of the back focal plane is viewed. As discussed in section 2.2.1 the spot pattern represent diffraction from specific atomic planes where the distance between spots relates to interplanar distances as

$$d = \frac{\lambda L}{R} \tag{2.63}$$

where L is the camera length used when obtaining the pattern, λ the wavelength of the incoming electrons and R the measured distances in the spot pattern, which is inversely related to the planar distances in the crystal being analysed. A spot pattern can be indexed by comparing the measured distances ($\mathbf{g}$ vectors) with d-values of the correct material and the corresponding zone axis can be found from the cross product of two vectors in the pattern. A SADP showing extra, missing or split reflexes might indicate structural deviations such as vacancies interstitials or superstructures.

Imaging and contrast

One of the strengths of a TEM is the high spatial resolution, down to sub-Ångstrøm for state of the art instrument operated in STEM mode. The instrument used in the present project has a spatial resolution of 1.9 Å when operated in TEM mode. Electrons going through the sample are both elasticity and inelastic scattered. Both types can be used for imaging, however, many of the strengths of imaging in a TEM is due to the elastically scattered electrons.

Mass-thickness contrast

If the sample is non-crystalline, the intensity from the interacted beam is dependent upon the electron beam energy, the thickness of the sample and the scattering strength of the elements. The contrast obtained by these interactions are called *mass-thickness contrast* consisting of incoherent elastic scattered electrons. By ensuring a uniformly thin sample only the variation in scattering strength determine the contrast. This is referred to as *mass contrast*, or Z-contrast,

due to dependence of the atomic number of the scattering atoms. The obtained contrast can be expressed as relative intensity

$$C = \frac{I_1 - I_2}{I_1} = \frac{\Delta I}{I_1} = 1 - \exp(-Q\Delta t) \tag{2.64}$$

and is dependent upon the thickness variations, Δt, and the elastic scattering cross section of the atoms. For crystalline samples there will also be intensity contributions from diffracted electrons. By inserting an aperture around the central spot at the back focal plane of the objective lens the selection of only the forward scattered and transmitted electrons can be made obtaining a *bright-field image*, obtaining mass-thickness contrast. In the same manner reflections corresponding to the electrons scattered by a specific atomic planes can be selected obtaining a *dark-field image* with mass-thickness contrast.

Diffraction contrast

To obtain strong diffraction contrast the sample is tilted to *two beam condition*, where the central spot and one diffracted spot is strongly excited. The image contrast is then determined primarily by the amplitude difference of the electrons which are scattered from atomic planes or defects satisfying the Bragg condition, appearing bright, and those who are not, appear darker. The phase difference ϕ of the scatterer at position $\mathbf{r}$ with the respect to the origin in the column of the material responsible for the contrast is then given by

$$\phi = 2\pi(\mathbf{g} \cdot \mathbf{r}) \tag{2.65}$$

with the expression for the amplitude scattered from a unit cell

$$Ae^{i\phi} = A\exp[2\pi i(\mathbf{g} \cdot \mathbf{r})] \tag{2.66}$$

allowing calculation of direction of objects in the crystal.

Phase contrast and high resolution imaging

By selecting only some of the transmitted electrons the overall intensity and possible resolution in the image is compromised. To obtain high resolution images more intensity is needed and all forward scattered electrons are let into the imaging system, $\alpha\langle 2\theta_B\rangle$. The forward scattered and diffracted waves will have different phase shift travelling through the sample. The interference between them in the image plane gives *phase contrast* reflecting the periodicity of the crystal. Contributing to the phase shift is the thickness, scattering factor and orientation of the sample. In addition, the resolution of the image is determined by the astigmatism of the lens system and

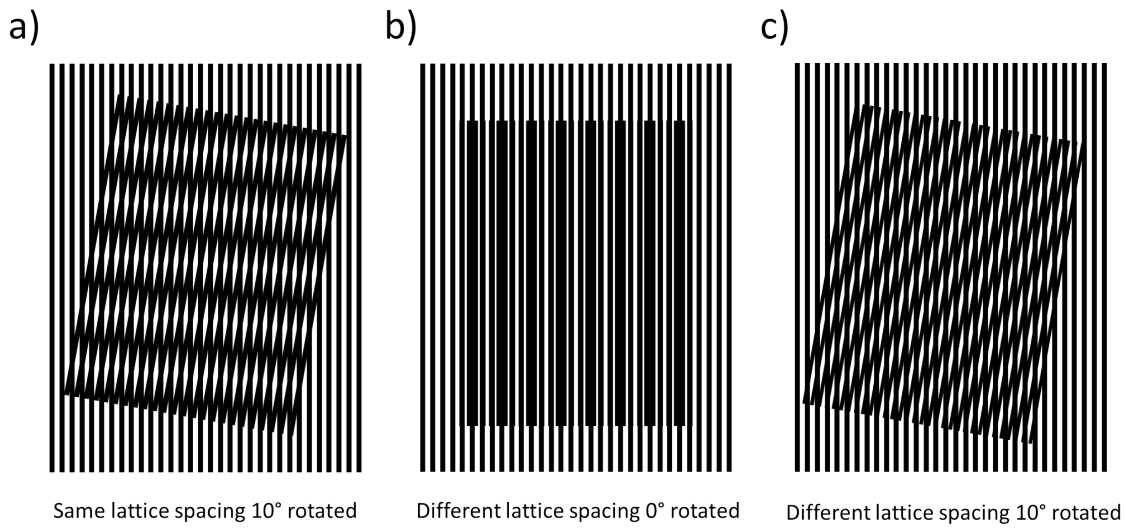

Figure 2.12: Illustration of Moire fringes wit a) equal plane spacing and rotated, b) unequal plane spacing and not rotated and c) unequal plane spacing and rotated.

coherence and energy spread of the incident electrons. In the same way the direct and diffracted waves interact to create phase contrast, waves travelled through two overlapping grains would interfere and create an additional phase contrast. This result in a line like pattern named *Moirè fringes*, illustrated in figure (2.12), with a) rotational, b) translational or rotational or a c) mix of the two. The spacing relating the two grains A and B, with angle of rotation, β, might be expressed as follows Fringes could also arise due to *thickness effects* and *bending contours*. Under dynamic conditions multiple scattering of electrons will lead to phase shifts and intensity variation appearing as lighter and darker lines on the sample. For thickness fringes the extinction factor remains constant as the thickness varies resulting in alternating bright and darker lines, while bending contours appear as pairs of bent lines with constant thickness and locally varying extinction factor.

2.7.3 Spectroscopy in electron microscopes

When the electrons from the probe enter the specimen, illustrated in figure (2.10), atomic electrons might be excited and de-excited yielding characteristic X-rays corresponding to the discrete energy levels in the atom. This yields a strong technique for obtaining chemical information about the sample. An X-ray spectrum is acquired from a small area limited by the probe size.

Energy Dispersive Spectrometer (EDS)

In Energy Dispersive spectrometry (EDS) the photons are collected as a function of their energy. The signal is detected by a solid-state detector consisting of a cooled semiconductor crystal which gives a current pulse in response to the charge generated by the energy of the incoming photon. The decay time of the pulse before being accessible for a new excitation is called the *dead time* of the detector. Together with the dead time the energy resolution is the limiting features of the EDS technique. Poor energy resolution might yield overlapping and hence indistinguishable characteristic peaks from the different chemical constituents. When acquiring EDS spectra control of experiment conditions to decrease artefacts are important. Such artefacts can be 1) sum peaks, when the detector is unable to distinguish between two X-ray and sum them together to one, 2) escape peaks, internal excitation in the detector decreasing the recorded energy, and 3) internal fluorescence, X-rays generated in the detector, yielding signal of elements only located in the detector.

Wave Dispersive Spectrometer (WDS)

Contrary to EDS, Wave dispersive spectroscopy (WDS) detect the photons as a function of wave length, providing a much higher spectral resolution. WDS is often performed using an Electron Probe Micro-Analyser, operated similar to a SEM. A series of bent single crystals with different lattice spacings are scanned by rotating the sample and detector, yielding signals at specific Bragg conditions, corresponding to the characteristic wavelengths of the emitted photons. All characteristic wavelengths must be scanned sequentially, one element at the time, resulting in long data collection times. With more than one spectrometer, several elements can be detected in the same scan rotation lowering the acquisition time of the experiment.

Other excitations and possible characterisation techniques are based on the excitations cathodoluminescence, plasmons and Auger electrons. However his will not be discussed futher, and the interested reader is referred to the references [53, 83, 84].

Chapter 3

Experimental methods

In this chapter, the methods used to synthesise and characterize samples are presented. The first section is dedicated to the synthesis methods of powders and samples, while the second section present the characterisation techniques used to determined phase composition and structure. The last section introduce the apparatus and methods used to determined the thermoelectric properties of the samples.

3.1 Sample synthesis

The samples investigated in this master project were synthesised by solid state reaction (SSR). Five compositions, yielding 15 individual samples, were synthesized to investigate the dependency of Mn content and sintering conditions upon structure and thermoelectric properties. Two additional samples, with correlating compositions, were received through collaborations with NTNU in the THELMA project, to investigate the influence on thermoelectric properties with a different synthesis technique. The batch prepared by Sathya Prakash Singh, PhD candidate at NTNU, will be referred to as CMO_NTNU and the samples synthesized at UiO as CMO_UiO.

3.1.1 Sample synthesis CMO_UiO

CMO_UiO samples were prepared from the $CaCo_3$ and MnO_2 precursor materials listed in table (3.1). The synthesis were performed following the following five steps described below

1. **Weighing and milling of precursor powders** $CaCO_3$ and MnO_2 were weighed out corresponding to the desired cation ratios with an analytical weight, Sartorius ED2245, and ball milled in agate jar with isopropanol and ∼12 agate balls of 10 mm diameter, using a Retsch rotary ball mill. The powders were ballmilled for 2 hours at 300 rpm with

15 minute intervals and 1 minute break time. After ball milling, the powder was dried at ∼120 °C in a Heraeus heating cabinet until isopropanol was evaporated.

2. **First calcination** The powders were calcined in alumina crucible in a muffle furnace either a Nabertherm LHT 04/17 or Entech SF-4 at 1050 °C for 18 hours with ramp rates 400 °/h up and 450 °/h down.

3. **Second calcination** The powders were ball milled, dried and calcined a second time in the same manner as point 1.-3. This because the full reaction and desired phase composition was not obtained after the first calcination.

4. **Pellet pressing** A third ball milling process, similar to point 1., was performed to prepare the batch for pellet pressing. Approximately 0.8 g of the obtained powder was weighed out and pressed into a pellet using 13 mm die and a Specac pellet press, pressed with ∼ 2 t.

5. **Sintering** The pellet was sintered on a pile of sacrificial powder, on an alumina plate with alumina cover, at 1200 °C for 20 hours with ramp rate 300 °/h up and 220 °/h down in a Nabertherm HT 04/17 or Entech SF-4 furnace.

Chemical	Formula	Supplier	Purity
Calcium Carbonate Precipitated	$CaCO_3$	Sigma-Aldrich	$\geq 99\,\%$
Manganese(IV)oxide	MnO_2	Sigma-Aldrich	$\geq 99\,\%$
Isopropanol	C_3H_8O	VWR International AS	$> 99\,\%$

Table 3.1: Precursor materials used for synthesis of CMO_UiO samples

3.1.2 Sample synthesis CMO_NTNU

Similar to the CMO_UiO samples, the CMO_NTNU samples were synthesised by SSR, with the main difference being the preparation of single phase precursor powder, $CaMn_{1+y}O_{2-\delta}$, under reducing conditions, before sintered and annealing while reoxidating. Only the general specifications will be presented for this synthesis.

Preparation of single phase precursor powder

Single phase precursor powder $CaMn_{1+y}O_{2-\delta}$ was synthesised by weighing out starting material $CaCO_3$ and MnO_2 corresponding to the desired cation ratio, and ball milled for 2 h. The powder

was heat treated under reducing atmosphere, 5 % H_2 + Ar, at 1250 °C with dwell time of 6 h and heating and cooling rate of 200 °/h.

Sintering and annealing

The precursor powder was ball milled for 30 min at 175 RPM in a planetary ball mill and pressed into a green body. The green body was sintered with heating rate 200 °/h in 5 % H_2 + Ar up til 1350 °C. The atmosphere was switched to 5 % N_2 (g) while heating, at 850 °C. After 6 h dwell time the atmosphere was switched to synthetic air, following 40 h dwell time, before being cooled with cooling rate 100 °/h to room temperature.

3.2 Characterization of phase composition and structure

A large variety of characterization techniques have been applied in order to investigate both the structure and properties of the samples. The subchapters of this section aim to give a short overview of the methods and equipment used.

3.2.1 Density measurements

The density of sintered samples were evaluated by geometric and Archimedes density measurements, in addition to image analysis from micrographs.

The geometric density, ρ_G, of the sintered pellets was found by measuring the diameter and height using a digital caliper and weighing on analytical weight Sartorius ED2245. The geometric density was calculated through equation (3.1),

$$\rho_G = \frac{m}{\pi r^2 h} \tag{3.1}$$

here m is the mass in grams, r is the radius and h is the height of the pellet.

Archimedes density measurements was performed using a modified setup of the Density Determination Kit from Sartorius YDK03 with water as the immersion liquid of choice. The weight of the sample was measured dry, m_{dry}, and immersed, m_{im} and the density is obtained through the following relation

$$\rho_A = \frac{m_{dry}\,\rho_{liq}}{m_{dry} - m_{im}} \tag{3.2}$$

Where ρ_{liq} is the density of the liquid at room temperature.

The porosity of the samples, Φ was determined by comparing the theoretical densities ρ_0 with the measured ρ

$$\Phi = \frac{\rho_0 - \rho}{\rho_0} \cdot 100\% \tag{3.3}$$

Image analysis of micrographs were performed using the program imagej [85]. The density was determined from the calculated area fraction of area corresponding to pores by the program, by assuming spherical pores cut at random heights.

3.2.2 X−ray diffraction

Phase identification of powder samples was obtained by X-ray diffraction (XRD) on a Rigaku MiniFlex600 with a D/teX 1D silicon strip high speed detector and radiation CuKα, λ = 1.5418 Å. The analysis was performed in the range $5\,^\circ \leq 2\theta \leq 90\,^\circ$ with settings; step $0.02\,^\circ$, speed of $2\,^\circ/_{\text{min}}$ and emission of 40 kV with 15 mA. The divergence slit DSO.0025, determining the width of the irradiated area on the specimen, and incident sollar slit IHS19 mm, the length limiting slit which enhances peak resolution, was chosen. Aluminium holders with depth 0.5 mm or 1 mm were used for the experiments. The obtained patterns were analysed in DIFFRAC.EVA and the Powder Diffraction File (PDF) database was used for indexing.

3.2.3 Analytical Scanning Electron Microscopy

All sintered samples were investigated Scanning Electron Microscopy (SEM) to study the microstructure. A Hitachi TM300-TableTop SEM with tungsten cartridge filament and backscattered electron detector, was used and operated under vacuum with an acceleration voltage of 15 kV. The samples were glued to stubs with crystal bond and in some cases grinded using diamond lapping films with particle size from 30 μm to 1 μm on multiprep machine.

Energy dispersive X-ray spectroscopy (SEM)

Energy dispersive X-ray spectroscopy (EDS) was performed to characterize the chemical composition of local areas in the samples. The detector used was a Quantax70 from Bruker with a Silicon drift detector (SDD) with energy resolution of 154 eV from a CuKα source. The acquisition times were chosen so that x-ray counts of the area of interest stood to good quality (quality green on quality bar) provided by the Quantax70 program. The elements were determined by K-series.

3.2.4 Electron Probe Micro-Analyzer (EMPA)

As a complementary technique for determining the chemical composition for a selection of samples, in addition to affirm the quantification done by SEM, Electron Probe Micro-Analysis (EPMA) with wave dispersive spectrometry (WDS) was performed. The CAMECA SX100 EPMA probes small areas, down to 1 μm, with a focused electron beam and quantify phase composition by detecting the wavelength of diffracted X-rays from the crystal. The instrument is equipped with four wavelength dispersive spectrometers with moving monocrystal as monochromators, which, when satisfying Braggs law, counts the signal generated with the given wavelength. This allows multi element analysis in the 100 ppm to 100 per cent range. In the experiments performed in this project, an acceleration voltage of 15 kV and a beam current of 15 nA was used.

3.2.5 Analytical Transmission Electron Microscopy (TEM)

The structural characterization of the specimens down to sub nano level was performed using Transmission Electron Microscopy (TEM), a JEOL JEM-2100F, operated at an acceleration voltage of 200 kV. The instrument is equipped with a Schottky FEG and a pole piece giving a point resolution of 1.9 Å. A JEOL double-tilt sample holder, EM-31640, was used for all experiments. High and low resolution TEM images were acquired by an Orius CCD camera and high and low resolution Scanning Transmission Electron Microscopy (STEM) images by JEOL scanning image observation device EM-24541SI0D with EM-271021AU Image Acqusition Unit. Energy filtered images and electron energy loss spectroscopy were aquired by Gatan Imaging filter (GIF) Quantum from Gatan and Energy dispersive x-ray (EDS) analysis by Oxford instrumentation X-Max^N 80 T with a Silicon Drift Detector (SDD). All analysis were done close to specimen edge to ensure thin area of investigation to limit artefacts such as multiple scattering, overlapping grains and absorption. Data was processed using Digital Micrograph provided by Gatan in addition to supportive indexing tools such as Jems and CrysTbox [86].

Energy-Dispersive Spectroscopy (EDS)

TEM-EDS was performed as spot analysis with 2 nm spot size and STEM-EDS with a scanning probe of 1 nm. EDS experiments were done with specimen tilted towards the detector and analysed by element K-edges and the following k-factors; $k_{Ca} = 0.993$, $k_{Mn} = 1.183$ and $k_O = 1.982$. The AZtecEnergy software provided by Oxford Instruments was used for analysing the data.

TEM specimen preparation

TEM specimens were attempted prepared in three ways. The standard specimen preparation approach, polishing and Ar-ion thinning (1), was unsuccessful due to the samples being resistant to ion etching. As an alternative preparation method specimens were crushed and thin edges examined. The crushed specimen on holey C-film preparation (2), is fast and exclude damage from Ar-ion milling. However, the control over what fraction of the sample is being investigated is lost. As a last attempt, Focused ion beam (FIB) specimens (3), were prepared by collaboration at Wroclaw Research Centre EIT+, by Sandeep Gorantla and Anna Siemiatkowska. This was found to be successful, but also time consuming due to the etching resistance of the specimen. Thus, due to time and cost considerations, only one specimen was prepared. A more detailed description on each preparation method is given below.

1) Polished specimens were prepared by initial rough grinding on SiC paper, before thinning and polishing with a MultiPrep machine with diamond lapping films with particle size from 30 μm to 1 μm. Final thinning was done by ion milling in a Fischion (model 1010) or Gatan PIPS (model 691 or PIPS II). The conditions normally used were upper and lower source voltage 5 kV and upper and lower source current 5 mA with stage rocking $\pm$ 45 degree, repositioned every 5 minutes, with milling angle of 7 degree and milling time of 30 minutes. The milling angle and time in addition to the upper and lower source voltage were reduced stepwise as the specimens were thinned. The thinned specimens were then glued to a Cu ring using Gatan cross-sectional glue kit (MODEL 601.07). The specimens proved to be very resistant to ion milling thinning and alternative methods for specimens preparation were chosen.

2) Crushed specimens were prepared by crushing and grinding in ethanol using mortal and pistol before beeing sonicated in a Branson device for approximately 5 minutes. A drop of solution extracted from the middle layer was then transferred to holey carbon film with 300 mesh Cu(50).

3) Focused ion beam (FIB) lamellas were prepared by milling technique using a FEI Helios NanoLab H50HP SEM/FIB instrument with GA^+ ion gun. A protective Pt layered was deposited to the area of interest in two steps, $\sim$ 300 nm thick layer by e^- beam followed by $\sim$ 3 µm thick layer by ion beam. A sample slice of $\sim$ 1.5 µm was milled by two trenches adjacent to the coated area and lifted out from the bulk sample using an Easy Lift nanomanipulator. The specimen was then welded to one of the fingers of a TEM bopper lift-out grid by Pt deposition. The attached FIB lamella was then thinned to $\sim$ 100 nm using progressively decreasing currents, with ion beam energy of 30 keV followed by final thinning with low ion beam energy of 1 keV

If the specimen were to be investigated by Scanning Transmission electron Microscopy (STEM) they were plasma cleaned using Fischione model 1010.

3.3 Thermoelectric properties measurements

Thermoelectric properties of the samples were determined by measuring the electrical resistivity, Seebeck coefficient and thermal conductivity. The experimental methods, aperture setup and data interpretation are presented in the following sections.

3.3.1 Electrical conductivity and Seebeck coefficient measurements

The electrical conductivity and Seebeck coefficient were both measured in a custom built assembly based on the measurement cell ProboStat from NorECs AS, shown in figure (3.1) (left) [87]. The cell was mounted in a tubular furnace which provided the base temperature of the measurements and flushed with synthetic air controlled by an in-house built gas mixer [88]. A Keysight 34970A multichannel multimeter and Keysight E3642A power source are used to measure the voltage and temperature and provide the current for the resistivity measurements and resistivity heating of Pt10Rh coils of an internal heater. The measurements are controlled and recorded through a in-house made LabVIEW software. [87].

(a) (b)

Figure 3.1: a) ProboStat from NorECs b) Sample mounting inside the ProboStat

The sample is placed on an alumina disk on an alumina support tube and kept in position with a spring load system, illustrated in figure (3.1) (right). Four Pt electrodes, placed on the circumference of the sample, were serving as voltage and current probes for van der Pauw resistivity measurements, and kept in position by a spring load system to ensure good one point contact. Two S-type thermocouples (TCs) (Pt-Rh10, Pt) were placed on the top and bottom of the sample with spring loads to ensure good thermal and electric contact. The Pt-leads of the TCs were acting as temperature and voltage probes to measure the induced thermoelectric voltage across the sample. To induce a temperature gradient over the sample a micro resistance heater, coils of Pt10Rh with room temperature resistance of $5\,\Omega$, was placed inside the support tube, underneath the sample. A third TC was placed outside the support tube, at same hight as the sample, to control the base temperature of the furnace. Further details on the measurement setup is found in reference [87].

Electrical conductivity

The electrical resistivity of the samples were measured by van der Pauw four point method [89]. This method gives an average resistivity of the sample and possible directional dependencies are disregarded. The four point method also allows contact quality to be neglected and the contact resistivity is eliminated. Three assumptions were made to apply this method i) The measured object is dense, with no holes or cracks ii) the object has a larger area than its height and iii) the electrodes are placed on the circumference of the object and have small, single point contact. A current is applied over two of the four electrodes, e.g. I_{12}, and the potential difference is measured between the two other, in this case U_{34}, giving the four point resistance $R_{12,34} = \frac{U_{34}}{I_{12}}$. The measurement is repeated several times with increasing values of I, thus $R_{12,34}$ is found through a linear fit of the measured points. By switching the contacts acting as the current probes, applying I_{23} and recording U_{41}, $R_{23,41} = \frac{U_{41}}{I_{23}}$ is obtained. This allows the electrical resistivity to be found through the van der Pauw equation

$$\exp(-\pi\, d\, R_{12,34}\, \frac{1}{\rho}) + \exp(-\pi\, d\, R_{23,41}\, \frac{1}{\rho}) = 1 \tag{3.4}$$

when the thickness, d, of the sample is known. A series measurement is then done between the four contacts. By changing the polarity of the current applied the influence of additional voltage caused by the Peltier effect is eliminated.

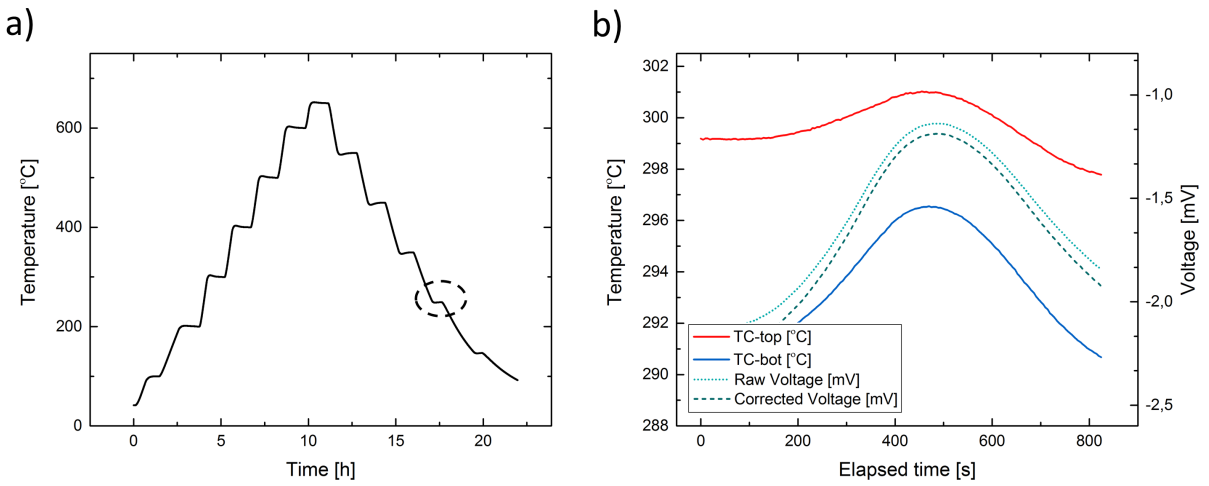

Figure 3.2: a) Show a temperature program and b) recorded Seebeck data at 250 °C (encircled area in a)) from a typical measurement cycle.

Seebeck coefficient

The Seebeck coefficient α is determined by measuring the open circuit voltage ΔU induced by a temperature difference ΔT over the sample

$$\alpha = \frac{\Delta U}{\Delta T} \tag{3.5}$$

The temperature difference is induced by resistant heating of the internal heater placed underneath the sample. The current applied to the heater, chosen to be maximum current 450 mA, increased and decreased over 13 steps with 0.8 min per step, gives rise to variation in ΔT and hence an induced voltage over time, illustrated in figure (3.2 b)).

The measured raw voltage was corrected for the contribution from the Pt-leads by subtracting the Seebeck coefficient of Pt, $U_{Corr} = U_{Raw} - \Delta T \cdot \alpha_{Pt}(T_{average})$, figure (3.3). When plotting ΔU_{corr} against ΔT, figure (3.3), the slope of the line gives the Seebeck coefficient of the material. The difference between the slope of the raw and corrected voltage corresponds to the Seebeck coefficient of the Pt-lead at the measured temperature. A typical temperature program for these measurements are shown in figure (3.2 a)) where measurements were done with 50 °C step and ramp rates of 2 °/min at low and 4 °/min at high temperatures.

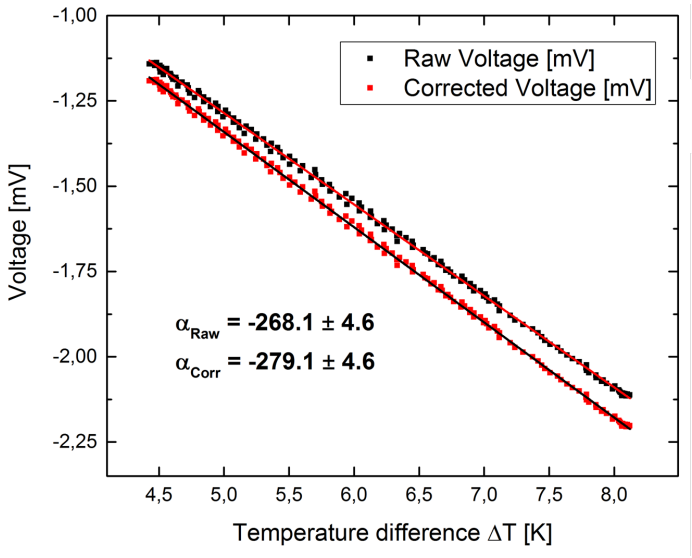

Figure 3.3: ΔU vs. ΔT plotted and fitted, with slope of the line is the Seebeck coefficient of the material.

3.3.2 Thermal conductivity measurements

The thermal conductivity, κ, of the sample was found by measuring the thermal diffusivity, D, and calculated through the following equation

$$\kappa = D\rho c_p \tag{3.6}$$

where ρ is the density and c_p the heat capacity of the sample. The diffusivity was measured by Laser Flash technique (LFA) using a NETZCSCH LFA457 MicroFlash, thermally stabilized with water cooling and with a vacuum tight sample chamber, flushed with nitrogen. Samples were coated with conductive graphite spray, GRAPHIT from Kontakt Chemie, to mimic the absorption and emission properties of a black body. A heat pulse, from a short laser pulse, is applied from the bottom side of the sample and the heat rise on top is recorded with an infrared detector. An illustration of the recorded temperature raise over time is shown in figure (3.4). The maximum temperautre rise at the rear side can be expressed as $T_{max} = \frac{q}{\rho\, c_p\, d}$, where q is the radiant energy from the heat pulse. The temperature increase with time can then be expressed as [90]

$$\tau(t) = \frac{q}{\rho\, c_p\, d}\left[1 + 2\sum_{n=1}^{n}(-1)^n \exp\left(\frac{-n^2\pi^2}{d^2}Dt\right)\right]. \tag{3.7}$$

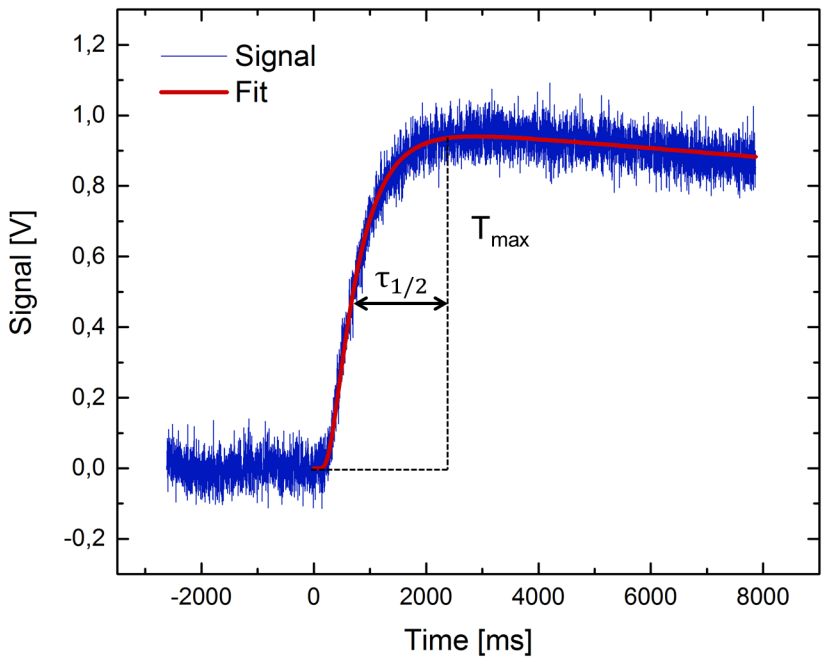

Figure 3.4: Signal vs time plot from a standard LFA measurement

where d is the sample height and t the elapsed time. Equation (3.7) is simplified by introducing the dimensionless parameters $\omega = \frac{\tau(t)}{T_{max}}$ and $\eta = \frac{\pi^2}{d^2}Dt$ which gives

$$\omega = 1 + 2\sum_{n=1}^{n}(-1)^n \exp(-n^2\eta) \tag{3.8}$$

The temperature rise over time curve, figure (3.4), is fitted to theoretical values and the quality of the measurement is evaluated by the program from predetermined requirements. If approved, the half time, $\tau_{1/2}$, is found from the half maximum temperature which gives $\omega = \frac{\tau(t)}{T_{max}} = 0.5$ hence $\eta = 1.38$ and the relation for the diffusivity is obtained as follows

$$D = 1.38\frac{d^2}{\pi^2\tau_{1/2}} \tag{3.9}$$

The heat capacity of the material is found through the reference sample Pyroceram 9606, also provided by Netzsch, by applying the Cape-Lehman Model fit to the diffusivity. The thermal conductivity is then found through equation (3.6). If the sample contains internal pores filled with air which a low thermal conductivity, $\sim$0.02 W/mK, this will significantly influence the results [10]. Correction models have been applied, presented in section 2.6.7, to reveal the pure thermal conductivity of the material.

3.4 Errors

For every experimental technique presented in this chapter there will be random and systematic errors associated with the technique. While systematic errors in measurement setups might yield high precision, low accuracy of the measurement might still be present. By random errors, the accuracy might be good while the precision thus the spread in the measurement might be large. Several measurements of same samples, and variation of experiment setup has been made to detect and minimize potential random and systematic errors. This will be further discussed in chapter 4.3 and is only briefly touched upon here.

Possible errors Contaminations might be introduced in all stages of sample preparation, either by equipment used or the apparatus itself. This was attempted prevented by wearing protective gear and thoroughly cleaning equipment before use. In all furnaces used, temperature gradients might exist, thus an uneven heat distribution. This effect was tried minimized by placing samples in the middle of furnaces.

Error estimation For several of the electrical measurement techniques, an average over measurement point is made, where error estimations can be made by calculating the mean, μ, and the spread, σ, of the measurement as follows:

$$\mu = \overline{x} = \frac{1}{n}\sum_{i=1}^{n} x_i \tag{3.10}$$

$$\sigma = \sqrt{\frac{1}{n-1}\sum_{i=1}^{n}(x_i - \overline{x})^2} \tag{3.11}$$

where n is the number of measurement points and x_i the measured value. While increasing the number of measurement points will not improve the spread if it is limited by the measurement set up, the *standard error of the mean*, eq. (3.12), will yield more information of error propagation, and will improve with increasing number of measurements. Assuming same uncertainty of σ in all measurements x_i the standard error of the mean can be expressed as

$$\Delta\overline{x} = \frac{\sigma}{\sqrt{n}} \tag{3.12}$$

Counting statistics For counting experiments such as X-rays in EDS the uncertainty is dependent upon the number of counts, N, number off events in an interval. The intensity in each peak is a result of the count over the incoming signal, applying the theory of Poisson

distribution, the uncertainty will be equal to

$$\sigma = \sqrt{N} \tag{3.13}$$

By repeating the experiment the theory of Guassian distribution predicts a likelihood of the next measurement yielding $N \pm 1\sigma$ of 68 %, $N \pm 2\sigma$ of 95 % and $N \pm 3\sigma$ of 99 %. This uncertainty should be accounted for when reporting results. The background in counting experiments will also be Poisson distributed and an evaluation of signal to noise ratio and thus the reliability of the measurement should always be performed.

Chapter 4

Results

In the following chapter the results of the structural and thermoelectric studies are presented. All samples investigated in this project are presented in table (4.1), with sample ID, composition, synthesis method and sintering temperature. The first section is dedicated to phase analysis of synthesised powders and the morphology and microstructure of sintered samples. In addition, results from investigations of the nano-structure of selected specimens are shown. In the second part, the measured thermoelectric properties of all UiO synthesised samples are reported. Lastly, a section dedicated to the investigation of the reproducibility of thermoelectric measurements and the discussion of associated uncertainties are presented.

Table 4.1: Summary of UiO and NTNU synthesised samples, $CaMn_{1+y}O_{3\pm\delta}$ with y = 0 (batch 1), 0 (batch 2), 0.020 , 0.036, 0.074 and 0.10, with sample ID, nominal composition, synthesis method and sintering temperature.

Sample ID	**Nominal Composition**	**Synthesis method**	**Sintering Temperature** [°C]
Batch 1			
CMO_UiO_0 _(a)	$CaMnO_3$	SSR in air	1200
CMO_UiO_0_(b)	$CaMnO_3$	SSR in air	1200
CMO_UiO_0_(c)	$CaMnO_3$	SSR in air	1250
CMO_UiO_0 _(d)	$CaMnO_3$	SSR in air	1300
Batch 2			
CMO_UiO_0 _(*a)	$CaMnO_3$	SSR in air	1200
CMO_UiO_0_(*b)	$CaMnO_3$	SSR in air	1200
CMO_UiO_2.02 _(a)	$CaMn_{1.020}O_{3\pm\delta}$	SSR in air	1200
CMO_UiO_2.02 _(b)	$CaMn_{1.020}O_{3\pm\delta}$	SSR in air	1200
CMO_UiO_3.66 _(a)	$CaMn_{1.037}O_{3\pm\delta}$	SSR in air	1200
CMO_UiO_3.66 _(b)	$CaMn_{1.037}O_{3\pm\delta}$	SSR in air	1200
CMO_UiO_3.66_(c)	$CaMn_{1.037}O_{3\pm\delta}$	SSR in air	1200
CMO_UiO_7.47 _(a)	$CaMn_{1.075}O_{3\pm\delta}$	SSR in air	1200
CMO_UiO_7.47 _(b)	$CaMn_{1.075}O_{3\pm\delta}$	SSR in air	1200
CMO_UiO_10 _(a)	$CaMn_{1.10}O_{3\pm\delta}$	SSR in air	1200
CMO_UiO_10 _(b)	$CaMn_{1.10}O_{3\pm\delta}$	SSR in air	1200
CMO_NTNU_3.66Mn	$CaMn_{1.037}O_{3\pm\delta}$	SSR H_2+Ar/N_2	1350
CMO_NTNU_7.47Mn	$CaMn_{1.075}O_{3\pm\delta}$	SSR H_2+Ar/N_2	1350

4.1 Sample composition and structure

4.1.1 XRD analysis of powders

Figure (4.1) show XRD diffractograms of all UiO synthesised powders, (black line corresponds to CMO_UiO_0, green to 2.02, pink to 3.66, purple to 7.47 and blue to 10) after 1st calcination (1050 °C for 18 h in air). The peak position and intensity profile of the pattern were found to be consistent with the presence of three phases; $CaMnO_3$, Ca_2MnO_4 and $CaMn_2O_4$, when the peaks from the Al-sample holder is disregarded [91]. The strongest reflections from the $CaMnO_3$ phase are found to be 121 and 202 and indexed in the diffractogram and marked with bullets, while $CaMn_2O_4$ and Ca_2MnO_4 are marked with diamond and star, respectively. Splitting of reflexes at higher 2θ is due to the radiation Cu source not being monochromated, while variation in the Al peaks intensities is due to varying amount of powder in the sample holder. The surprising presence of a Ca-rich secondary phase, Ca_2MnO_4, in the nominally Mn-rich samples indicate that the reaction was not fully completed, thus a second calcination was performed.

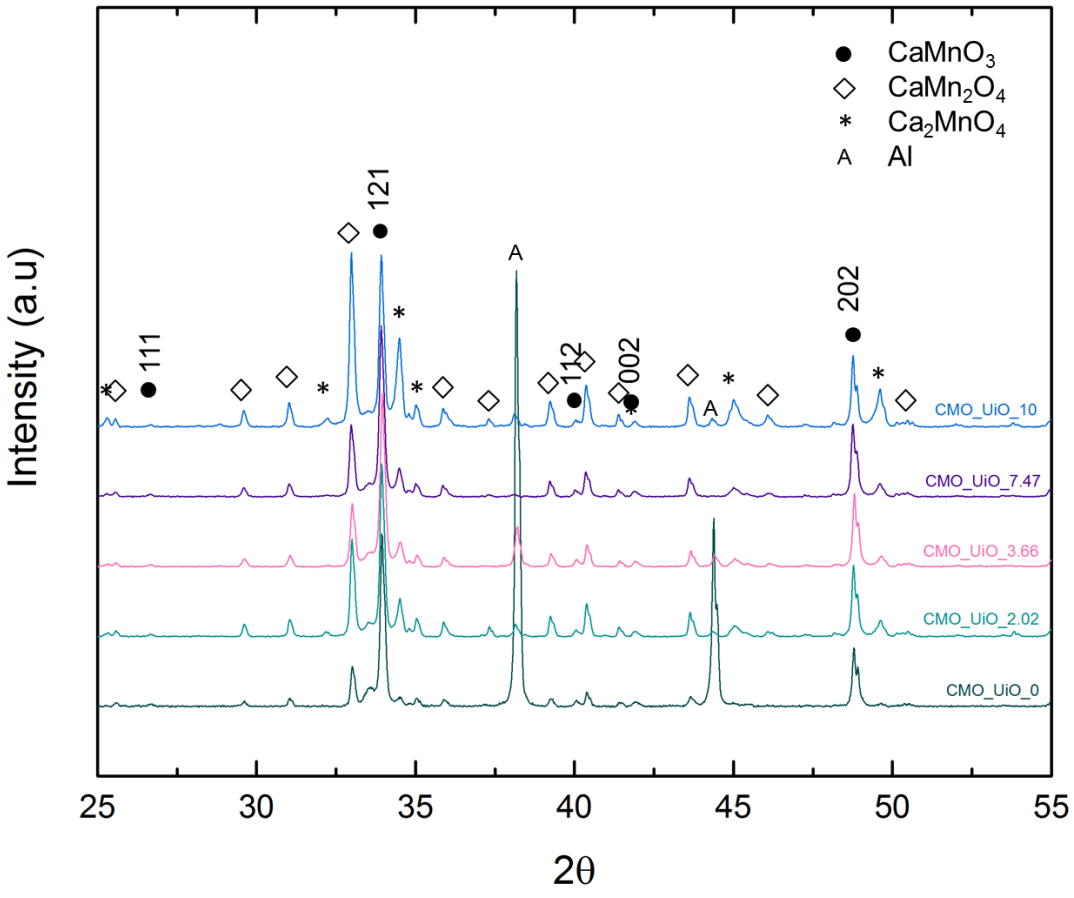

Figure 4.1: XRD for UiO synthesised samples after 1st calcination (at 1050 °C for 18 h in air). Indexed reflection correspond to • $CaMnO_3$, while ♢ $CaMn_2O_4$, * Ca_2MnO_4 and A Al (holder).

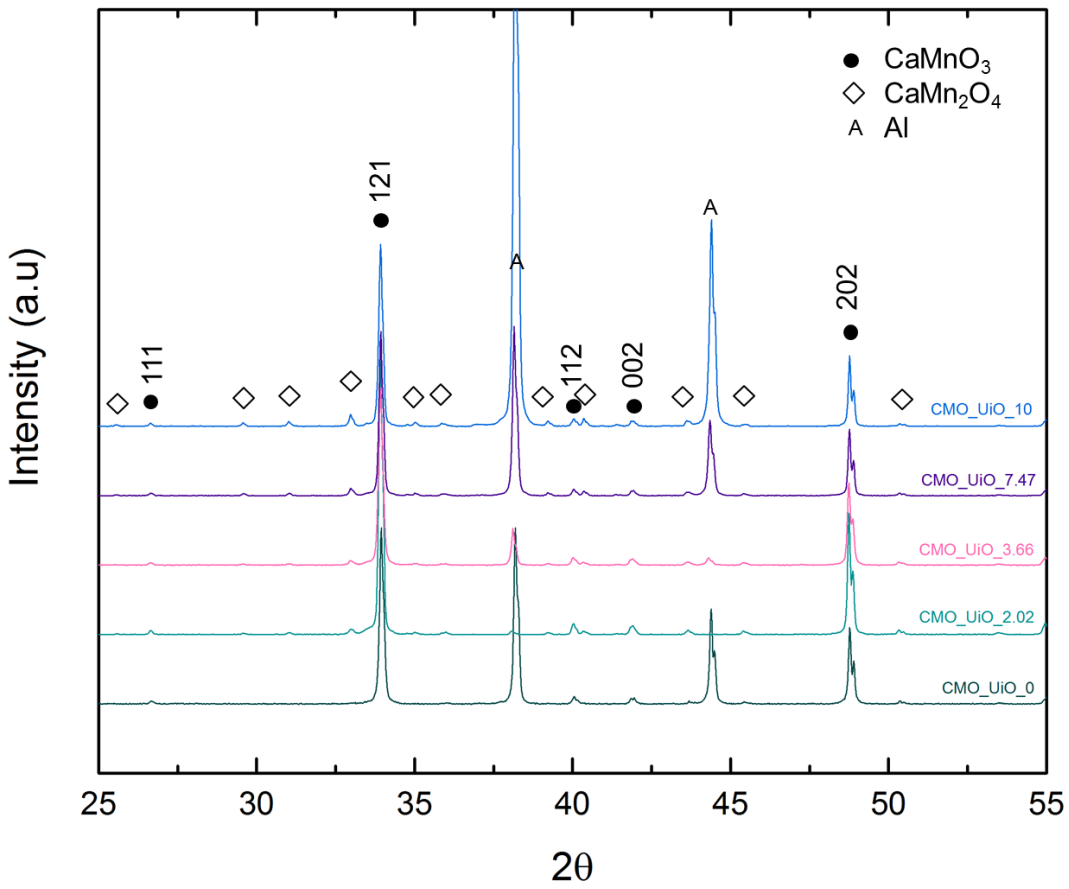

Figure 4.2: XRD for UiO synthesised samples after 2nd calcination (at 1050 °C for 18 h in air). Indexed reflection correspond to • $CaMnO_3$, while ♢ $CaMn_2O_4$ and A Al (holder).

Figure (4.2) show the corresponding diffractogram after the second calcination treatment, performed in the same manner as the first (1050 °C for 18 h in air). If the Al-peaks from the holder are disregarded, only two phases are now present; $CaMn_2O_4$ and $CaMnO_3$, identified and indexed in the same manner as figure (4.1). For the nominally stoichiometric sample, CMO_UiO_0, the only set of reflections observed corresponds to $CaMnO_3$. Comparing the peak intensities of $CaMn_2O_4$ with the $CaMnO_3$ ones, it is found that a higher Mn concentration corresponds to a relative increase of $CaMn_2O_4$ in the powders. As there were no evidence of any Ca_2MnO_4 phase still present, it was concluded that no further calcination was needed and the powders were ready to be sintered.

4.1.2 Microstructure of sintered samples

Investigation of morphology and microstructure of sintered samples was performed by SEM. Micrographs were acquired with backscattered electrons, at 1500x magnification, and are compared as a function of Mn content and sintering temperature in this section. Figure (4.3) and (4.4) show micrographs of pellet samples sintered at 1200 °C for 20 h of unpolished and polished samples, respectively. Micrographs of the unpolished samples were acquired to obtain an indication of grain size as a function of Mn content. While polished samples provide information of sample morphology an microstructure.

Figure (4.3) a) - f) show micrographs of unpolished samples $CaMn_{1+y}O_{1-\delta}$ with composition y = 0 (batch 1), 0 (batch 2), 0.020 , 0.036, 0.074 and 0.10, respectively. Sample $CaMn_{1+y}O_{1-\delta}$ with y = 0 (batch 1 and 2), image a) and b), have a homogenous grain size distribution of $\sim$ 8 µm, while sample with larger Mn excess, y = 0.074 and y = 0.10, image e) and f), appear to have two categories of grain sizes, $\sim$ 5 µm and $\sim$ 10 µm. An overall decrease in grain size with increasing Mn content is observed. Although present in the starting powqders, no secondary phase of $CaMn_2O_4$ was detected on sample surface by use of EDS. The darker areas of the images in figure (4.3) corresponds to pores located on triple points and grain boundaries, while the brighter areas can be attributed to edge effects where electrons more easily escape from the sample surface.

Figure (4.4) a) - f) show micrographs of polished samples $CaMn_{1+y}O_{1-\delta}$ with composition y = 0 (batch 1), 0 (batch 2), 0.020 , 0.036, 0.074 and 0.1, respectively. In all micrographs a low intensity matrix with brighter areas are seen. This is consistent with the expected Z-contrast from $CaMnO_3$ and $CaMn_2O_4$ respectively. The brighter $CaMn_2O_4$ grains are in the size range of $\sim$2-5 µm in all obtained micrographs, and increasing in number rather than in extent with increasing Mn composition, from a) to f). It should be noted that sample CMO_UiO_0 (batch 1 and 2), a) and f), show brighter areas corresponding to secondary phase $CaMn_2O_4$, indicating that the samples are not stoichiometric as intended. The areas appearing darker than the matrix corresponds to shallow and deep pores.

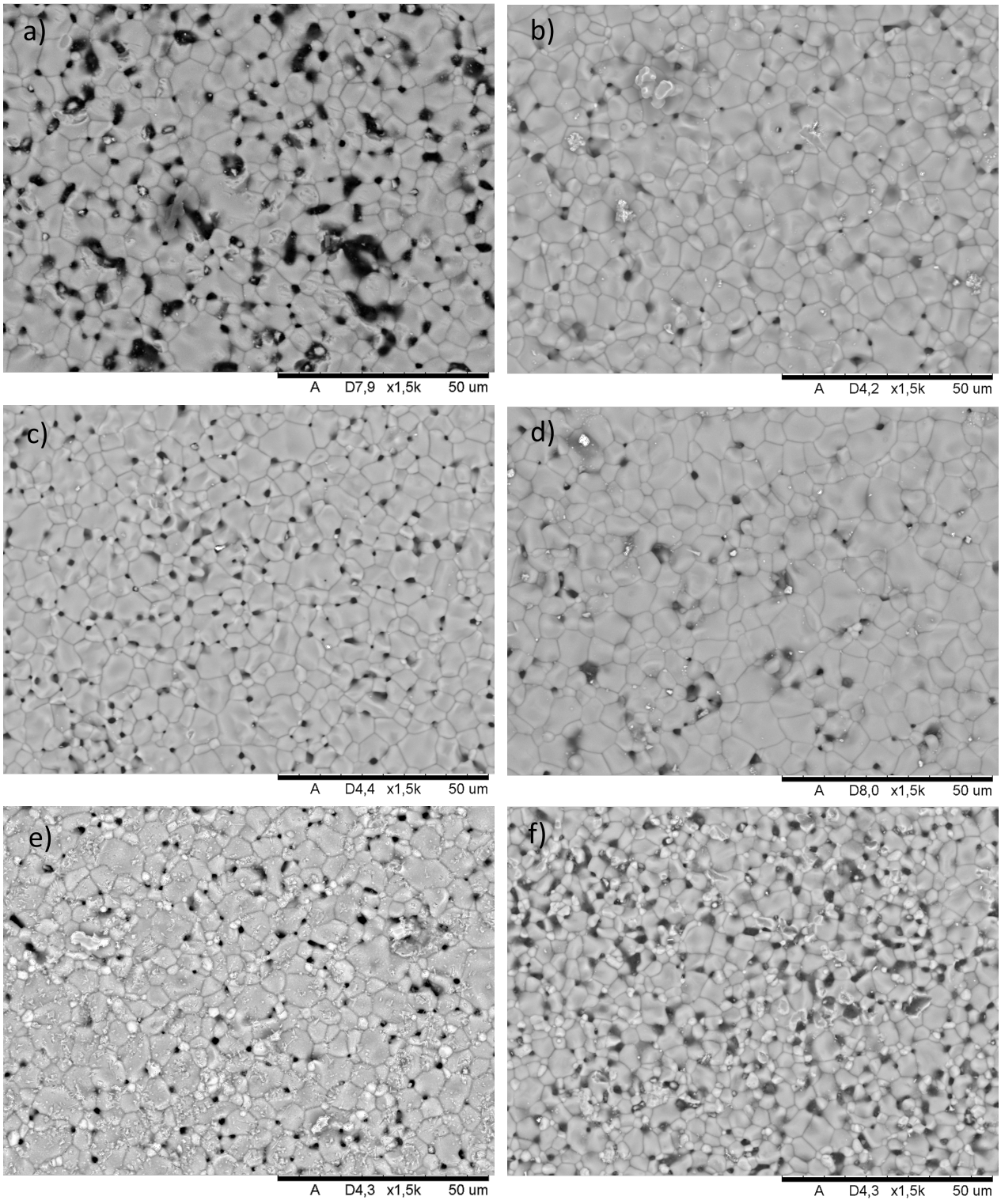

Figure 4.3: Backscatter SEM micrographs of unpolished surface indicating grain size of samples (CMO_UiO) with nominally Mn excess a) 0 at% (batch 1), b) 0 at% (batch 2), c) 2.02 at%, d) 3.66 at%, e) 7.47 at% and f) 10 at%. The dark areas corresponds to pores.

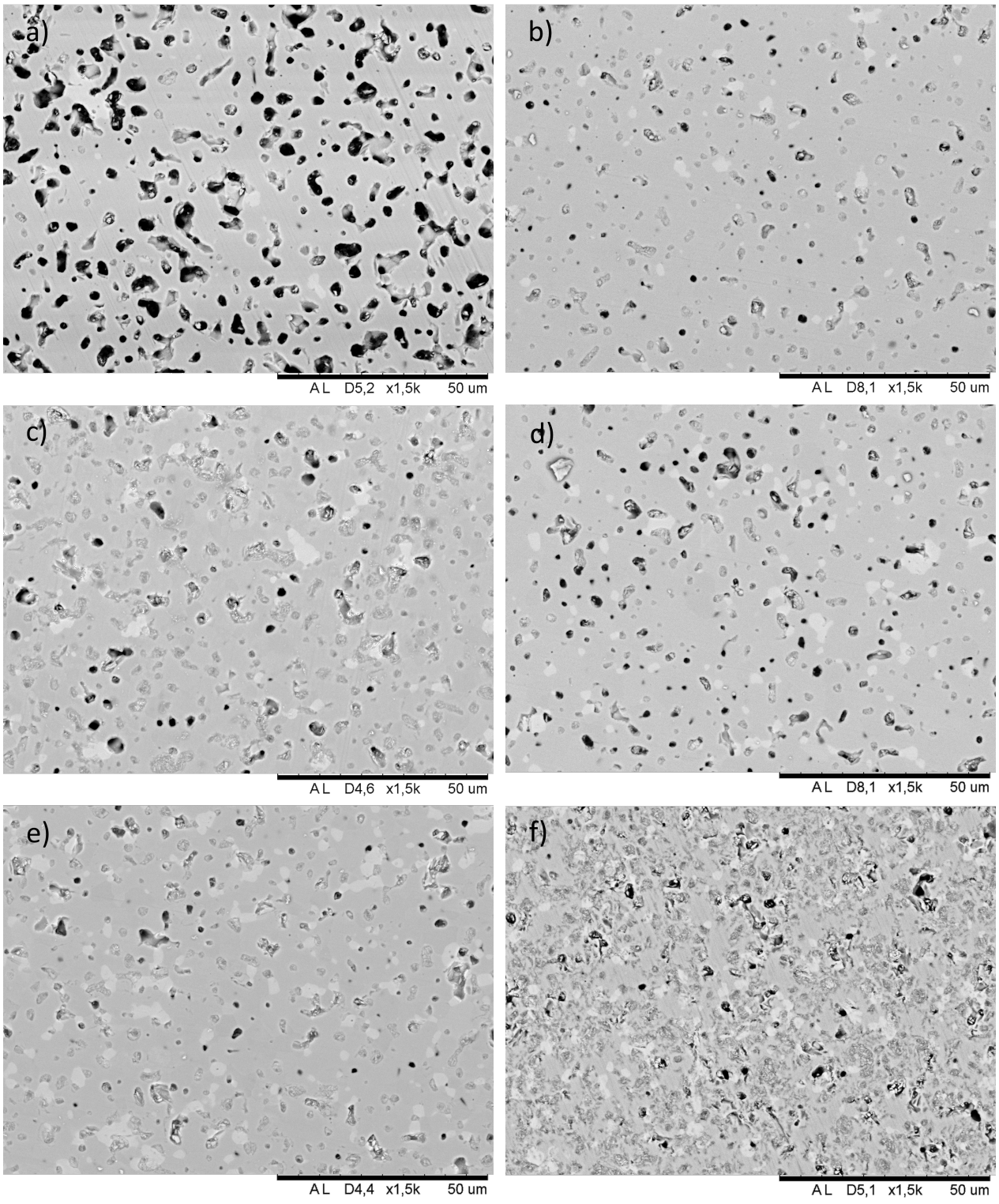

Figure 4.4: Backscatter SEM micrographs of polished samples (CMO_UiO) with nominally Mn excess a) 0 at% (batch 1), b) 0 at% (batch 2), c) 2.02 at%, d) 3.66 at%, e) 7.47 at% and f) 10 at%. Low intensity matrix and brighter grains are consistent with expected contrast from $CaMnO_3$ and $CaMn_2O_4$ respectively. The darkest areas correspond to pores.

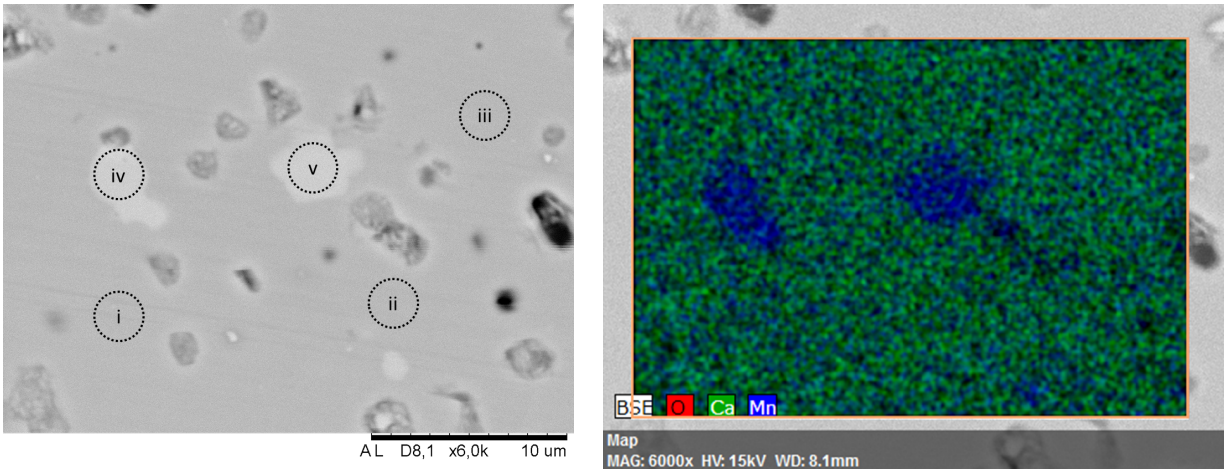

Area	(i)	(ii)	(iii)	(iv)	(v)
Mn/Ca ratio	0.95	0.98	0.98	1.48	1.53

Figure 4.5: EDS analysis of CMO_UiO_3.66 (a) showing low intensity matrix corresponding to $CaMnO_3$ and brighter area secondary phase $CaMn_2O_4$.

Chemical analysis was further performed, on all samples, by EDS, confirming main phase matrix $CaMnO_3$ and secondary phase precipitates $CaMn_2O_4$. EDS analysis of sample CMO_UiO_3.66 (a) is shown as an example in figure (4.5). The general trend inn all specimen is an observation of a Mn deficient matrix, with an average Mn/Ca ratio of 0.97. This indicate that all Mn excess precipitate as secondary phase $CaMn_2O_4$ and that no Mn rich precipitates exist within the main phase. A Mn deficient matrix might also be due to Ca rich precipitates within the main phase. However, even though the brighter areas clearly show a higher concentration of Mn relative to the matrix, figure (4.5) (right), the measured Mn/Ca ratio in all bright areas are close to 1.5 (2:3), which deviates significantly from the expected Mn/Ca ratio equal to 2 (1:2) from the $CaMn_2O_4$ phase.

Phase analysis using Electron Probe Micro-Analyzer with wave dispersive spectrometer, WDS, was performed as a supportive technique to EDS. The results are presented in figure (4.6) and compared with EDS analysis. In addition, the associated errors with the WDS and EDS analysis, calculated by the software, are included. The obtained Mn/Ca ratio by WDS show a slight enrichment of Mn in the matrix with respect to $CaMnO_3$. This could indicate that there are Mn-precipitates within the matrix. This is in contrast to EDS, which show a Mn deficient matrix. EMPA, in analogue with EDS, show an unexpected Mn/Ca ratio of 1.5 (2:3) for the brighter areas.

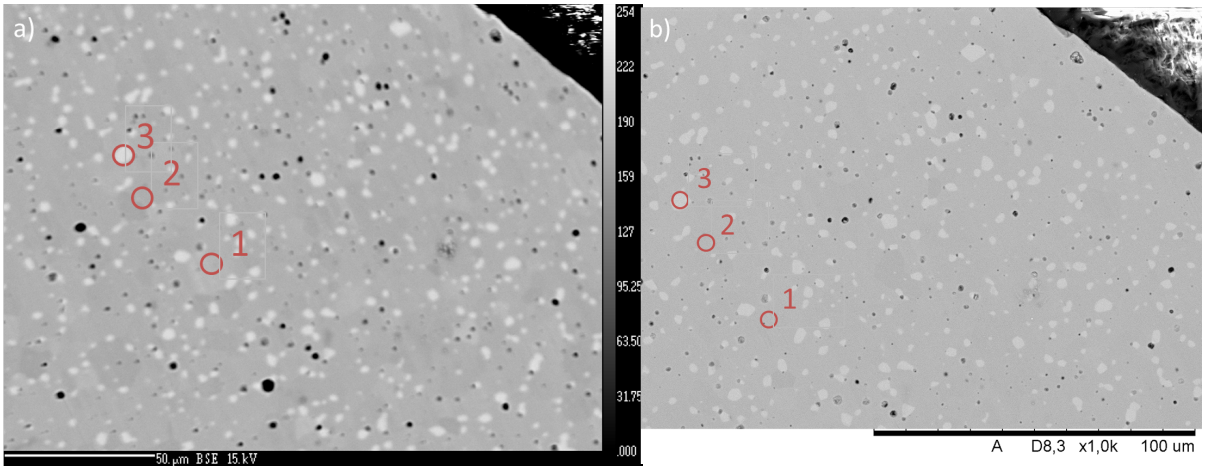

Area	EMPA Mn/Ca ratio	Error[%] Mn	Error[%] Ca	SEM Mn/Ca ratio	Error[%] Mn	Error[%] Ca
1	1.04	1.1	0.2	0.99	1.1	0.8
2	1.05	1.1	0.2	1.0	1.1	0.8
3	1.47	1.2	0.2	1.62	1.4	0.9

Figure 4.6: Phase analysis of CMO_UiO_7.47 with EMPA a) and SEM b) showing area 1 and 2 correspoding to main phase $CaMnO_3$ and brighter area 3 corresponding to secondary phase $CaMn_2O_4$.

Effect of sintering temperature

The effect of sintering temperature on grain size and density were investigated by sintering three samples from the same batch, CMO_UiO_0 (batch 1), at different temperatures, 1200 °C, 1250 °C and 1300 °C with same dwell time, 20 h. Figure (4.7) shows SEM micrographs of the three sintered samples unpolished, a) - c) and polished d) - f). An increase in density with temperature is observed in both a) - c) and d) - e), however f) seem to deviate from the trend, and from what is seen on the unpolished surface c), and might not be representative for the specimen as a whole. The grain size is observed to be increasing with temperature, a) - c), from $\sim 5\,\mu m$ to $\sim 25\,\mu m$. The distribution of grains with different size in one sample, also appear to be larger.

As sintered at 1200 °C

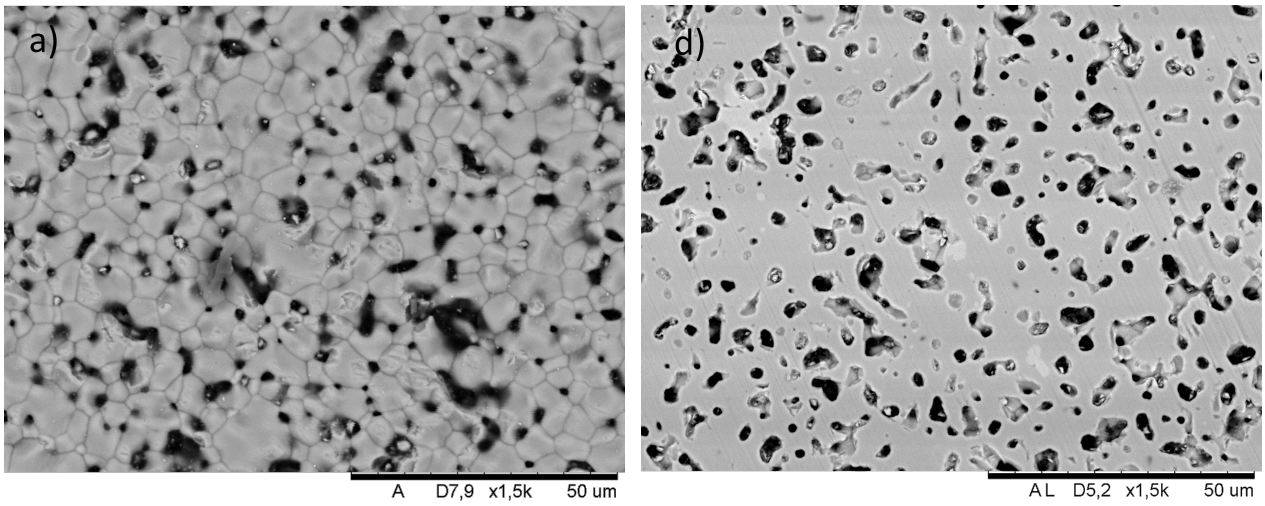

As sintered at 1250 °C

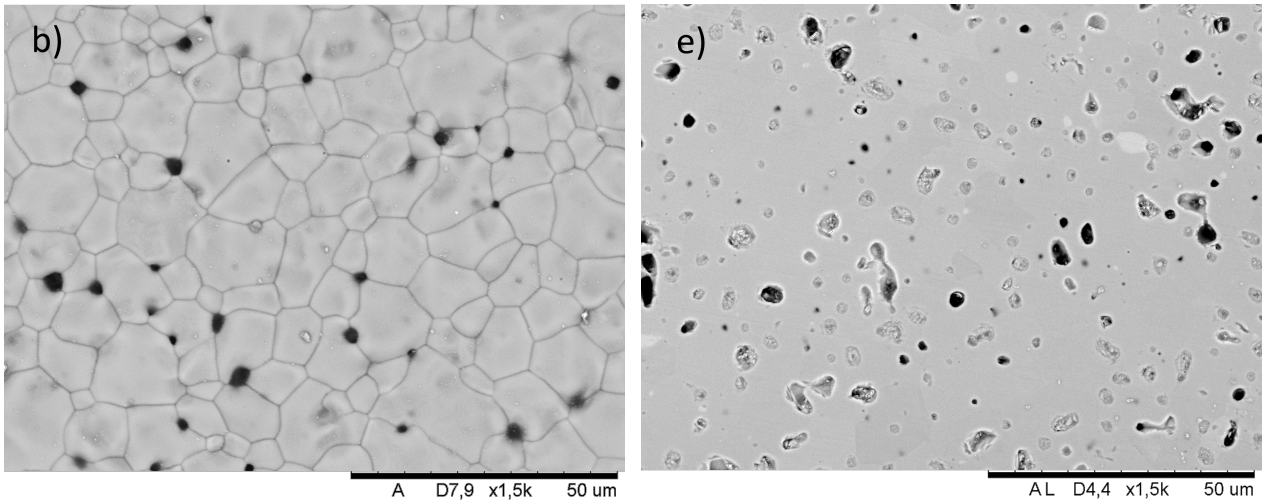

As sintered at 1300 °C

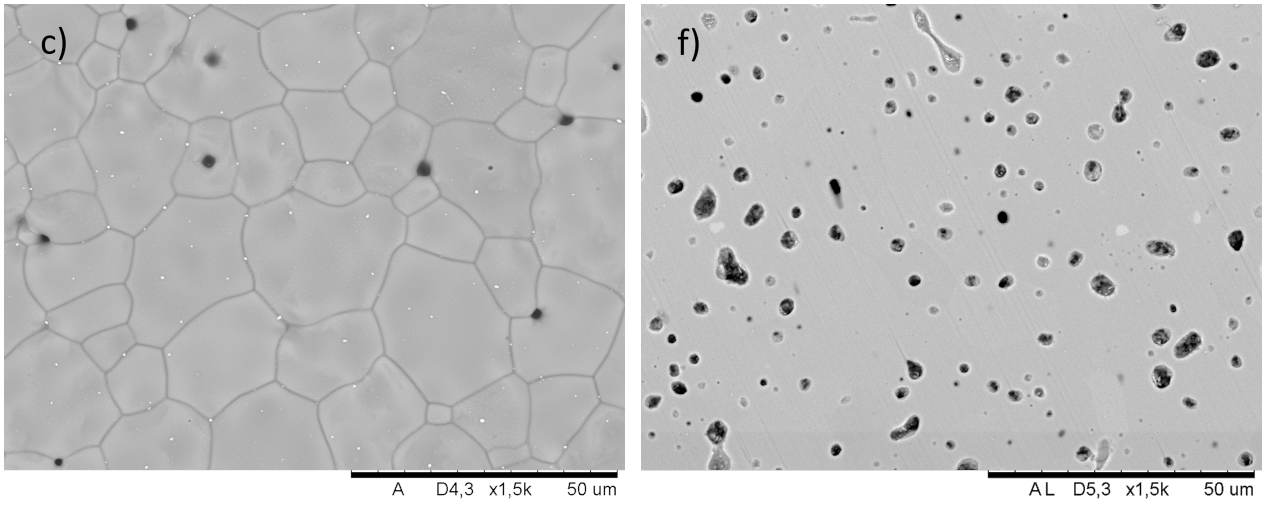

Figure 4.7: Backscatterd SEM micrographs of nominally stoichiometric $CaMnO_3$ (CMO_UiO) for unpolished samples (left), with sintering temperature a) 1200 °C, b) 1250 °C and c) 1300 °C and polished samples (right) with sintering temperatures d) 1200 °C, e) 1250 °C and f) 1300 °C

Micro structure of CMO_NTNU samples

Samples received from collaborations at NTNU were also investigated with XRD, presented in Appendix G, and SEM. The synthesis was presented in section 3.1.2, where the main difference is the preparation of precursor powder in addition to sintering and annealing in reducing atmosphere. Phase analysis from XRD of CMO_NTNU samples show, in analogue to UiO sintered samples, the presence of two phases, $CaMnO_3$ and $CaMn_2O_4$. Figure (4.8) is showing SEM micrographs of CMO_NTNU samples, $CaMn_{1+y}O_{1-\delta}$ with Mn excess y = 0.036 a) and c) and y = 0.074 b) and d) as sintered (left) and polished (right).

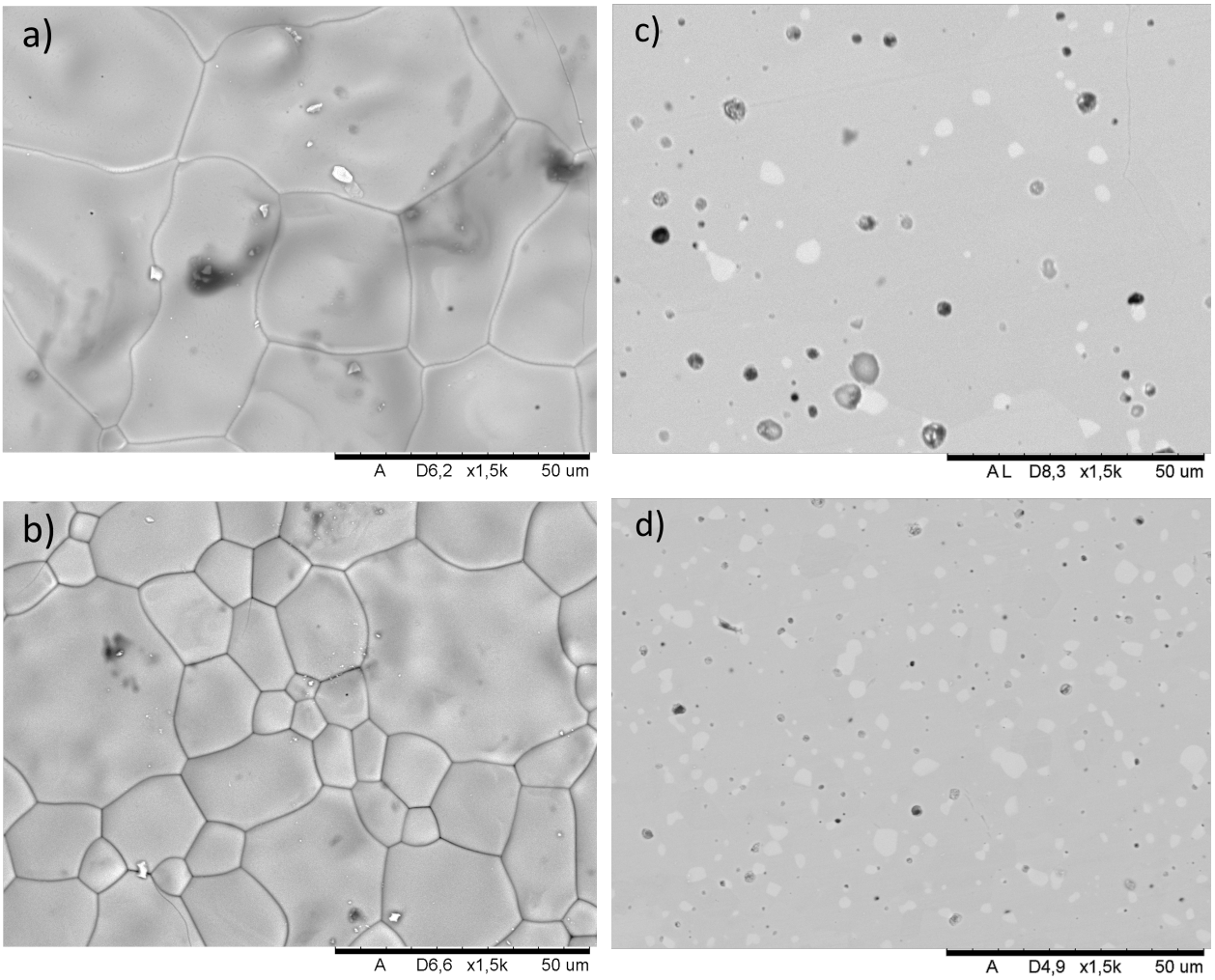

Figure 4.8: Backscattered SEM micrographs of surface as sintered (left), and polished (right) sample (CMO_NTNU) with nominal Mn excess a) and c) 3.66 at%, b) and d) 7.47 at%. Where a) - b) indicate a decrease in grain size and c) - d) increase in secondary phase with increasing Mn content. Low intensity matrix corresponds to $CaMnO_3$ and the brighter precipitates to $CaMn_2O_4$. The dark areas corresponds to pores.

[H]

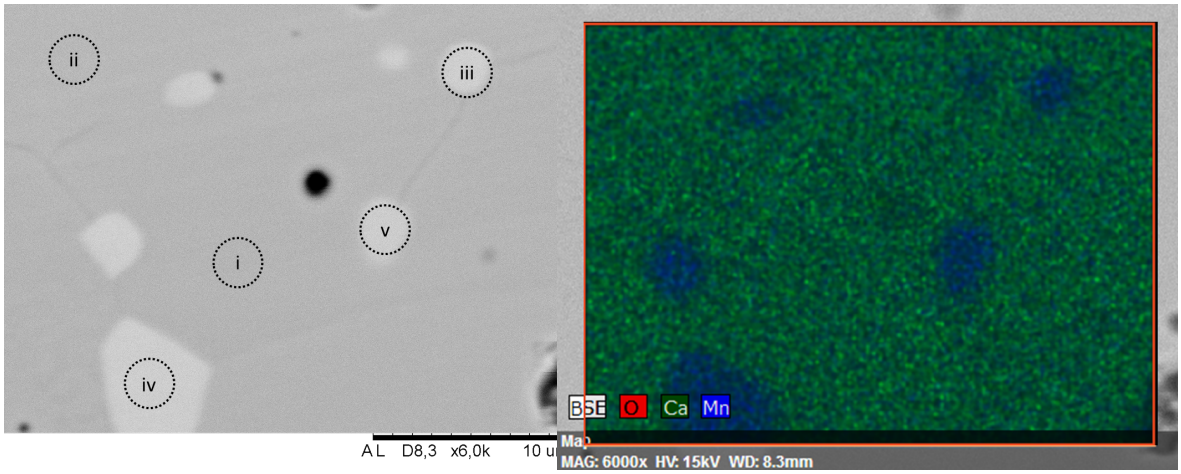

Area	(i)	(ii)	(iii)	(iv)	(v)
Mn/Ca ratio	0.96	0.95	1.58	1.60	1.49

Figure 4.9: EDS analysis of CMO_UiO_3.66 (a) showing low intensity matrix corresponding to $CaMnO_3$ and brighter area secondary phase $CaMn_2O_4$.

These are comparable to the micrographs of UiO synthesised samples, $CaMn_{1+y}O_{1-\delta}$ with Mn excess y = 0.036 a) and c) and y = 0.074, d) and e) shown in figure (4.3) and figure (4.4). The darker area correspond to pores. The grain size of sample y = 0.036, a), is ∼30 µm while sample y = 0.074 has a larger distribution of grain size, in the range of ∼10 - 50 µm. In the same manner as for the inhouse synthesised samples, grain size decrease with increasing Mn content together with an increase in grain size distribution. Secondary phase precipitates increase in number with increasing Mn content and stay in the size range ∼ 2-5 µm. In analogue to UiO synthesised samples, EDS of both CMO_NTNU samples show low intensity matrix with an average Mn/Ca ratio close to 1, while the brighter areas has Mn/Ca ration close to 1.5. An example of an EDS analysis of CMO_NTNU_3.66 is shown in figure (4.9).

Nano-structural investigations

Further phase analysis were performed using TEM, focusing on investigating possible nano-precipitates with the $CaMnO_3$ matrix. In order to maximize the probability of observing precipitates, TEM specimens were prepared from the samples with the highest Mn content, CMO_UiO_7.47 and CMO_NTNU_7.47. The TEM specimens were investigated using diffraction, imaging and EDS. Both specimens were investigated as powder specimen, while CMO_UiO_7.47 was in addition investigated as a FIB specimen.
Figure (4.10) show diffraction patterns (DP) from the $CaMnO_3$ matrix, from specimen CMO_UiO_7.47 with zone axis [100] (left) , [101] (middle) and [111] (right).

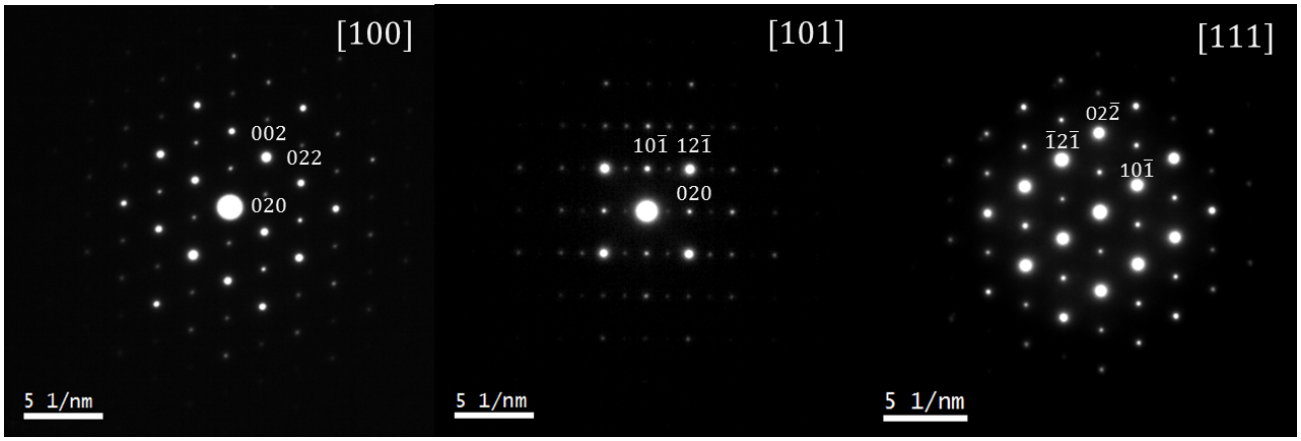

Figure 4.10: SADP with zone axis [100] (left), [101] (middle) and [111] (right) from main phase $CaMnO_3$ of specimen CMO_UiO_7.47Mn

The DP from zone axis [100] show strong reflections 002, 020 and 022, and is in good agreement with simulated DPs, presented in Appendix H. For DP for zone axis [101] both $10\bar{1}$, $12\bar{1}$ and 020 is strong in addition to observed intensity from the kinematic forbidden 010 reflection. The intensity of the 010 reflection is most likely due to multiple scattering. When disregarding the kinematic forbidden reflections, the DP is in good agreement with the simulated DPs. Also the DP from [111] zone axis in agreement with simulated DPs, when disregarding the intensity from forbidden $01\bar{1}$ reflection, which arises due to multiple scattering in the same manner as for the [101] DP. The $10\bar{1}$, $02\bar{2}$ and $\bar{1}2\bar{1}$ show strong intensity in analogue to the simulated patterns. No superstructures or splitting of reflections are observed in these SADPs.
Figure (4.11) show diffraction patterns of $CaMnO_3$ matrix, from specimen CMO_NTNU_7.47 with zone axis [010] (left), [111] (middle) and [210] (right).

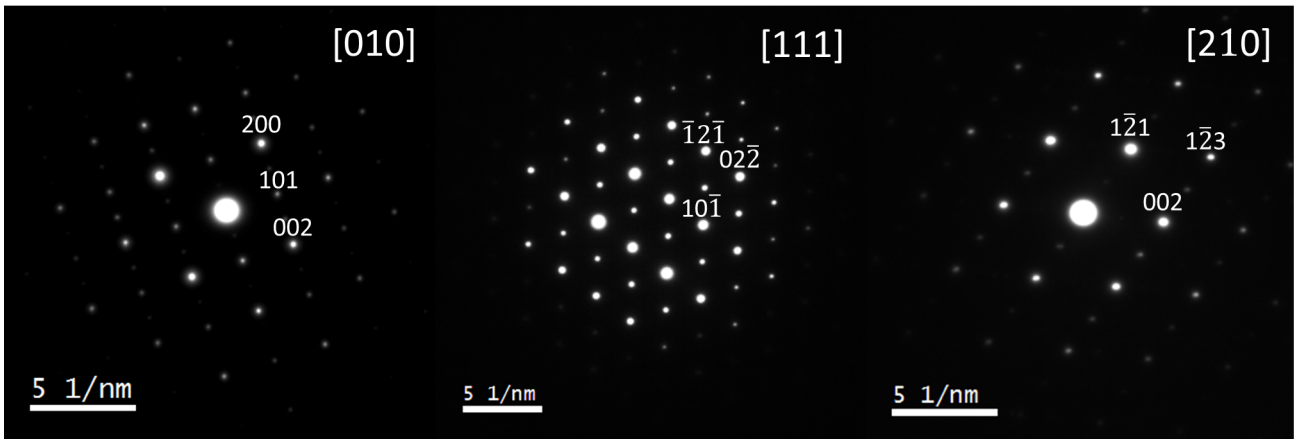

Figure 4.11: SADP with zone axis [010] (left), [111] (middle) and [210] (right) from main phase $CaMnO_3$ of specimen CMO_NTNU_7.47Mn

The [010] DP show strong reflection 002 and 200 which is in analogue to simulated diffraction patterns. No extra reflections and indications of superstructures are seen. The [111] DP similarly fits well with simulated data, however, the $01\bar{1}$ reflection has intensity even though it is forbidden. The [210] DP show strong reflections $1\bar{2}1$ and 002, however, also intensity between 000 and $1\bar{2}1$ reflections are observed, which should be forbidden. This might be due to, in analogue with the previous DP a result of multiple scattering. The main phase, $CaMnO_3$, and expected secondary phase, $CaMn_2O_4$, were identified SAD. As seen in the high resolution TEM image (HRTEM) from zone axis [101] and [102], figure (4.12) a) and b) respectively, all specimen show large areas with perfect crystallinity, without any precipitates. Figure (4.12) a) and b) show high resolution TEM (HRTEM) images of the $CaMnO_3$ matrix of specimen CMO_UiO_7.47, with corresponding FFTs. The HRTEM images are obtained with zone axis [101], a) and [102] b). Large areas with perfect crystallinity, and no precipitates, are observed. This implies that there are no obvious solubility of Mn in $CaMnO_3$ enabling nano-precipitates within the $CaMnO_3$ grains. There was further not observed any evident differences in the nano-structure between the CMO_UiO and CMO_NTNU specimens, indicating that synthesis method does not effect the nano-structure. In section 1.4.1, the phase transition from high temperature cubic, to low temperature orthorhombic crystal structure was introduced. The characteristic elongation of one of the cubic unit cell basis vectors, into the orthorhombic $\vec{b}$, could arise in all three cubic unit cell vector directions. This might results in an orientation relationship between grains.

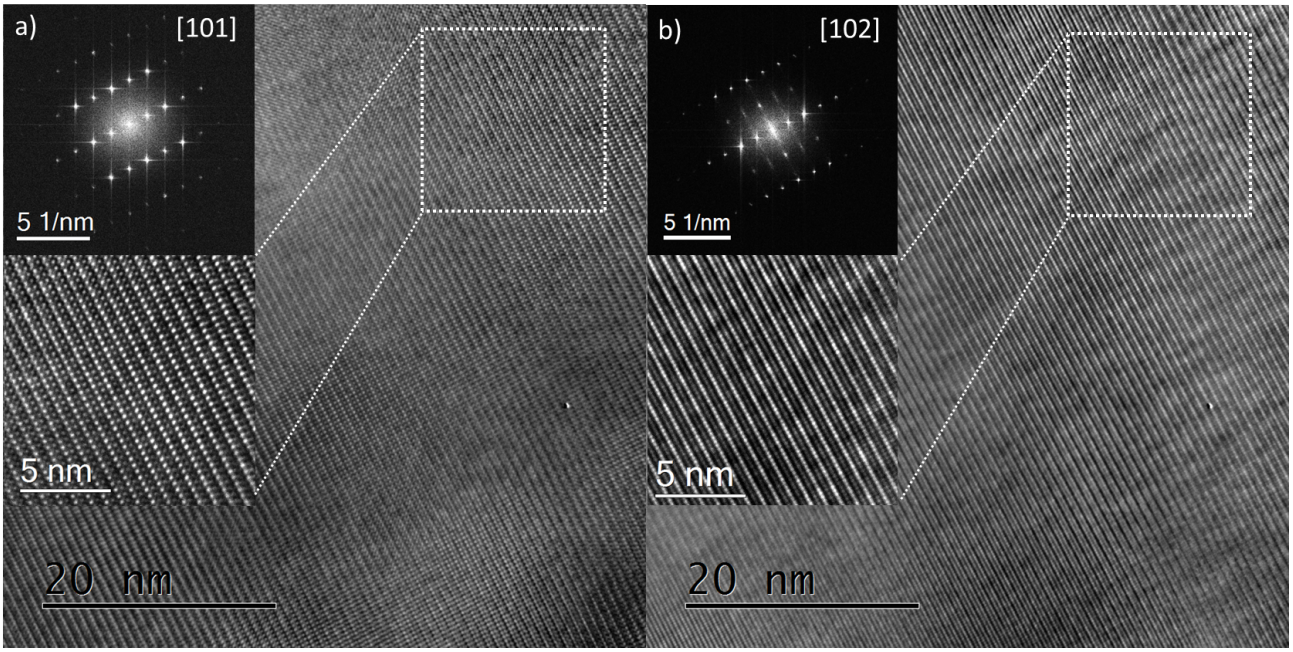

Figure 4.12: HRTEM images of main phase $CaMnO_3$ with zone axis a) [101] and b) [210]

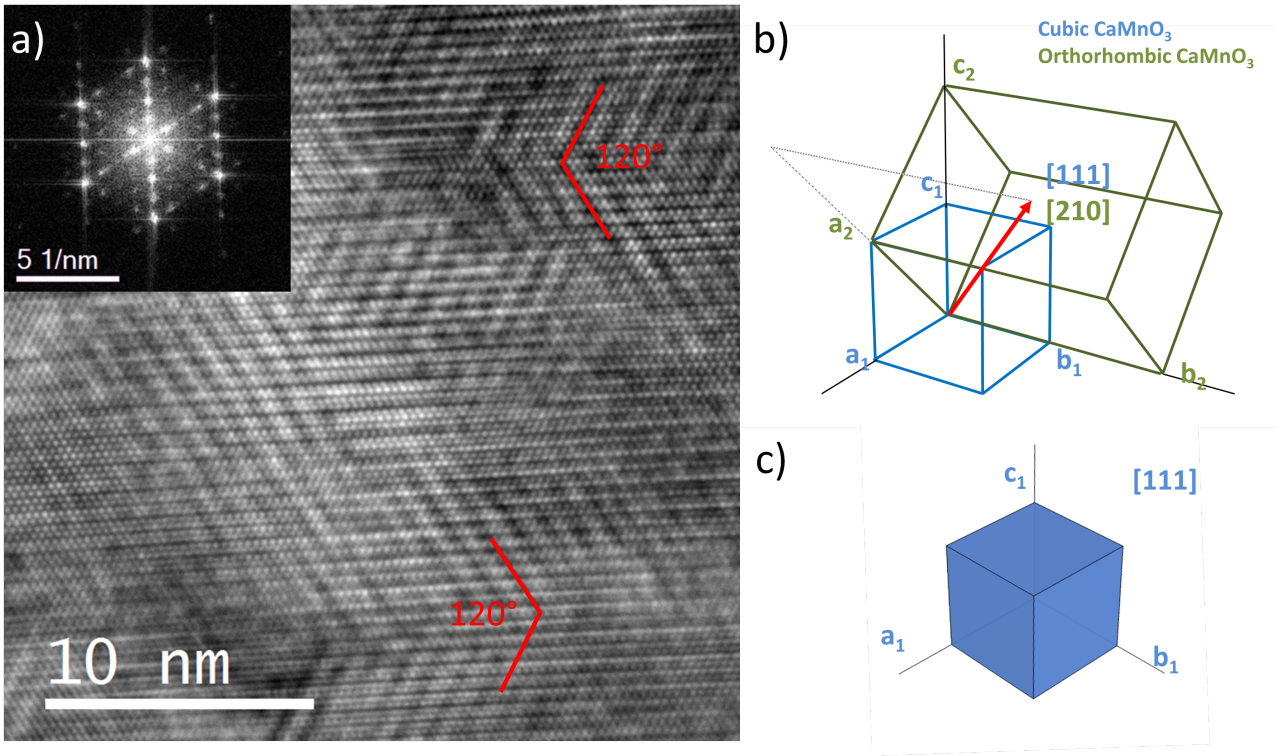

Figure 4.13: a) HRTEM with overall zone axis [210] and corresponding FFT for CMO_NTNU_7.47, showing areas with related but different crystal orientation. b) Illustration of the relation of high temperature cubic and room temperature orthorhombic with zone axis [210] marked in red showing the corresponding [111] direction in the cubic phase. c) An illustration of how cubic $CaMnO_3$ look down [111] zone axis.

Figure (4.12) a) show a HRTEM image of a twin boundary between two grains with zone axis [101] and [010] and the corresponding FFT. The basis vector $\vec{b}$ of the orthorhombic unit cell is marked in the figure where $\vec{b}$ is parallel to the grain boundary in the grain oriented with zone axis [101] and points out of the image for the grain oriented with zone axis [010]. The arrows points out areas which look like distorted areas but with closer examination is found to be contrast changes due to uneven specimen surface. Figure (4.12) b) show a magnification of the marked area in a), with blue circles marking the Mn atomic colums, displaying the sharp grain boundary. The $CaMnO_3$ unit cell as seen with [101] and [010] zone axis, corresponding to the grain orientation is illustrated in figure (4.12) c). An illustration of the structural relation between the high and low temperature structure is presented in figure (4.13) b). The red arrow marks the zone axis for the HRTEM image in a) which corresponds to [210] direction in the orthorhombic and [111] in the cubic phase. Figure (4.13) c) show the cubic unit cell viewed down the [111] zone axis, included to illustrate how the marked angles over grain boundaries in figure a) correlated to the angles in the cubic structure.

Areas containing different kinds of distortions were also observed. However, these were only

observed occasionally, thus was not a representation of the general picture. Whether these distortions originates due to local variation in composition, or if they would also exist in a stoichiometric compound, has not been further investigated. However, it should be noted that these were observed in both CMO_UiO and CMO_NTNU specimens.With powder specimens, the knowledge of where in the bulk sample the investigation takes place is lost. Unexpected phases has been observed on sample surface of CMO_UiO_7.47 and raises a concern of sample stability. The CMO_UiO_7.47 specimen was investigated by collaborations at Wroclaw Research Centre EIT+, by Sandeep Gorantla. Some obtained results from this investigation are presented in Appendix I, however the full characterization was beyond the scope of this work. XRD between the synthesis steps and after measurements was performed for sample CMO_UiO_3.66 to check sample stability, included in Appendix J, showing same structure before and after sintering and measurements. However, small concentrations of another phase might not be detected by XRD.

4.2 Thermoelectric properties

In this section the thermoelectric properties of all UiO synthesized samples, presented in table (4.1), are reported.

4.2.1 Electrical resistivity

The electrical resistivity of samples $CaMn_{1+y}O_3$ with composition y = 0, 0.020 , 0.036, 0.074 and 0.10 was measured from 50 to 600 °C in air, and are presented in figure (4.14) as a function of temperature (left) and Mn composition (right). The resistivity is in the range of 70 - 100 mOhm cm at room temperature, and decreasing to 25 - 50 mOhm cm at higher temperatures. No obvious trend in resistivity with the variation of Mn content is observed. If the influence of Mn content is small, it might be masked by other variables such as sample density. Potential introduction of impurities or defects might further vary charge carrier concentrations and lead to a variation in resistivity. A change in the slope of the resistivity at $\sim$ 500 °C was observed, which is also reported in previous work, but of which the origin is unknown [30,32,87]. Calcium manganate oxide undergoes structural changes at elevated temperatures, however, this is expected to happen well above $\sim$ 500 °C [30].

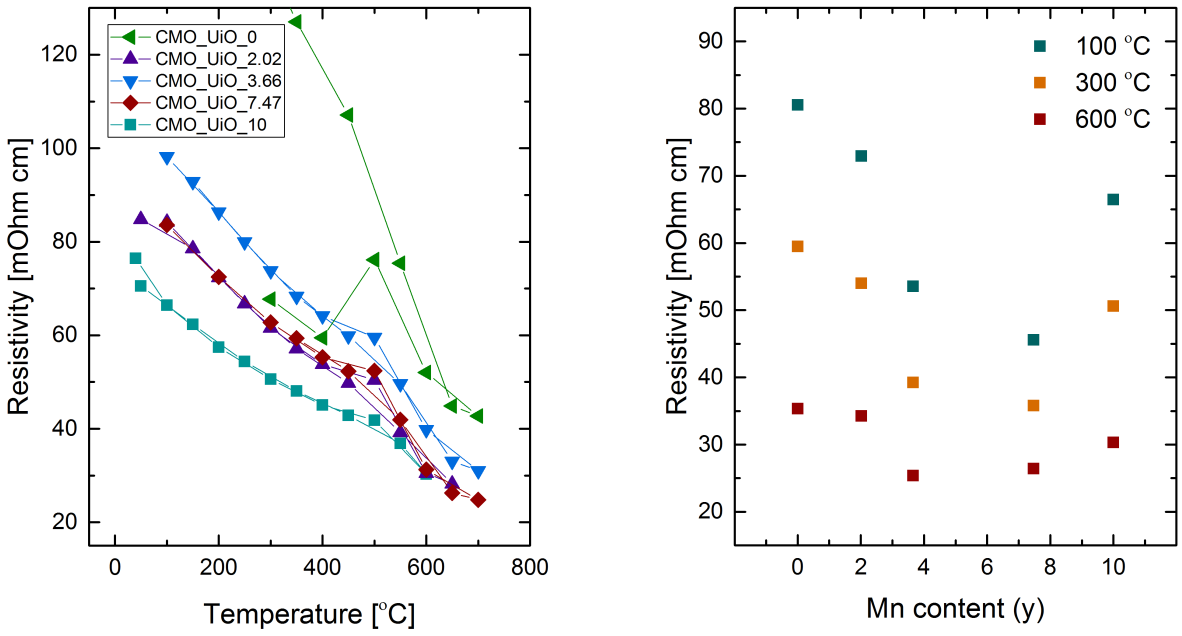

Figure 4.14: Resistivity as a function of temperature for $CaMn_{1+y}O_{3\pm\delta}$ with y = 0, 0.020 , 0.036, 0.074 and 0.10 (left) and Mn content (y) at 100 °C, 300 °C and 600 °C (right).

In addition the oxygen stoichiometry of the structure is known to vary, forming oxygen vacancies with compensating electronic defects, leading to a decrease in resistivity. A further investigation of this slope change is needed and it would be interesting to perform calorimetric analysis on this samples. To investigate the nature of the conduction, the natural logarithm of conductivity times temperature, $\ln(\sigma T)$, was plotted against the inverse temperature, $1/T$, in an Arrhenius type plot, figure (4.15). Conductivity increase exponentially with temperature, confirming the earlier suggested hopping of localised small polarons as the dominant charge transport mechanism. No apparent overall incline was observed, instead it might be interpreted as two slopes, one at lower and one at higher temperatures, with slope change at $\sim 500\,^{\circ}\mathrm{C}$. Both slopes and thus activation energy of conduction were then evaluated through the Arrhenius equation for all compositions, figure (4.15), showing an activation energy of ~ 60 meV at lower and ~ 140 meV at higher temperature.

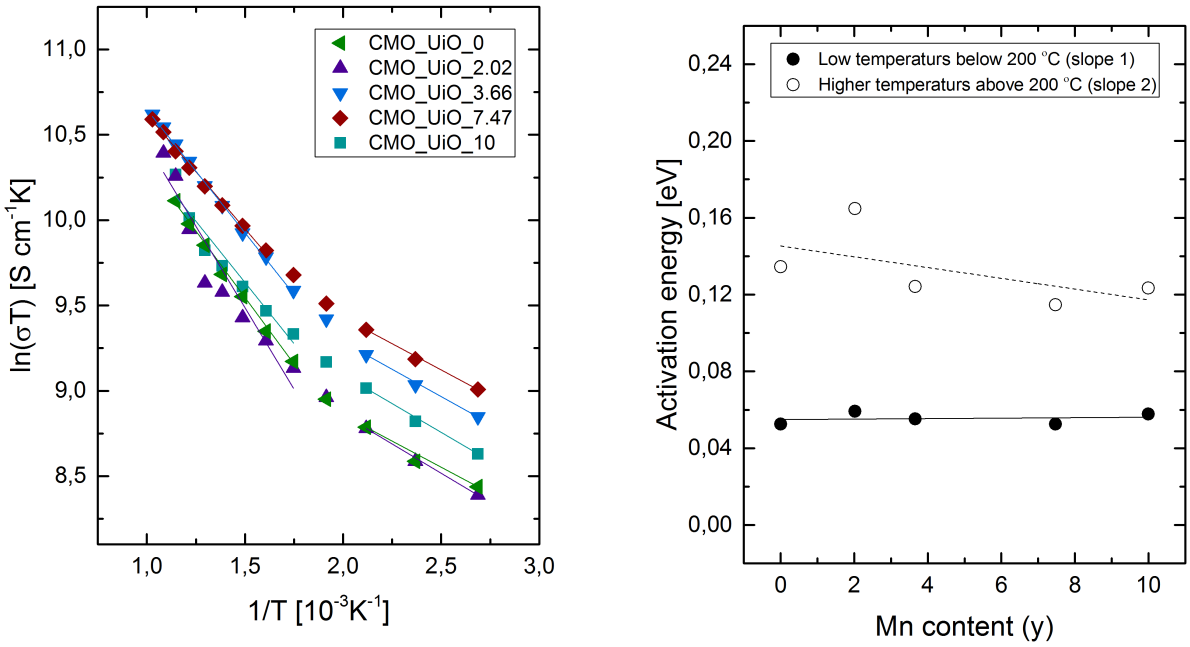

Figure 4.15: Arrhenius plot, ln(σT) vs 1/T (left) and corresponding activation energies as a function of Mn content (right).

4.2.2 Seebeck coefficient

The Seebeck coefficient was measured simultaneously with resistivity, for several samples with compositions $CaMn_{1+y}O_3$ with y = 0, 0.020 , 0.036, 0.074 and 0.1 from 50 to 600 °C, shown in figure (4.16). The Seebeck coefficient, figure (4.16), is negative, indicating that the material is an n-type conductor. Mn rich samples show Seebeck coefficients ranging from -300 μVK^{-1} at room temperature to -200 μVK^{-1} at 600 °C, while at intermediate temperature have a spread of $\sim$ 50 μVK^{-1}. No trend in Seebeck coefficient with increasing Mn content is observed, in analogy with the resistivity of the samples. However, the nominally stoichiometric sample shows a higher absolute Seebeck coefficient than the Mn rich samples, and is in agreement with previous reported values [30, 32, 87]. The Seebeck coefficient is not heavily dependent upon microstructure, porosity or impurities, and is mainly influenced by charge carrier concentration, with decreasing absolute values with increasing number of carriers.

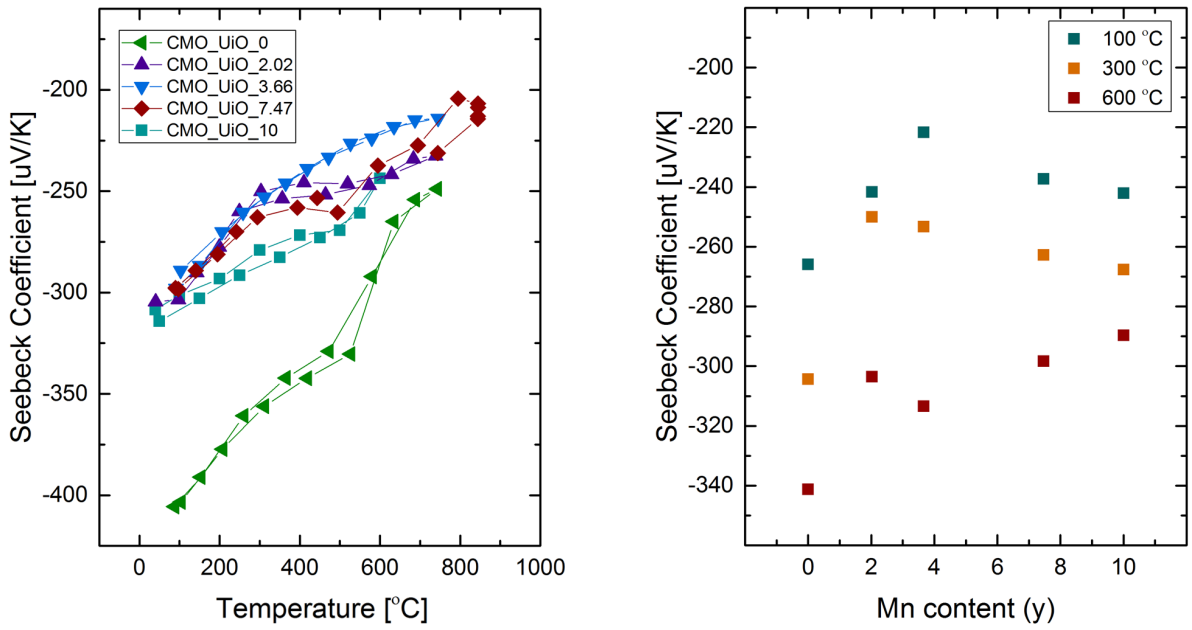

Figure 4.16: Seebeck coefficient as a function of temperature for $CaMn_{1+y}O_{3\pm\delta}$ with y = 0, 0.020 , 0.036, 0.074 and 0.10 (left) and Mn content (y) at 100 °C, 300 °C and 600 °C (right).

4.2.3 Thermal conductivity

Thermal diffusivity was measured with Laser Flash technique and the thermal conductivity calculated from the results. Samples with compositions $CaMn_{1+y}O_3$ with y = 0, 0.020 , 0.036, 0.074 and 0.1 were investigated from 50 to 600 °C and the results are presented in figure (4.17). For all measured samples, the thermal conductivity decreases with increasing temperature but with different steepness of slope. The measured values range from 2.3 W $m^{-1}K^{-1}$ to 3.6 W $m^{-1}K^{-1}$ at room temperature and from 1.9 W $m^{-1}K^{-1}$ to 2.4 W $m^{-1}K^{-1}$ at 600 ° C. The spread in thermal conductivity between the samples are less than $\sim$ 0.3 W $m^{-1}K^{-1}$, and no clear trend is found with increasing Mn content.

The contribution from the lattice thermal conductivity was obtained by subtracting the electronic contribution, found through Wiedemann Franz law, presented in equation (1.6), from the total, measured, thermal conductivity. The calculated results for sample CMO_UiO _7.47 (a) as a function of temperature is presented in figure (4.18) (left) as an illustrating example. The total, lattice and electronic contribution are plotted as a function of Mn content at 600 °C (right). The lattice conductivity, similar to the total thermal conductivity, is decreasing with temperature. This is expected from theory with domination of Umklapp scattering processes at higher temperatures.

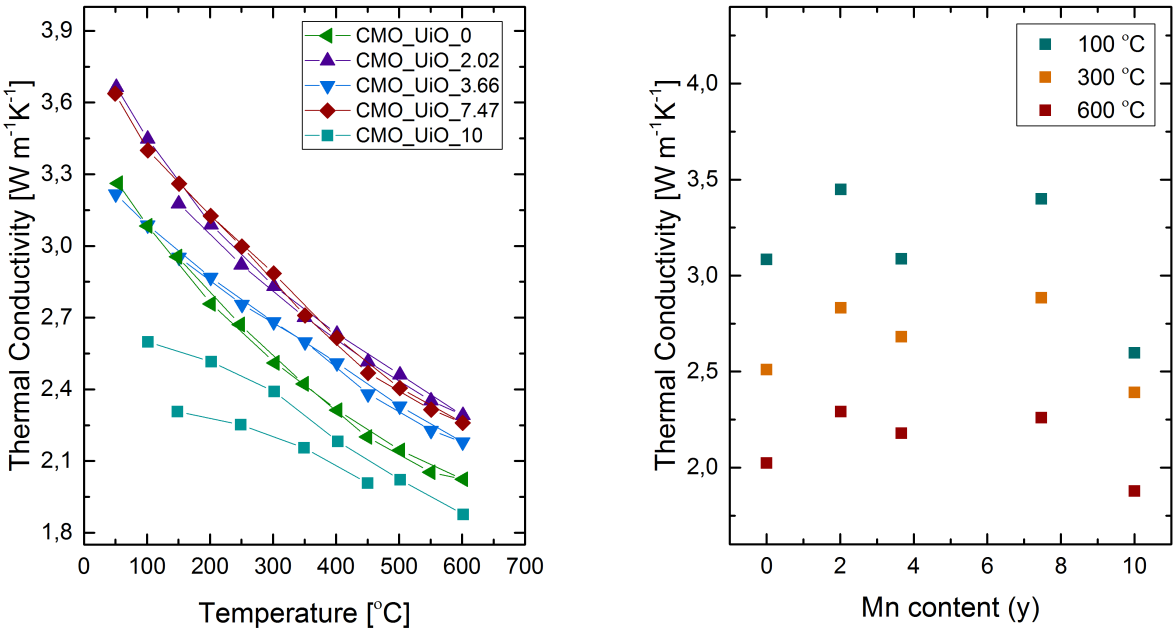

Figure 4.17: Thermal conductivity as a function of temperature for $CaMn_{1+y}O_{3\pm\delta}$ withy = 0, 0.020 , 0.036, 0.074 and 0.10 (left) and Mn content (y) at 100 °C, 300 °C and 600 °C (right).

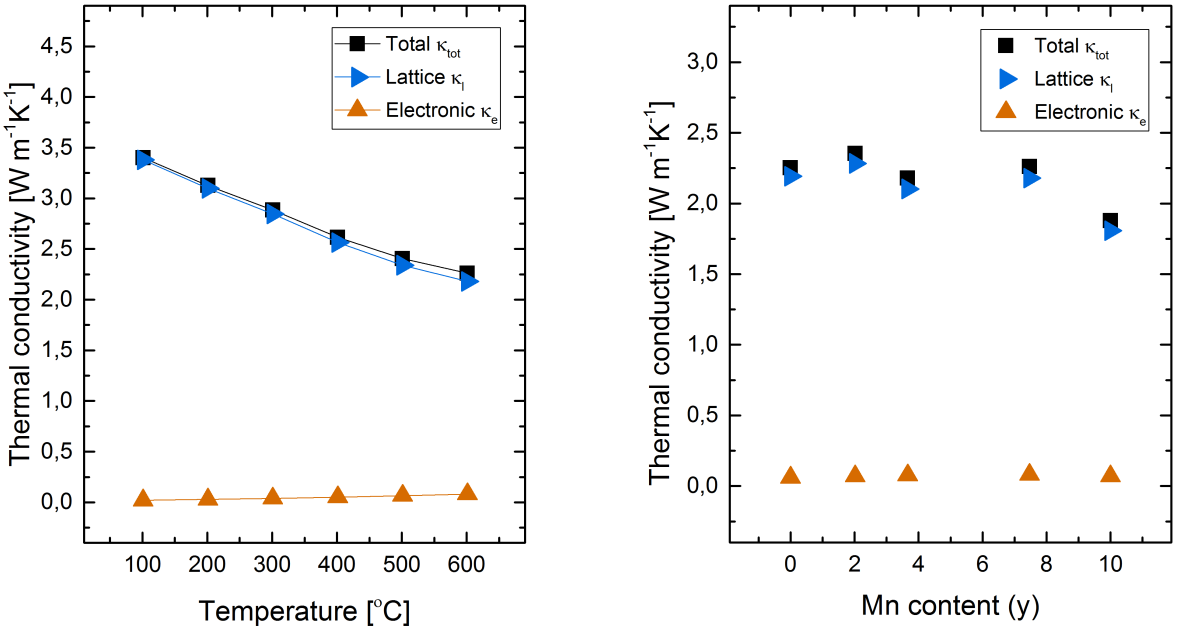

Figure 4.18: Lattice, electronic and total thermal conductivity for CMO_UiO_7.47 as a function of temperature (left) and Mn content (right).

The electronic contribution is slightly increasing. The electronic contribution make up 0.6 % at 100 °C and 3.7 % at 600 °C of the total conductivity, which is regarded as negligible in the further discussion. The initial electrical and thermal measurements performed on these samples do not reveal a dependency upon Mn content and investigations into the reproducibility of measurements were performed. The first approach was correcting for density variations, considering that both resistivity and thermal conductivity are heavily influenced by sample porosity.

Porosity corrections

Several models have been applied to correct for the porosity of samples, in order to directly compare the properties as a function of Mn content. Figure (4.19) show porosity corrections of measured thermal conductivity, presented in section (4.2.3), by three different models, presented in theory chapter section (2.6.7), i) Maxwell Garnett model, ii) correction term presented by Shafiro & Kachanov and iii) Klemens *et al.* When applying the models, the values increase by a factor ∼0.2. The increase is expected due to denser samples having less scattering centres and thus a higher thermal conductivity.

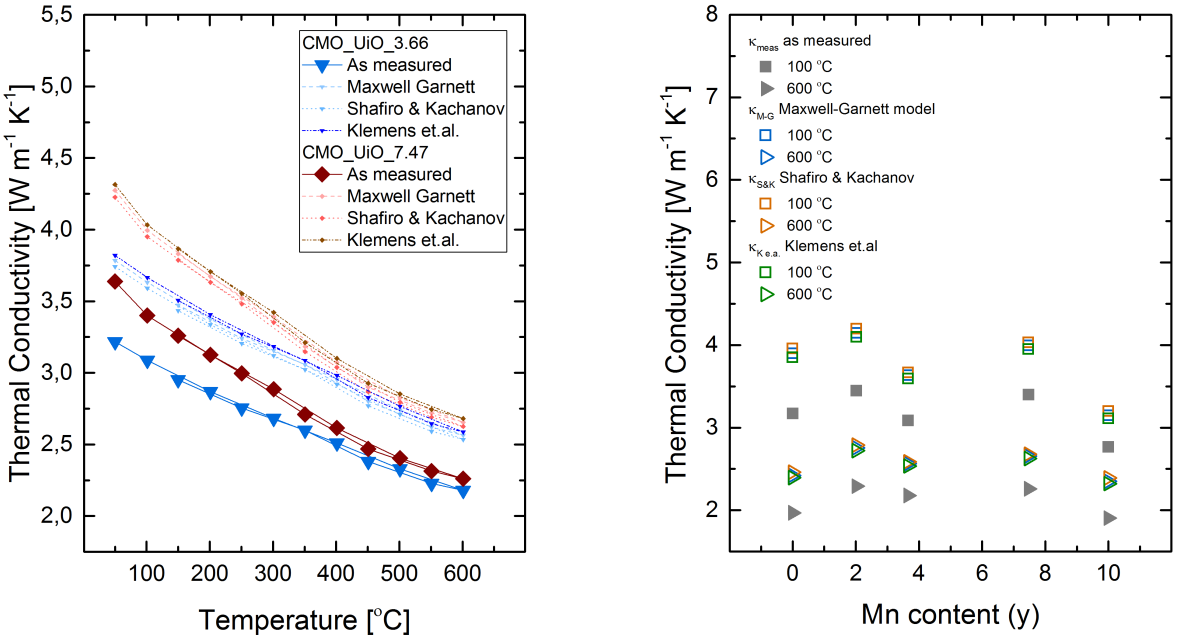

Figure 4.19: Effect of correction on the thermal conductivity of CMO_UiO _3.66 and CMO_UiO _7.47 as a function of temperature (left) and Mn content (y) at 100 °C, 300 °C and 600 °C (right).

Furthermore, all models return approximately the same shift and the discrepancy between them is $\sim$0.05 W m^{-1} K^{-1}, equal to $\sim$5 % of the initial value, well within the error estimation of the measurement itself. From this point, the data is only corrected using the model presented by Klemens. Still, no trend or dependency upon Mn content was revealed when applying the correction models and the reproducibility and accuracy in the measurements might be brought into question. A comprehensive study of the measurement condition and setup was performed, and is presented in section 4.3.

4.2.4 Thermoelectric figure of merit

The thermoelectric figure-of-merit, zT was found through equation (1.5) from measured values of electrical resistivity, Seebeck coefficient and thermal conductivity. The obtained zT is presented in figure (4.20) from 50 - 600 °C. zT for the materials ranges from 0.01 at 50 °C to 0.07 at 600 °C, with a spread of $\sim$ 0.01 at lower and 0.02 at higher temperatures between samples with different Mn content. No trend as a function of Mn composition is observed as expected from the individual measurements.

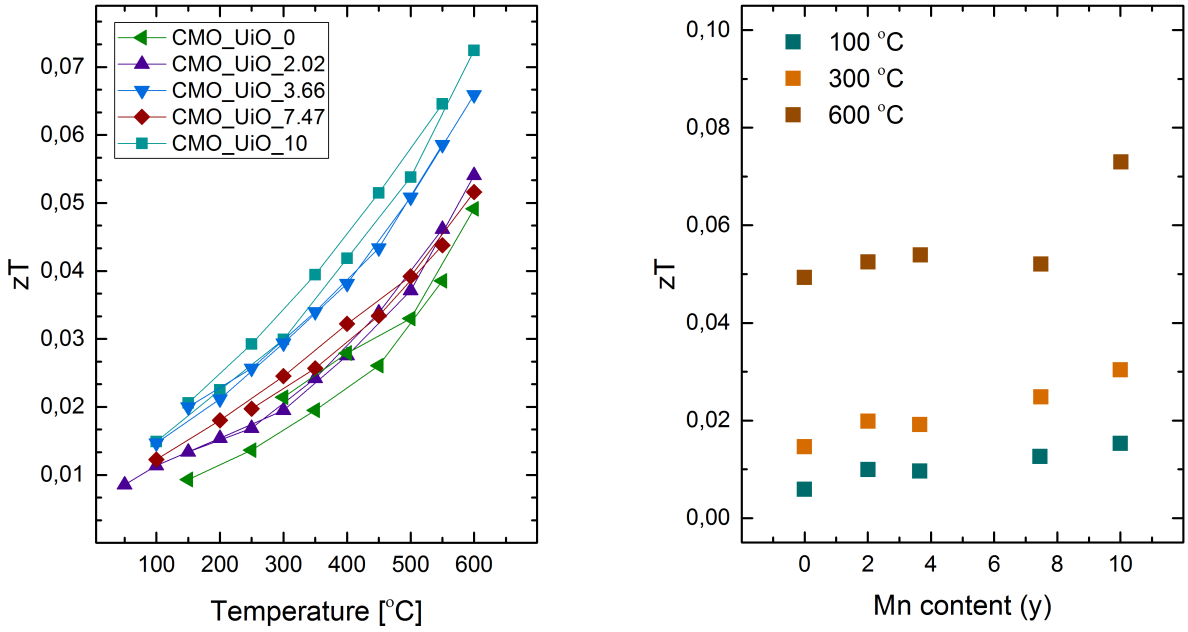

Figure 4.20: zT as a function of temperature (left) for $CaMn_{1+y}O_{3\pm\delta}$ withy = 0, 0.020 , 0.036, 0.074 and 0.10 (left) and Mn content (y) at 100 °C, 300 °C and 600 °C (right).

4.3 Investigation of the reproducibility of measurements

4.3.1 Density dependencies on thermoelectric measurements

Three pellet samples from the same batch, CMO_UiO_0 of nominally stoichiometric $CaMnO_3$, were sintered at different temperatures, 1200 °C, 1250 °C and 1300 °C, to obtain different densities. The samples were investigated to reveal the thermoelectric measurements dependency on porosity. Thermal conductivity measurements, corrected with the model presented by Klemens, of these samples are presented in figure (4.21) (left), in addition to resistivity and Seebeck coefficients in figure (4.21) (right). Surprisingly, the measured electrical resistivity and thermal conductivity are higher for the most dense sample, (c), than the second most dense sample, (b), which contradicts what is intuitive. The least dense sample, (a), has a thermal conductivity lying between the most and second most dense sample. Furthermore it holds the highest absolute Seebeck coefficient and resistance.

The measurement also reveals a change in properties of sample (a), displaying a different curve, upon heating and cooling. This difference is also observed in other samples from first heating cycle, figure (4.21) (left), and might be due to filling of oxygen vacancies formed due to too rapid cooling when sintering the samples.

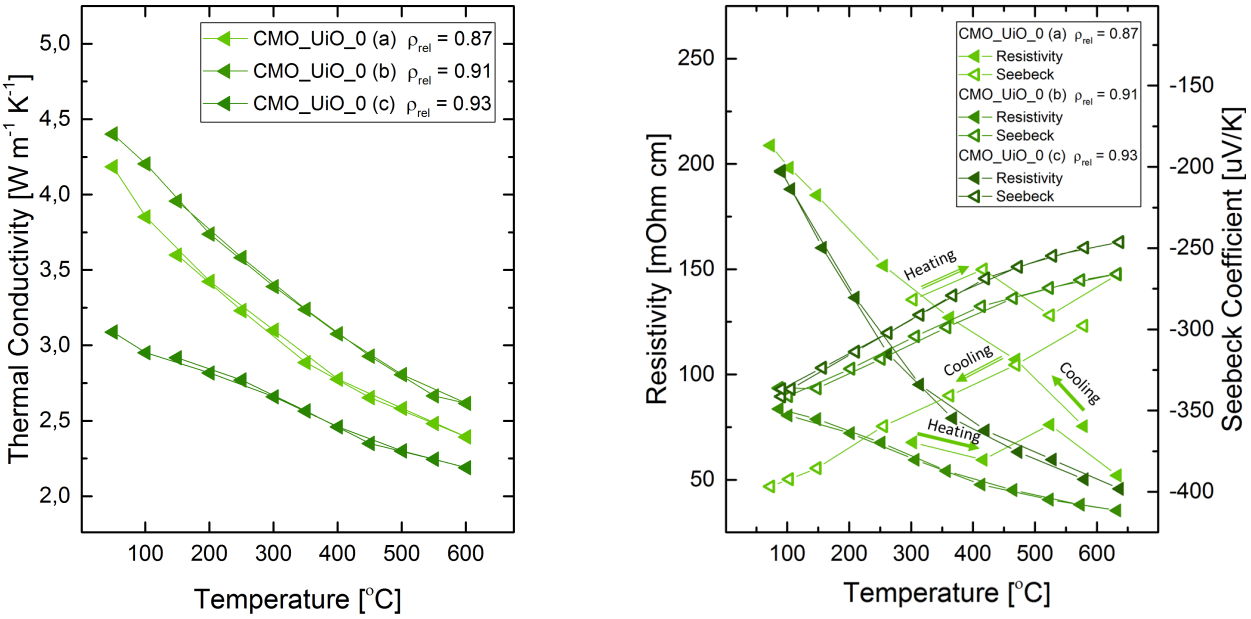

Figure 4.21: Thermal conductivity (left), Resistivity and Seebeck coefficient (right) of CMO_UiO_0 (a), (b) and (c) with same composition but different densities.

Considering the Seebeck effect not being dependent on porosity, expected values of the Seebeck coefficient for the three samples would be the same which is true for the most and second most dense sample, (b) and (c). However the least dense sample, (a), deviates from (b) and (c) upon cooling. This might be due to reacting with contamination in the cell, causing defects in the sample, contemplating that the Seebeck coefficient is inversely proportional to charge carrier concentration. Then again it would be expected that the induced defects would lead to a decrease in resistivity in contrary to the observed increase.
No conclusion was reached from the investigation of density dependency of thermoelectric measurements, and the spread in obtained data might be due to the uncertainty of the measurement set-up itself, in addition to microstructural variations of the three samples.

4.3.2 Contact placing and reproducibility of resistivity and Seebeck measurements

The Van der Pauw measurement assumes point contact placing on the circumference of the sample, which might not be adequately met and may influence the results of the electrical measurements. The reproducibility of the measurements were investigated by cycling a sample up

and down in temperature under same conditions, removed from measurement cell and replaced with new contact placings, and cycled anew. The obtained data for sample CMO_UiO_3.66 (b) is shown as an example in figure (4.22), revealing a variation in resistivity of $\sim$ 15 mOhm cm at low temperatures and $\sim$ 2 mOhm cm at higher temperatures between the two contact placings. Potential microcracks induced while handling the sample, would also be a source of the variations in resistivity, though difficult to control and quantify. However, it would then be expected that the resistivity was increased and not decreased by the second measurement cycle and is disregarded in this case. The Seebeck coefficient of the sample from the 1st to 2nd run are overlaying, except for the very first heating, which has shown to have similar behaviour for all samples. This indicates that the Seebeck coefficient is not dependent upon the contact placing and is reproducible.

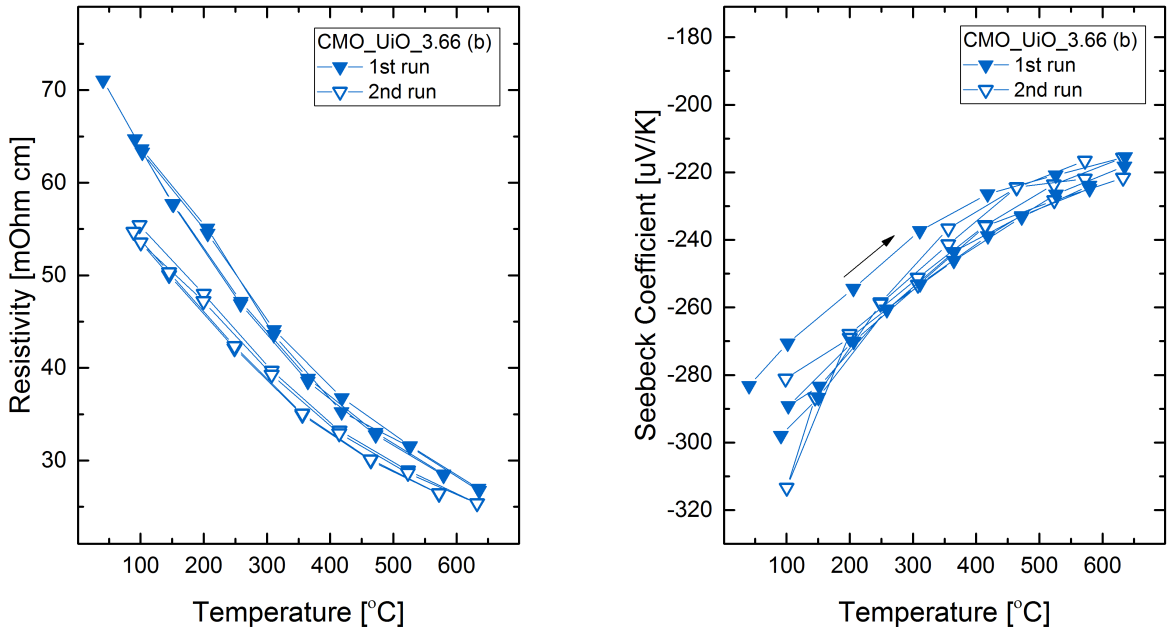

Figure 4.22: Resistivity (left) and Seebeck coefficient (right) for sample CMO_UiO_3.66 (b) for two different mountings, 1st and 2nd run

4.3.3 Dependency upon sample holders and the reproducibility of laser flash measurements.

The sample holders available for Netzsch LFA457 laser flash, are round with diameter 12.7 mm and square 10 mm and 8 mm. Disk shaped samples were prepared using a 13 mm die. However,

samples after sintering had a diameter of less than 12.7 mm, thus graphite support rings were utilized to prevent samples from falling through the sample holders. The dependency on support rings was tested by first measuring thermal diffusivity alternating the support rings used, figure (4.23) (left), and then by cutting the samples into squares and remeasure them using square sample holders, figure (4.23) (right). No reference samples were available for the square sample experiment and the raw data, thermal diffusivity, was instead compared directly.
When measuring the same samples with different support rings, the deviation in thermal diffusivity between the two runs are $\sim$0.05 $\mathrm{mm^2 s^{-1}}$ at low temperatures, decreasing to $\sim$0.01 $\mathrm{mm^2 s^{-1}}$ at higher temperatures, thereby considered negligible.

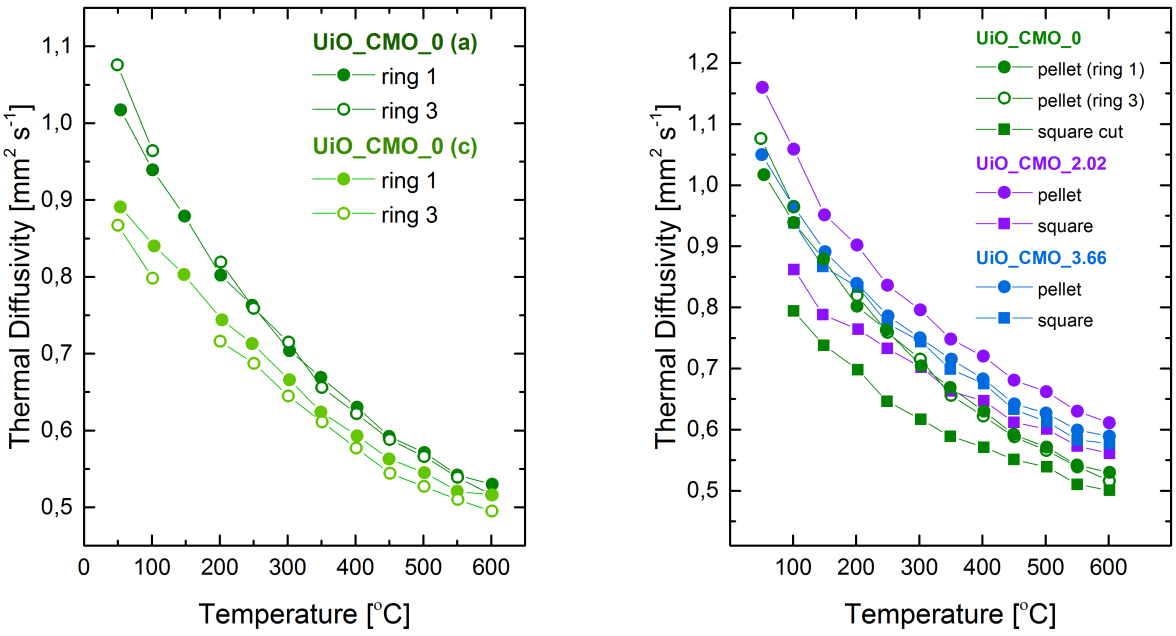

Figure 4.23: Thermal diffusivity of samples measured with different support rings (left) and compared to square cut samples (right).

When comparing thermal diffusivity measured on disk shaped samples and square cut samples, figure (4.23) (left), it is observed that for sample CMO_UiO_0 and CMO_UiO_2.02, the measured diffusivity in round holders are higher than for the square holders. For both samples the deviations are $\sim$0.3 $\mathrm{mm^2 s^{-1}}$ at low temperatures, decreasing to $\sim$0.05 $\mathrm{mm^2 s^{-1}}$ at higher temperatures. Sample CMO_UiO_3.66, on the other hand, only show small deviations in both holders. A reason for the shift only appearing for two out of three samples, might be the introduction of cracks in these two samples, while cutting them into squares. Crack

introduction would lead to a decrease in thermal diffusivity, which is observed in figure (4.23) (right). However, the deviations due to sample holders do not explain the spread in thermal conductivity as a function of Mn content, figure (4.19).
Netzsch has reported an uncertainty in the reproducibility of thermal diffusivity, for most materials, of $\pm 2\,\%$ and for specific heat capacity $\pm 3\,\%$ [92]. Additional claims in literature states that the uncertainty in the measurement, in addition to the conversion from diffusivity into conductivity through a reference sample, reaches as much as $20\,\%$ [47]. Several assumptions are made when conducting this experiment i) the thermal expansion of the material is 0, ii) the material does not undergo any phase transitions, iii) the specific heat capacity could be adequately described through a reference sample and iv) no heat was transported through convection on the sides of the samples due to inaccurate sample positioning in the holders. These assumptions might not be met and would benefit further investigations. Also, the importance of the graphite coating is emphasized in the review article by Borup *et al.*, claiming that even though it enhances absorption of the laser pulse and maximizes the detector signal, the thickness of the coating and the adhesion to the sample, might be a source of significant error [93]. This was assumed negligible in this work, but would be beneficial to investigate, and optimize, if further investigation into the reproducibility of thermal diffusivity measurements were to be performed.

Chapter 5

Discussion

In this chapter the results of structural characterization and thermoelectric properties presented in the previous chapter are discussed. A model for phonon scattering mechanisms, the Callaway model, is suggested and compared to the measured thermal conductivities. Lastly, the thermoelectric properties of samples received through collaborations at NTNU is presented and compared with the thermoelectric properties of UiO synthesised samples.

5.1 Influence of Mn excess on structure and morphology

All samples with Mn excess show the presence of two phases, $CaMnO_3$ matrix and secondary phase precipitates of $CaMn_2O_4$, mainly located on grain boundaries and in triple points. These results were presented in figure (4.4). The diameter of the $CaMn_2O_3$ particles was found to be in the range of $\sim$ 0.1 - 2 μm and increasing in number rather then extent with increasing Mn content.

Image analysis was performed on SEM micrographs to evaluate concentration of secondary phase and porosity, and to determine the average grain size of main and secondary phase. The approach is presented in Appendix L and the obtained result of the analysis in table (5.1) and figure (5.1).

Figure (5.1) (right) show the relative densities found through image analysis and are compared with the relative density obtained by the Archimedes and geometric method. Uncertainties associated with the Archimedes method are regarded as small, while larger uncertainties are associated with image analysis and geometric method. However, when disregarding the outlier sample, y = 0.10, there seem to be a relative decent agreement between the measured densities from the three methods. Relative densities appears to increase with increasing sintering temperature and increasing Mn concentration. The latter indicate that the secondary phase contribute to denser samples, possibly due to being located at grain boundaries and tripe points.

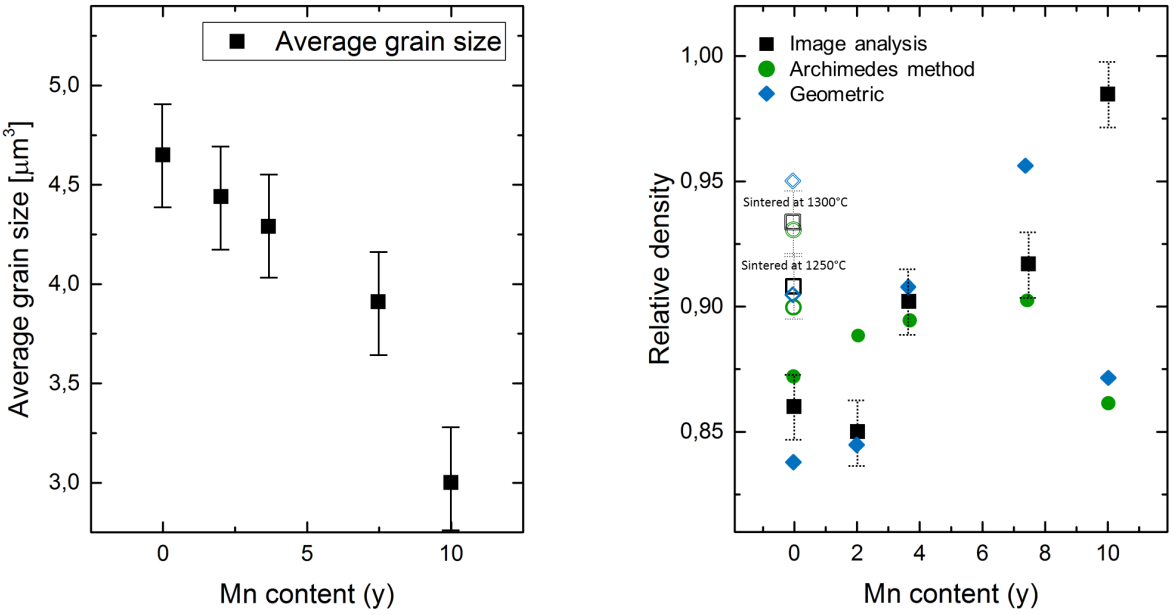

Figure 5.1: Average grain size (left) of grains in the $CaMnO_3$ matrix, and relative density (right) as a function of Mn concentration. Filled symbols represent samples with similar sintering program, 1200 °C for 20 h.

Average grain size was observed to increase with increasing sintering temperature, from $\sim$ 4.6 µm for 1200 °C, $\sim$ 7.7 µm for 1250 °C, to $\sim$ 12.0 µm for 1300 °C, with same dwell time. While average grain size appears to decrease with Mn concentration. The latter might be due to the secondary phase precipitates located on grain boundaries, which, with increasing Mn concentration, do not increase in volume but as a larger number of precipitates in the same size range, thus limiting the grain growth.

The estimated Mn composition from image analysis is presented in table (5.1), together with the intended nominal composition. The evaluation confirms that the sample series has increasing Mn concentration, thus justifying the investigation of thermoelectric properties as a function of Mn concentration. The image analysis yield a systematic evaluation of Mn content, lower than the intended nominal composition. This might indicate that there is a solubility of Mn in the $CaMnO_3$ matrix. However, during synthesis, it was observed that the precursor powder MnO_2 was easily adhesive to equipment like spatulas and beakers. Despite care was taken to not loose any powder, this might be the cause of some, though minor, Mn-deficiency. On the other hand, image analysis is a coarse method, with rough assumptions such as spherical grains, cut at random heights. Relatively large errors are associated with the evaluation, here assumed to be $\sim$10 %, however, the analysis is still useful to get an indication of trends.

Sample	Nominal composition y in [at%]	Secondary phase [area%]	Calculated composition y in [at%]
CMO_UiO_0(a)	0	0.3	0.2
CMO_UiO_2.02(a)	2.02	2.8	1.9
CMO_UiO_3.66(b)	3.66	4.9	3.3
CMO_UiO_7.47(a)	7.47	8.3	5.5
CMO_UiO_10(b)	10	10.7	7.0
CMO_NTNU_3.66	3.66	2.14	1.5
CMO_NTNU_7.47	7.47	6.79	4.5
CMO_UiO_0(a)	0	0.3	0.2
CMO_UiO_0(b)	0	0.3	0.2
CMO_UiO_0(c)	0	0.1	0.1

Table 5.1: Summary of nominal and calculated composition of a selection of samples $CaMn_{1+y}O_{3-\delta}$.

If there were some solubility of Mn (or Ca) in the main phase at higher temperature, illustrated in figure (5.2) with dashed lines, these might "freeze in" in the main phase upon cooling, and precipitates as entities on the nano-scale. Two scenarios are illustrated in figure (5.2). Line 1 correlates to a scenario where all hypothetical solute is stuck within the main phase, thus precipitating with equal distributions upon cooling. In scenario 2, line 2, some solute are under conditions which allow them to diffuse out of the $CaMnO_3$ matrix, and precipitate as the thermodynamically favourable $CaMn_2O_4$ phase. If these precipitates existed, they would be expected to be observable by TEM. However, such features has not been observed in calcined, sintered or measured samples. Under thermoelectric measurements, samples are cycled up and down to temperatures where ions are significantly more mobile, and would be expected to show a change in nano-structure. Since nano-precipitates have not been observed it might imply that there is no solubility in $CaMnO_3$ even at higher temperatures. Precipitates at this length scale would not necessarily be detected by SEM but might explain the deviation from a 1:1 relationship between Mn:Ca observed in the matrix, generally ~ 0.98 corresponding to a Mn deficient matrix, by EDS and WDS. The general trend from EDS is a slightly Mn deficient matrix, with an average Mn/Ca ratio of 0.97. This might indicate that all Mn excess precipitate as secondary phase $CaMn_2O_4$ and no Mn rich precipitates exist within the main phase. However, the general trend in brighter area secondary phase is a Mn/Ca ratio of 1.5 corresponding to a 2:3 relation between Ca and Mn. This is a significant deviation from the expected 2 ratio or 1:2 relation frp, XRD analysis, showing only two phases present, $CaMnO_3$ and $CaMn_2O_4$.

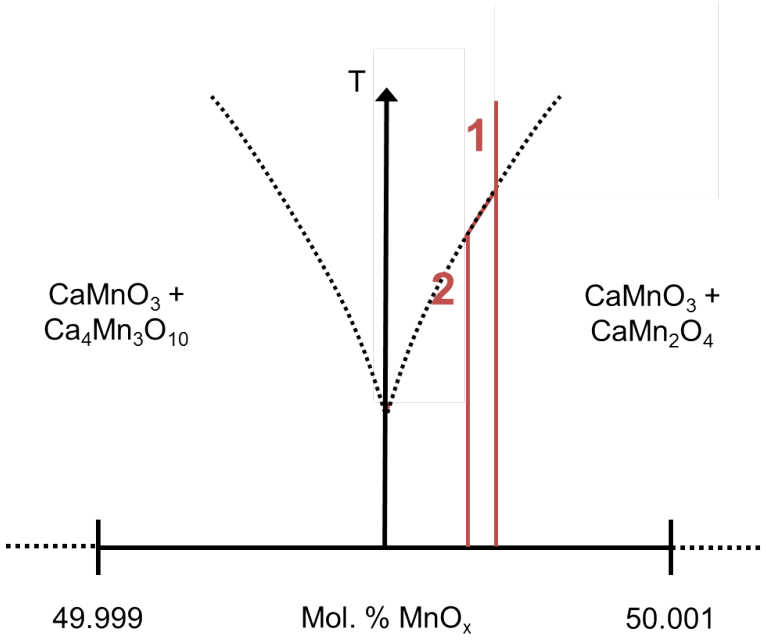

Figure 5.2: Illustration of hypothetical solubility in $CaMnO_3$ and two scenarios yielding different concentration of precipitates.

A 2:3 relation is corresponding to $Ca_2Mn_3\ O_8$ phase, structural data presented in Appendix D, with space group C12/m1 (12) and cell parameters a = 1.102, b = 0.5848, c = 0.4942 nm [94]. However, this does not correlate with the obtained XRD data, figure (4.2). When moving from matrix to the bright precipitates, the at% of oxygen decrease rather then increase relative to the matrix supporting that the secondary phase is not $Ca_2Mn_3\ O_8$, with at% O of 0.62 compared to $CaMnO_3$ with at% 0.60 and $CaMn_2O_4$ with at% O of 0.57. A reason for the low Mn/Ca ratio might be due to high concentrations of Mn vacancies, substitution of Ca on Mn sites, or a high solubility of Ca interstitials in the $CaMn_2O_3$ phase. However, high concentrations of these defects would be detectable by XRD due to the change in cell parameters, which has not been observed. Another possible reason for unexpected Mn/Ca ratio might be due to the interaction volume of the electron probe. By probing underlying main phase $CaMnO_3$ in addition to the bright area precipitate, the average Mn concentration will be lower than representative for the precipitate. However, all analysis of bright are precipitates show close to 1.5 Mn/Ca ratio. The focus of this work has been on nano-precipitates within the $CaMnO_3$ matrix, and the nano-structure of the secondary phase precipitates has not been investigated. This should be included if further work is conducted.

Nano-structural investigation by TEM shows a general trend of perfect crystallinity within the $CaMnO_3$ matrix, and no distribution of precipitates or defects. Examples of these findings were presented in figure (4.12). This implies that the excess Mn does not manifest as

nano-precipitates within the $CaMnO_3$ matrix, but exclusively as secondary phase precipitates, $CaMn_2O_4$, providing further evidence that Mn solubility in the perovskite $CaMnO_3$ is limited.

5.2 Influence of Mn excess on thermoelectric properties

The electrical resistivity of the UiO synthesised samples are in the range of 20 - 100 mOhm cm from room temperature to 600 °C in good agreement with literature [32, 38]. The decrease in resistivity with temperature is likely due to increased mobility and, to a less degree, thermally excited charge carriers. Calculated activation energy was found to be $\sim\sim$0.06 eV at lower and $\sim\sim$0.14 eV at higher temperature, similar for all compositions. The activation energy indicates small polaron hopping conduction [38,95]. Donor doped $CaMnO_3$ is reported to have an decrease in resistivity with dopant concentration, to as low as 10 mOhm cm with 0.02 at% W on B site [32] and $\sim$15 mOhm cm for 0.01 at% Ta on B site [34] at 300 K. Which is significantly lower for the, nominally undoped, samples investigated in this project with a resistivity of $\sim$90 mOhm at 300 K.

The Seebeck coefficient of the samples is negative, implying that the sample is an n-type semiconductor, and is in the range of -300 μVK^{-1} at room temperature to -200 μVK^{-1} at 600 °C, shown in figure (4.16). This in agreement with literature [32, 38]. The decrease in absolute Seebeck with temperature is likely due to thermally excited charge carriers, and is in agreement with the decrease of electric resistivity with temperatures. Small changes in concentrations of impurities would lead to a change in both resistivity and Seebeck coefficient. However, due to the Seebeck coefficient being so similar for all samples with Mn excess, this would imply small to insignificant impurity levels.

Even though no trend in Seebeck coefficient or resistivity due to Mn content is found, there is a spread in both measurements between samples with different Mn composition. The spread in Seebeck coefficient is of $\sim$ 10 % at the most. It is reported that the Seebeck coefficient of a seemingly homogeneous sample can have significant spatial variations, which can easily result in a measurement inaccuracy of 10 %. In addition, experimental considerations, like contact placing and measurement geometry can cause additional uncertainty [9, 96, 97]. The observed spread in Seebeck coefficient is thus regarded as small to none, and is possible due to measurement setup. Therefore, it is argued that the Seebeck coefficient does not vary significantly with the Mn content. This indicates no systematic change in carrier concentration between the samples. The observed spread in resistivity, of as much as $\sim$ 20 mOhm cm might thus be due to sample morphology such as porosity, grain size and possible micro cracks.

The thermal conductivity of the investigated samples is in the range of 3.6 W $m^{-1}K^{-1}$ at room temperature to 1.8 W $m^{-1}K^{-1}$ at 600 °C, decreasing with increasing temperature. These results were presented in figure (4.17). By analysing the thermal conductivity through Wiedemann Franz law it was shown, figure (4.18), that the electrical contribution is negligible. If there was a change in lattice thermal conductivity due to nano-precipitates by Mn content, it would not be masked by increasing contribution from the electronic contribution at higher temperatures, and should be observable. The thermal conductivity is heavily dependent upon sample morphology, and even though correction models for porosity and evaluation of grain size have been applied, no trend in thermal conductivity is observed as a function of Mn content. The spread in the measured values, ∼10 %, might be in the range of the error estimation of the measurement itself, discussed extensively in chapter (4.3). The lack of a trend in thermal conductivity with Mn content can be correlated with the the absence of nano-precipitates observed by micro- and nano-structural investigations. Hence, no additional scattering centres for long wavelength phonons exist, leaving the thermal conductivity unaffected by Mn stoichiometry.
A theoretical model for phonon relaxation times in $CaMnO_3$ was found by the Callaway model presented in section 2.6.5 with the script and assumptions presented in Appendix N. The calculated relaxation times for Umklapp, impurity, grain boundary and electron-phonon scattering are presented as a function of phonon frequency (left) and temperature (right) in figure (5.3). The calculations are done on a $CaMnO_3$ crystal with grain size 10 μm and impurity level 0.05 Ca vacancies chosen for illustrating purposes.

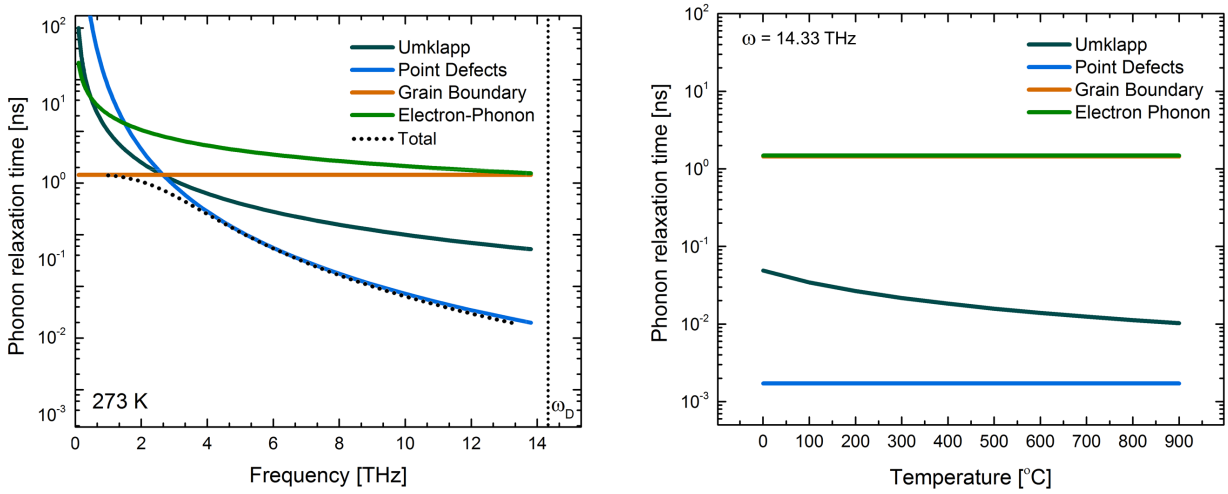

Figure 5.3: Calculated phonon relaxation time as a function of phonon frequency (left) and temperature (right) for Umklapp, point defect, grain boundary and electron-phonon scattering at 273 K. The crystal is modelled with a grain size of 10 μm and impurity level of (1-0.95).

Figure (5.3) (left) shows that as the phonon frequency increase the dominant scattering mechanism changes from grain boundary scattering for phonon frequencies below ∼3 THz to point defect scattering. The Umklapp and electron-phonon scattering contribute more with increasing frequency, however, is point defects remain the dominating factor in $CaMnO_3$ for all frequencies above ∼3 THz.

The approximated parameters, the Gruneisen parameter, $\gamma = 1$, deformation potential, $E_{def} = 2$eV, and electron effective mass, $m^* = 0.36\ m_0$, are all linear in the calculation of the Umklapp and electron-phonon scattering times, eq. (2.50) and (2.54). Even if the chosen values were based on several, partly crude assumptions, realistic deviations will not lead to a significant variation of the obtained phonon relaxation times, as neither Umklapp nor electron-phonon scattering is dominant at any frequency. The effect of impurity concentration (left) and grain size (right) on phonon relaxation times as a function of phonon frequency are presented in figure (5.4). By increasing the impurity concentration, from 0.05 to 0.20, figure (5.4) (left), the relaxation time of point defect scattering decrease and becomes even more prominent. It is reported in the literature, in analogy with the calculated trend, that alloying $CaMnO_3$ with heavier elements on A- and B-site does lower the thermal conductivity [32, 34, 98].
Alloying of $CaMnO_3$ with a donor species, also lead to an increase in charge carrier concentrations, thus a decrease in resistivity and the absolute Seebeck coefficient. However, it has been reported that by exceeding a certain substitution level, an increase in resistivity is observed [87, 98]. The effect is explained by the authors in [98] with the basis of charge ordering in heavily doped $CaMnO_3$.

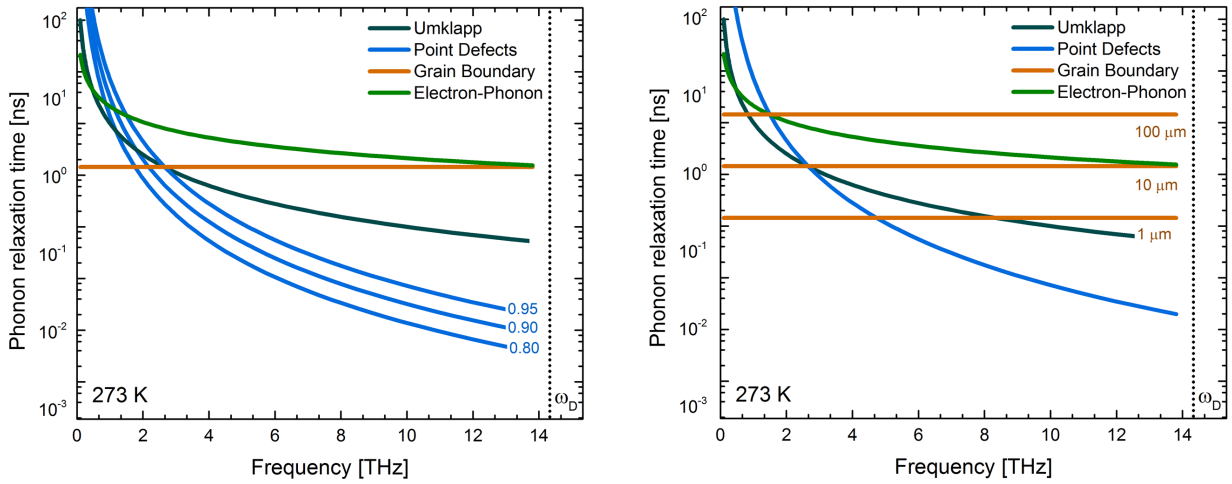

Figure 5.4: Calculated phonon relaxation time with phonon frequency for Umklapp, point defect, grain boundary and electron-phonon scattering processes at 273 K with constant grain size, 10 μm with varying impurity concentration (1-0.8, 1-0.90, 1-0.95) (left) and constant impurity level, (1-0.95), with varying grain size (right).

The alloying level needed to obtain the desired effect on thermal conductivity might exceed the concentration where the resistivity begin to increase. Therefore, $CaMnO_3$ should be substituted with a heavier element with same valence, lowering the thermal conductivity, accompanied by another element with dissimilar valence, decreasing resistivity, to maximise the effect of alloying on the thermoelectric properties. Unlike what is conducted in reference [32, 34, 98] discussed above. It must be noted that by increasing impurity concentration also the charge carrier concentration will increase, which would influence the electron-phonon scattering. However, this effect assumed to be low and hence disregarded in this work. However, this was not the focus of this project, but would be an interesting next step if further work was conducted.
By increasing the grain size, the relaxation time of boundary scattering increase, thus the scattering of grain boundary becomes insignificant for phonons with frequencies over 1.5 THz. With the presented crystal properties, a grain size of 1 μm and impurity level of 0.05, the electron-phonon scattering is the dominating scattering mechanism for phonons with frequency 1.5 - 2.5 THz, before point defect scattering dominated at higher frequencies. When decreasing the grain size to 1 μm, the relaxation time decrease and grain boundary scattering becomes the prominent scattering mechanism for phonons. Decreasing grain size is thus an effective way of reducing low frequency phonon propagation. The grain size in CMO_UiO samples is ∼5 μm while secondary phase precipitates, $CaMn_2O_3$, particle size is ∼5 μm. The secondary phase precipitates would contribute to scattering of low frequency phonons, of a value between the presented relaxation time for grain boundary scattering between ∼1-10 μm reported in figure (5.4) (right). However, the value must be weighted with respect to secondary phase concentration relative to main phase and main phase grain size. Thus the effect of the observed secondary phase, figure (4.4), on the reduction thermal conductivity is low and limited to low frequency phonons. This result thereby rationalizes the experimental findings in figure (4.17) on thermal conductivity.

Precipitates on the length scale of a couple of nm, which was the hope and aim of the project, resemble more a point defect than a small grain, when implemented in the Callaway model. However, the model gives an indication, by the decrease in relaxation time with small grains and high concentration of point defects, that precipitates of that length scale would contribute to a decrease in thermal conductivity.

5.3 Influence of synthesis method on structure and thermoelectric properties

Externally synthesised samples, by collaborators at NTNU, have been investigated and compared with samples synthesised at UiO. The main difference of the synthesis methods is that sintering was performed in reducing atmosphere at higher temperatures. The details of the synthesis methods are found in section 3.1.All samples has been investigated by SEM and image analysis in the same manner as for the CMO_UiO samples. SEM micrographs show equal distribution of secondary phase in the size range of $\sim$ 0.1 - 2 µm. By image analysis less than nominal compositions of Mn was found. Grain size evaluation showed larger grains and denser samples than samples synthesised at UiO. Even though samples are shown to be denser and have smaller grains with increasing Mn content, the CMO_NTNU sample with highest Mn excess is still denser and has larger grains than the CMO_UiO sample with least Mn excess. Samples were further investigated with TEM and, in agreement with CMO_UiO samples, no precipitates or systematic defects were found.

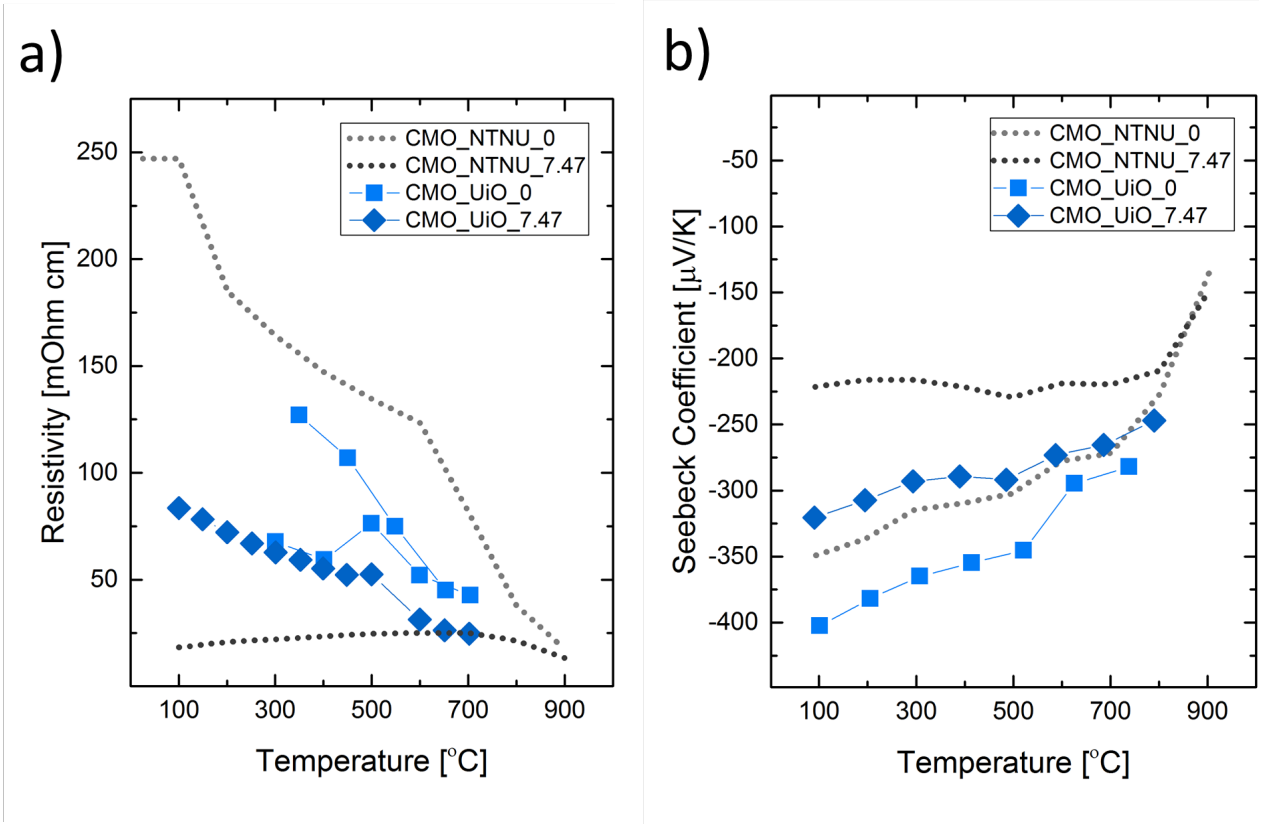

Figure 5.5: Comparison of electrical resistivity (left) and Seebeck coefficient (right) for samples $CaMn_{1+y}O_{3\pm\delta}$ with y = 0 and y = 0.074 synthesized at UiO and NTNU.

Thermoelectric properties of the samples were measured at NTNU, and compared with CMO_UiO samples in figure (5.5) and (5.6). However, with only two compositions one can not discuss a trend with Mn content.

Since the Seebeck coefficient is not dependent upon microstructure, one would expect the Seebeck coefficient of CMO_UiO and CMO_NTNU samples to be similar with same Mn composition. The CMO_NTNU samples show a lower absolute Seebeck coefficient, for both the stoichiometric sample and the sample with Mn excess. This indicates a higher charge carriers concentration than in the CMO_UiO samples, which might be due to precursor or other impurities. The resistivity of CMO_NTNU samples is expected to be lower than CMO_UiO samples due to the lower absolute Seebeck coefficient in combination with higher density and larger grain size which would lead to higher charge carrier mobility. This is the case for CMO_NTNU sample with Mn excess, but not the stoichiometric one. No apparent trends are observed, thus the reason for the high resistivity of the CMO_NTNU stoichiometric sample might be due to unobserved sample conditions, such as microcracks, which would influence the electrical resistivity but not the Seebeck coefficient.

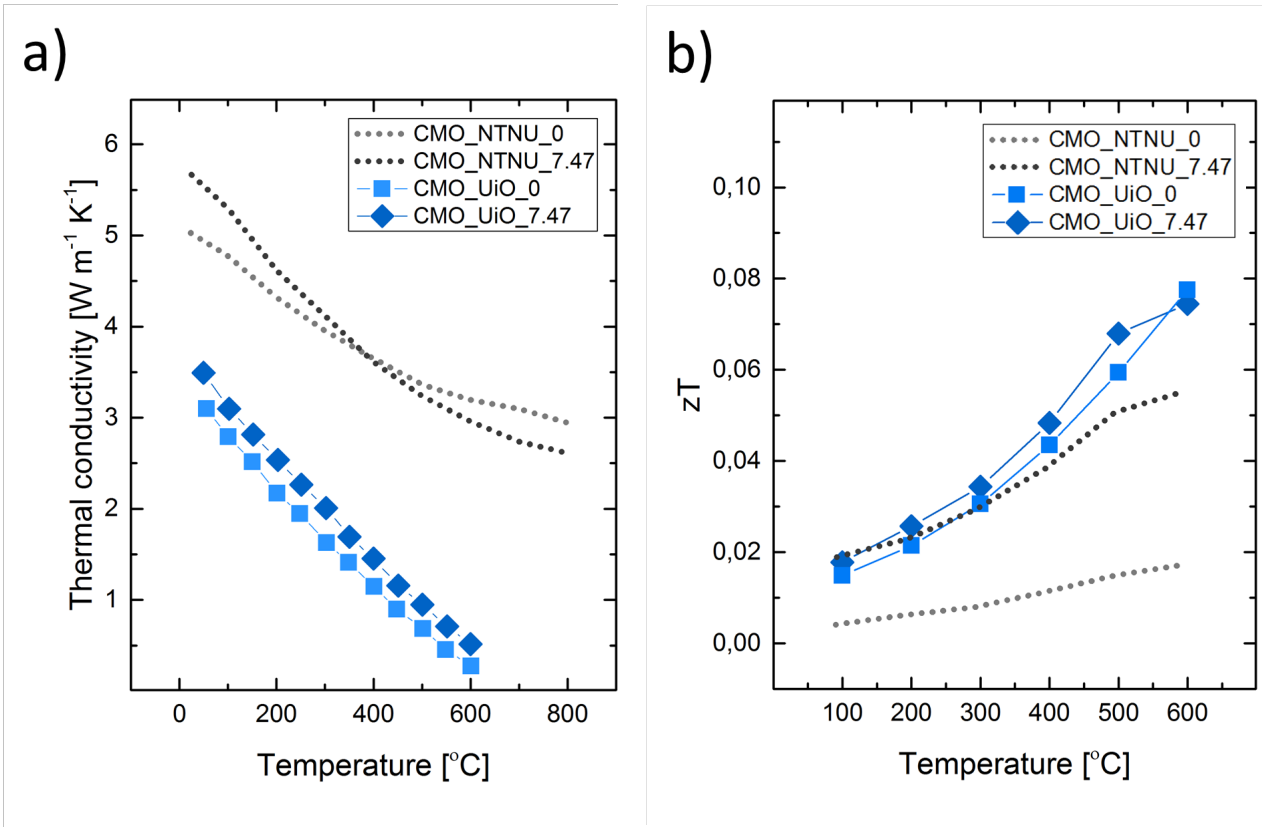

Figure 5.6: Comparison of thermal conductivity (left) and zT (right) for samples $CaMn_{1+y}O_{3\pm\delta}$ with y = 0 and y = 0.074 synthesized at UiO and NTNU.

The thermal conductivity of CMO_NTNU synthesised samples is presented in figure (5.6) (left), showing thermal conductivities in the range of 5 - 6 W $m^{-1}K^{-1}$ at room temperature decreasing to 3 - 3.5 W $m^{-1}K^{-1}$ at 600 °C. These values are significantly higher than for the CMO_UiO samples. This is likely due to the higher density and larger average grain sizes for all sample compositions. However, only the thermoelectric data of sample CMO_NTNU_0 was provided, hence the microstructure of this sample has not been investigated, thus no outright conclusions regarding this sample can be made.
Figure (5.6) (right) show calculated figure-of-merit, zT, values for CMO_NTNU and CMO_UiO samples. The CMO_UiO samples and the CMO_NTNU_7.47 sample show similar values of zT, increasing from ~ 0.02 at lower, to ~ 0.08 at higher temperatures. While the CMO_UiO synthesised samples do no not show a shift in zT from nominally stoichiometric sample to the sample with Mn excess, the zT values of the nominally stoichiometric CMO_NTNU samples is significantly lower than the one with Mn excess. Even though the CMO_NTNU samples has a significantly higher thermal conductivity, it appears the low resistivity of CMO_NTNU_7.47 compensate for that, leaving the over all thermoelectric properties comparable to the CMO_UiO samples.
It has been shown that a more complex synthesis technique does not enhance the thermoelectric properties of $CaMnO_3$. The sintering conditions, under reducing atmosphere, does not appear to facilitate nano-precipitates within the main phase, lowering the thermal conductivity. On the contrary the thermal conductivity of the CMO_NTNU samples are higher than for CMO_UiO, most likely due to larger crystal grains. However, the electrical resistivity of CMO_NTNTU_7.47 sample was measured to be lower than for all the CMO_UiO samples, which cannot de solely due to lager grains, and the suspicion of impurities has been presented. Based on the present investigations, there seem to be no effect of synthesis method on thermoelectric properties.

5.4 Further work

From this study several areas would benefit on further investigations to obtain a deeper understanding of the material and the effect of Mn non-stoichiometry.

- Thermogravimetric analysis with Differential Scanning Calorimetry (TGA-DSC) is encouraged to investigate possible structural changes causing the slope change in Seebeck coefficient, presented in figure (4.16). TGA-DSC will reveal possible change in entropy as a change of temperature, indicating a phase transition in the material. TGA-DSC would also be interesting to determined the heat capacity of the material to more accurately calculate the thermal conductivity. By applying the Landauer-EMT and Maxwell-Eucken correction models for

a two phased material, the thermal conductivity of $CaMn_{1+y}O_{3\pm\delta}$ can be determined with higher accuracy, which might reveal the actual contribution of the $CaMn_2O_4$ phase. Further investigation into the reproducibility of LFA measurements is also sought for, especially to investigate the influence of graphite spray and sample height.

- Electron Backscatterered Electron Diffraction (EBSD) would reveal possible orientation relations between crystal grains in the main phase and to the secondary phase. This would give a more accurate grain size and phase analysis, thus a more precise evaluation of sample morphology and possible influence on thermoelectric properties.
- Further TEM studies to determine the origin and nature of the deviating areas reported in this project would be beneficial to understand this material in more detail. HR-STEM on a monochromated TEM instrument would be a strong technique to characterise the local structure with high precision. Further including EELS experiments would allow the chemical environment of the deviating areas to be determined by measuring the change in the bonding environment. Environmental TEM studies should be included to investigate structural changes with temperatures, especially around the temperatures where the slope change in Seebeck coefficient is observed, and the transition temperature of the cubic to orthorhombic phase.

- $CaMnO_3$ ia an abundant and non-toxic promising candidate as a n-type thermoelectric material, applicable at high temperatures, and it is of further interest to investigate ways of improving its thermoelectric properties. From the analysis performed using the Callaway model, it is found that point defect scattering is the prominent scattering mechanism in $CaMnO_3$. It would therefore be interesting to substitute heavier elements, with same valence, on both A and B site and investigate the affect of electrical and thermal properties. Found most interesting by the author is substitution of Zr on Mn site while donor doping with Sc on Ca cite. Also interesting would be a mixed doping with a element with same valence and one aliovalent, both on B-site.
- Optimizing the synthesis method, providing better control of microstructure would need to be further investigation. Applying other methods such as, sol-gel method, templating or printing to decrease grain size would be of interest.
- An interesting experiment would be to flicker the temperature around the cubic to orthorhombic phase transition temperature, to investigate if this would leads to even smaller crystal grains with orientation relationships, and investigate the effect on electrical and thermal properties.

Chapter 6

Conclusions

In this master project, structural and thermoelectric studies of non-stoichiometric $CaMn_{1+y}O_{3\pm\delta}$ have been performed to investigate whether Mn non-stoichiometry facilitates the creation nano-precipitates within the $CaMnO_3$ matrix, acting as scattering agents for long-wavelength phonons.

The structural investigations of $CaMn_{1+y}O_{3\pm\delta}$ with Mn excess show precipitates of secondary phase, $CaMn_2O_4$ in the 5-10 μm range. These are observed to be too large to be effective scattering centres for phonons, thus do not contribute to lowering the thermal conductivity of the material. Further investigations with TEM show no precipitates within the main phase.

The microstructural characterizations were complemented with a full characterization of the thermoelectric properties of the investigated materials. The materials inhabit a electrical resistivity of 20 - 100 mOhm cm and Seebeck coefficient of -300 to -200 μVK^{-1} at temperatures from room temperature up to 600 °C. The thermal conductivity is found to be in the range 2.3 - 3.6 $Wm^{-1}K^{-1}$ in the same temperature range. No trend with Mn content is observed in the thermoelectric properties. An extensive investigation of possible experimental factors, like sample porosity, impurity level and measurement inaccuracy, was performed in order to confirm the absence of a dependency on Mn-content.

The thermoelectric properties of the sample series were further compared with samples synthesized my a more sophisticated synthesis route. It was shown that the electrical resistivity and absolute Seebeck coefficient is lower, however, the total thermal conductivity is higher, than UiO synthesised samples. This indicates that a more complex synthesis route is not necessarily beneficial.

These findings are rationalized based on the microstructural results, demonstrating the usefulness of the combined investigation of thermoelectric transport and nano-structure.

Appendix A

CaO - MnO phase diagram

The CaO - MnO phase diagram is presented on the next page. The compositions investigated in this project are between 42 - 60 % MnO yielding expected phases $CaMnO_3$ and $Ca_4Mn_3O_3$ for Mn deficient and $CaMnO_3$ and $CaMn_2O_3$ for samples with Mn excess.

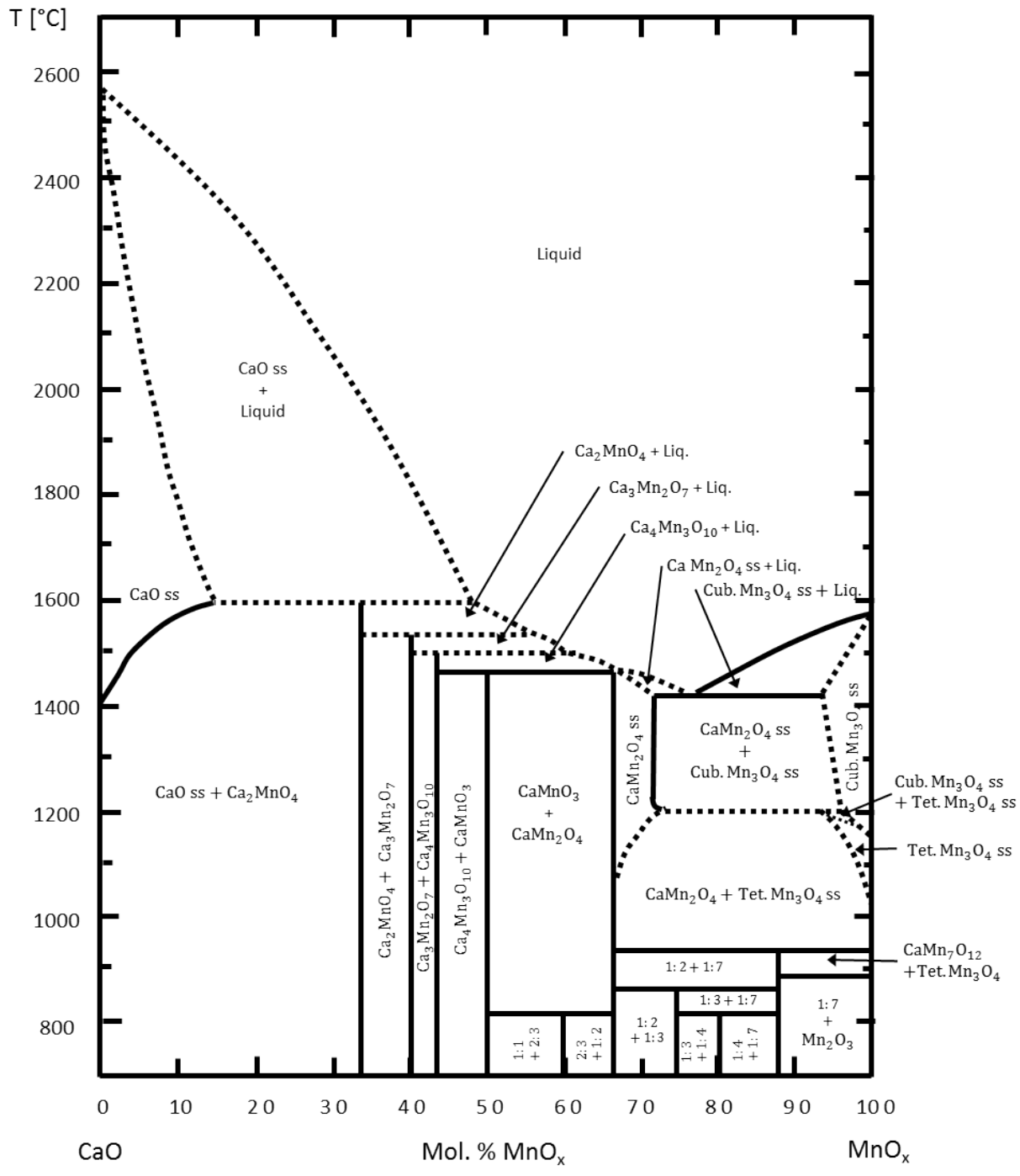

Figure A.1: The CaO - MnO phase diagram adapted from Horowitz and Longo [99].

Appendix B

Structure data of $CaMnO_3$

Crystal data for $CaMnO_3$ as obtained from [100].

Table B.1: Crystal data as obtained from [100]

Space group	Pnma (62)					
Cell parameters	a = 0.5265, b = 0.7452, c = 0.5282 nm, $\alpha = 90°$, $\beta = 90°$, $\gamma = 90°$					
Atom coordinates						
O1	O	8d	1	0.1988	0.0528	0.3044
Ca1	Ca	4c	.m.	0.43745	1/4	0.01537
O2	O	4c	.m.	0.5323	1/4	0.5996
Mn1	Mn	4a	-1	0	0	0
Reflection conditions						
0kl	k + l = 2n					
hk0	h = 2n					
h00	h = 2n					
0k0	k = 2n					
00l	l = 2n					

Appendix C

Structure data of $CaMn_2O_4$

Crystal data for $CaMn_2O_4$ as obtained from [100].

Table C.1: Crystal data as obtained from [100]

Space group	Pbcm (57)					
Cell parameters	a = 0.3155, b = 0.9988, c = 0.9677 nm, $\alpha = 90°$, $\beta = 90°$, $\gamma = 90°$					
Atom coordinates						
Mn1	Mn	8e	1	0.20400(7)	0.388233(19)	0.56852(2)
Ca1	Ca	4d	m	0.31754(11)	0.64882(4)	3/4
O1	O	4d	m	0.8095(5)	0.81633(14)	3/4
O2	O	8e	1	0.7994(3)	0.52716(9)	0.60794(10)
O3	O	4c	2	0.4077(5)	3/4	1/2
Reflection conditions						
0kl	k = 2n					
h0l	l = 2n					
hk0	h = 2n					
h00	h = 2n					
0k0	k = 2n					
00l	l = 2n					

Appendix D

Structure data of $Ca_2Mn_3O_8$

Crystal data and XRD for $Ca_2Mn_3O_8$ as obtained from [94, 100].

Table D.1: Crystal data as obtained from [94, 100]

Space group	C12 / m1 (12)					
Cell parameters	a = 1.102, b = 0.5848, c = 0.4942 nm, $\alpha = 90°$, $\beta = 109.8°$, $\gamma = 90°$					
Atom coordinates						
O1	O	8j	1	0.402	0.266	0.106
O2	O	4i	m	0.093	0	0.405
O3	O	4i	m	0.389	0	0.575
M1	0.600Mn + 0.400Ca	4i	m	0.73	0	0.162
M2	0.600Mn + 0.400Ca	4h	2	0	0.262	1/2
M3	0.600Mn + 0.400Ca	2a	2/m	0	0	0

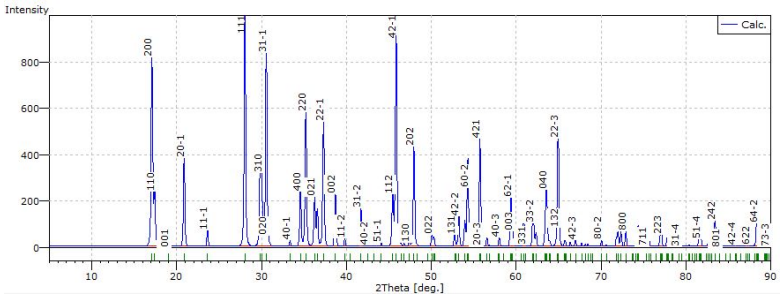

Figure D.1: XRD pattern obtained from [100] entry 1503483

Appendix E

Derivation of heat capacity

By including the interactions between adjacent atoms Debye described the energy as

$$U_D = 3\int_0^{\omega_D} d\omega D(\omega) u_n \tag{E.1}$$

where $D(\omega)$ is the density of states and u_n is the energy of a particular mode described as a harmonic oscillator

$$u_n = (\langle n \rangle + 1/2)\hbar\omega \tag{E.2}$$

where n is the phonon dispersion distribution from the Bose-Einstein distribution.

$$\langle n \rangle = \frac{1}{\exp(\hbar\omega_D/k_BT) - 1} \tag{E.3}$$

By solving the derivative of phonon dispersion with respect to temperature, where the zero point energy is neglected,

$$\frac{\delta\langle n \rangle}{\delta T} = \frac{\delta}{\delta T}\frac{1}{\exp(\hbar\omega_D/k_BT) - 1} \tag{E.4}$$

and inserting into equation (E), together with the expression for the density of states $D(\omega) = V\omega^2/2\pi^2V_s^3$, where V is the volume and v_s the speed of sound of the material, an expression for the Debye system energy is obtained as follows

$$U_D = \frac{3V\hbar}{2\pi^2 v_s^3}\int_0^{\omega_D} d\omega \frac{\omega^3}{\exp(\hbar\omega/k_BT - 1)}. \tag{E.5}$$

This reveals the Debye heat capacity

$$C_D = \frac{\delta}{\delta T}\frac{3V\hbar}{2\pi^2 v_s^3}\int_0^{\omega_D} d\omega \frac{\omega^3}{\exp(\hbar\omega/k_BT - 1)} \tag{E.6}$$

By doing the temperature dependent integration and substituting $x = \hbar\omega/k_B T$ in addition to introducing the *Debye temperature* $\theta_D = \hbar\omega_D/k_B$ the Debye approximation of the differential lattice specific heat is expressed as

$$C(x)dx = \frac{3k_B}{2\pi^2 v^3}\left(\frac{k_B}{\hbar}\right)^3 T^3 \frac{x^4 e^x}{(e^x - 1)^2} dx \tag{E.7}$$

Appendix F

Derivation of κ_L

By substituting equation (2.46) in to (2.47) the following expression for the total heat transported is obtained

$$\vec{Q} = -\frac{1}{3}\sum_{\vec{q}} \hbar\omega_{\vec{q}}\vec{v}_g^2\tau_q\frac{\delta N_{\vec{q}}^0}{\delta T}\vec{\nabla}T \tag{F.1}$$

yielding an expression for the lattice thermal conductivity

$$\kappa_L = \frac{\vec{Q}}{\vec{\nabla}T} = -\frac{1}{3}\sum_{\vec{q}} \hbar\omega_{\vec{q}}\vec{v}_g^2\tau_q\frac{\delta N_{\vec{q}}^0}{\delta T} \tag{F.2}$$

The summation is replaced by an integral where $f(q)d\vec{q} = (3q^2/2\pi^2)dq$ and following substitution $f(\omega)d\omega = (3\omega^2/2\pi^2v^3)d\omega$. And by the Debye assumption of average phonon velocity being approximately equal to the speed of sound in the solid, the phonon frequency is replaced for all phonon branches and assumed equal for all polarizations, $\omega_{\vec{q}} = v \cdot g$, yields together with equation (F.2)

$$\kappa_L = \frac{1}{2\pi^2 v}\int_0^{\omega_D} \hbar\omega^3\tau_q(\omega)\frac{(\hbar\omega/k_BT^2)\exp(\hbar\omega/k_BT)}{[\exp(\hbar\omega/k_BT)-1]^2} \tag{F.3}$$

where ω_D is the Debye frequency so that the total number of distinguishable phonon modes are described as $3N = \int_0^{\omega_D} f(\omega)d\omega$. By substituting $x = \hbar\omega/k_BT$ and defining the Debye temperature $\theta_D = \hbar\omega_D/k_B$ equation (F.3) become

$$\kappa_L = \frac{k_B}{2\pi^2 v}\Big(\frac{k_B}{\hbar}\Big)^3 T^3\int_0^{\theta_D/T} \tau_q(x)\frac{x^4e^x}{(e^x-1)^2}dx \tag{F.4}$$

The Debye approximation of the differential lattice specific heat is

$$C(x)dx = \frac{3k_B}{2\pi^2 v^3}\Big(\frac{k_B}{\hbar}\Big)^3 T^3\frac{x^4e^x}{(e^x-1)^2}dx \tag{F.5}$$

which when applied to equation (F.4) together with the expression for the mean free path of the phonon $l(x) = v\tau(x)$ yields the expression for the lattice thermal conductivity

$$\kappa_L = \frac{1}{3}\int_0^{\theta_D/T} C(x)vl(x)dx \tag{F.6}$$

Appendix G

XRD of CMO_NTNU

Figure (G.1) show XRD diffractograms NTNU synthesised samples with light blue line corresponds to CMO_NTNU_3.66 and dark blue line to CMO_NTNU_7.47.

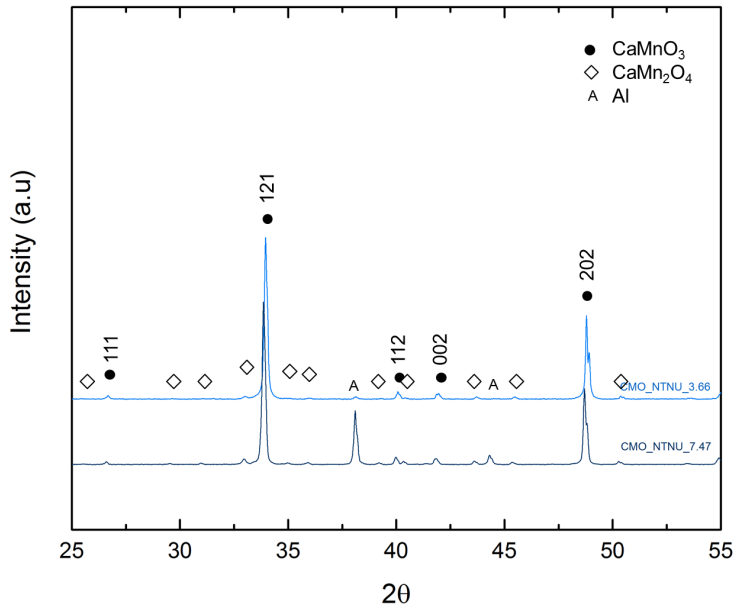

Figure G.1: XRD for CMO_NTNU. Indexed reflection correspond to • $CaMnO_3$, while ♢ $CaMn_2O_4$ and A Al (sample holder).

Appendix H

Simulated SADP, $CaMnO_3$

Simulated diffraction patterns for $CaMnO_3$ along [100], [101], [111] and [210] zone axis.

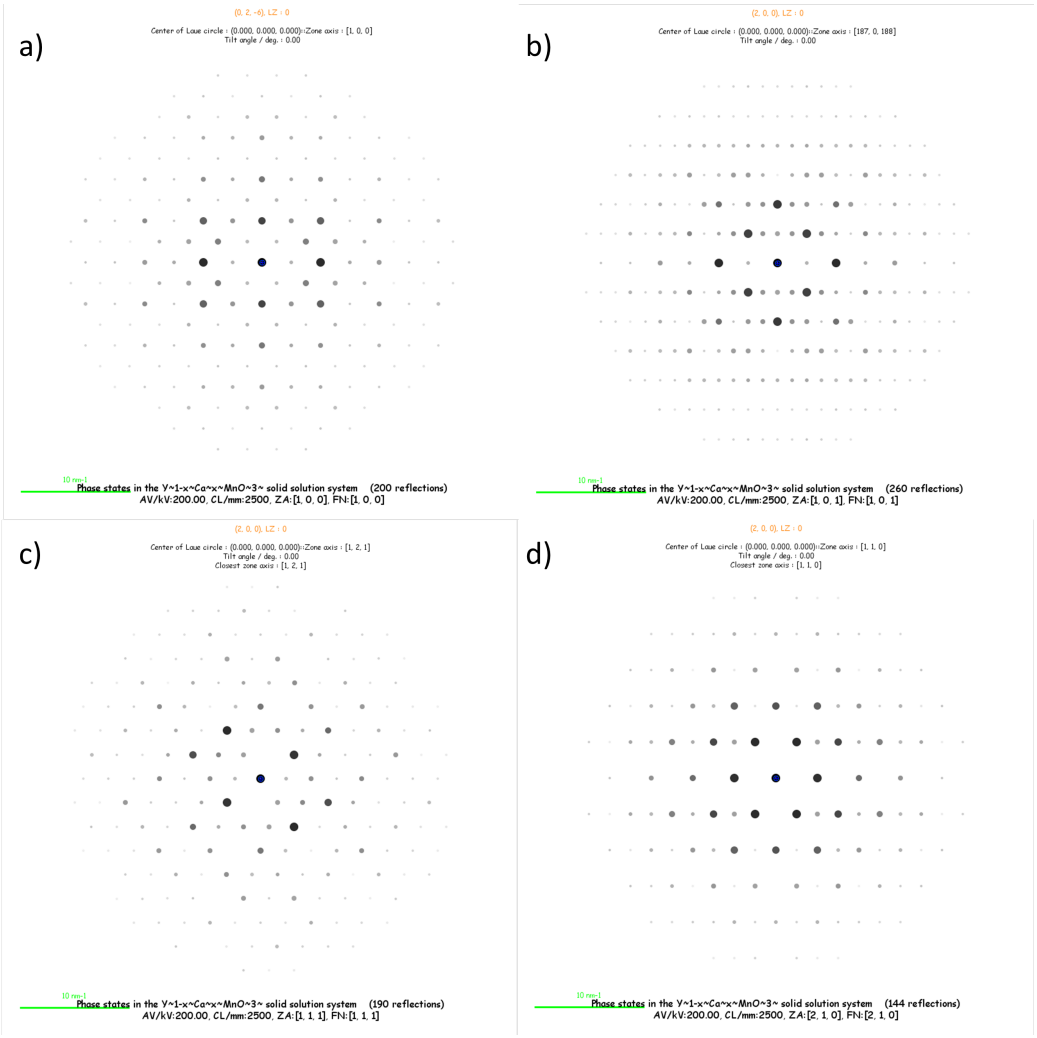

Figure H.1: Simulated DP of $CaMnO_3$ with zone axis a) [100], b) [101], c) [111] and d) [210]

Appendix I

Surface reactions

Surface features observed on sample CMO_UiO _3.66 (a) was investigated by collaborations at Wroclaw Research Centre EIT+, by Sandeep Gorantla and Anna Siemiatkowska, on FEI Helios NanoLab H50HP SEM/FIB and FEI Titan 60-300 cubed (S)TEM, operated at 300 kV. The microscope is equipped with an X-FEG gun, Wien-filter monochromator, image Cs-corrector, DCOR probe Cs corrector and ChemiSTEM super-X EDS detectors. High resolution STEM was obtained by HAADF imaging with a probe current of $\sim 80\,\mathrm{pA}$ and convergence and collection angle of 24.6 and 79.5 - 200 mrad, respectively. Rosette like features were observed on the surface of sample CMO_UiO _3.66 (a) with the SEM/FIB instrument, figure (I.1), and a FIB sample from the area was prepared and investigated with (S)TEM, figure (I.3).

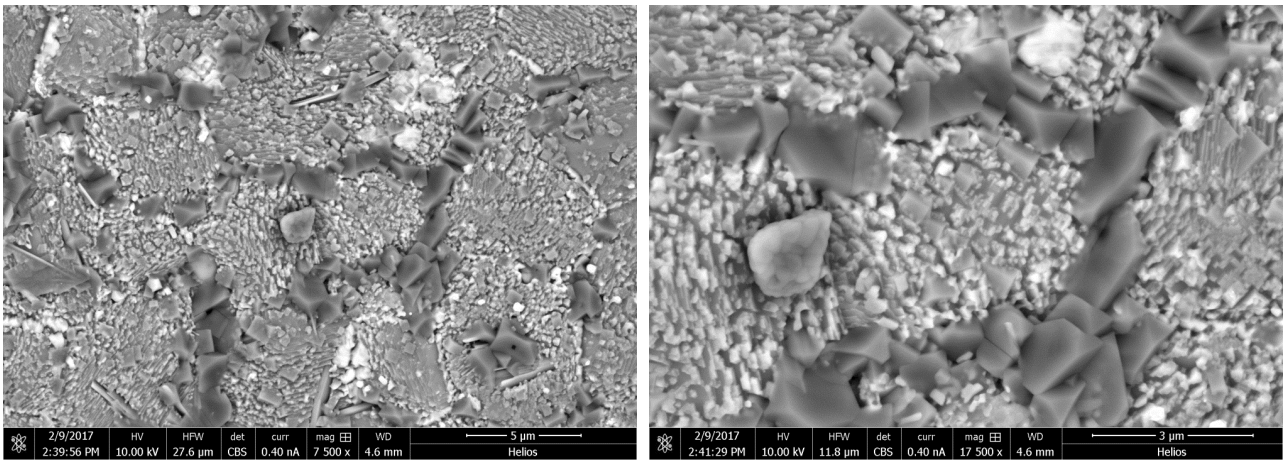

Figure I.1: Image of CMO_UiO_7.47(a) surface with a) 7500 times and b) 17500 times magnification.

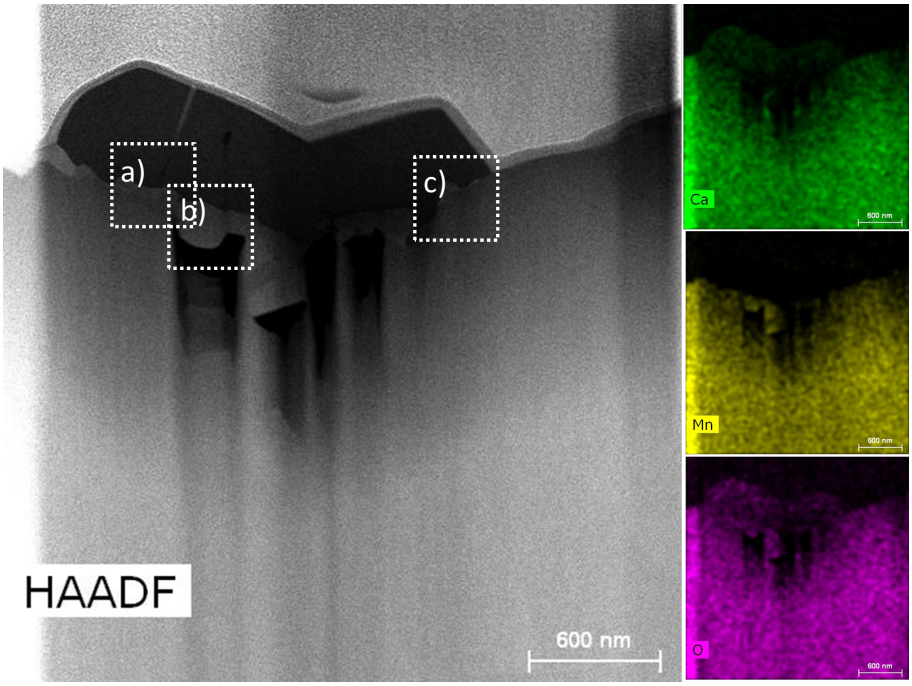

Figure I.2: HAADF image (left) and EDS (left) of FIB sample showing areas enriched in Ca and other enriched in Mn. Marked areas are further investigated in figure (I.4).

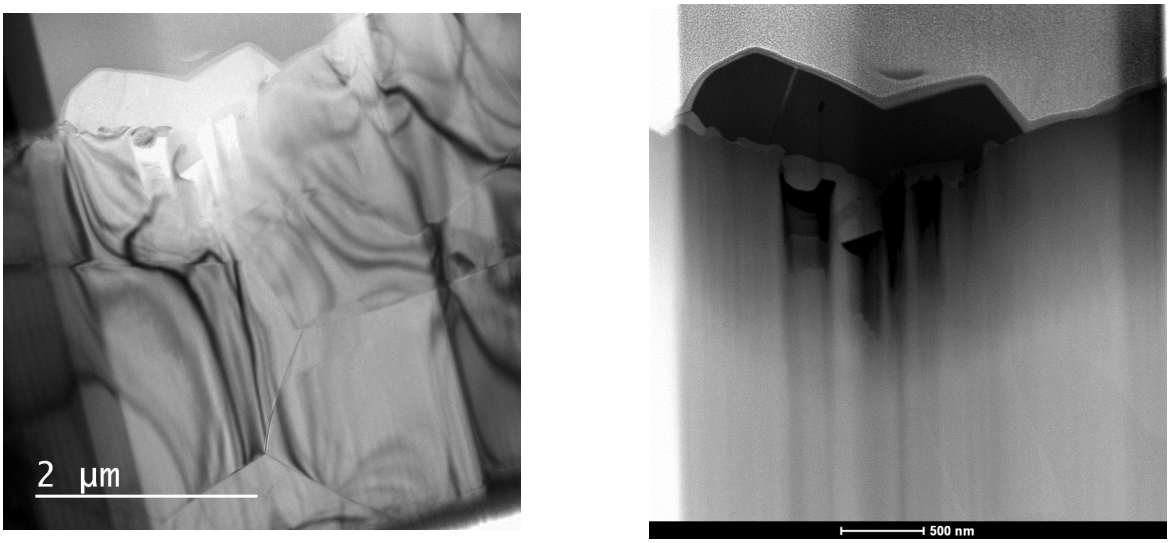

Figure I.3: BF-TEM image (left) and STEM-HAADF image (right) of FIB sample CMO_UiO_7.47 (a) showing one of the "rosettes" observed in SEM.

Figure (I.3) show BF-TEM (left) and HAADF (left) of the FIB sample. An overview of the EDS analysis is presented in figure (I.2) and (I.4) where the marked area in figure (I.2) correspond to EDS analysis presented in figure (I.4). The analysis show areas enriched in Ca and other enriched in Mn. The areas are crystalline, an example is presented in figure (I.5)

showing HRTEM image of interface from area c) presented in figure (I.2). Further investigations of these phases and the origin is needed before any conclusions can be made.

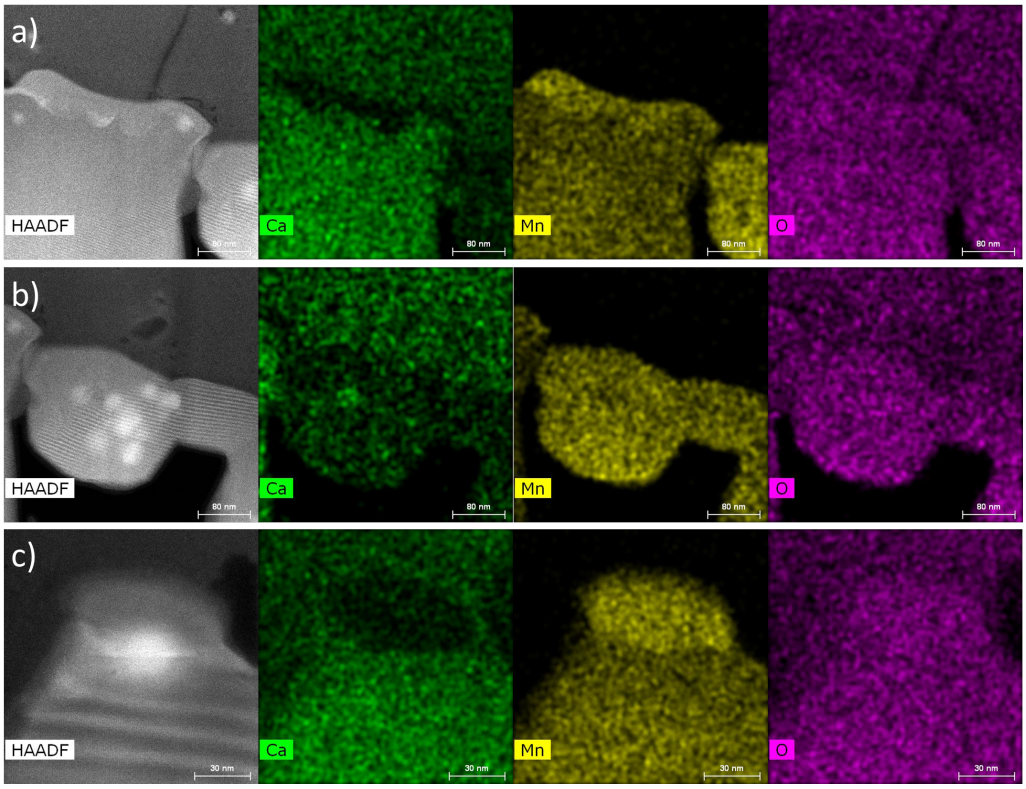

Figure I.4: EDS analysis of areas marked in figure (I.2).

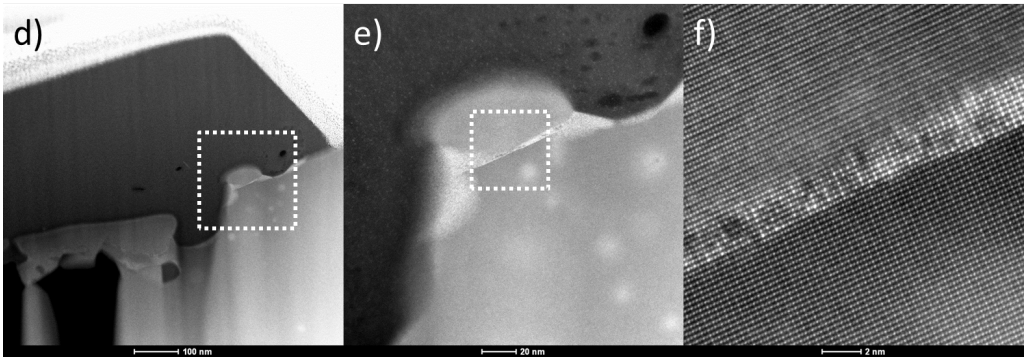

Figure I.5: HRTEM image of area c) in figure figure (I.2).

Appendix J

XRD of CMO_UiO_3.66

One selected sample, CMO_UiO_3.66, was investigated with XRD throughout the process, figure (J.1), to see if there was any phase change in the sample in any stages of the synthesis or measurement of sample.

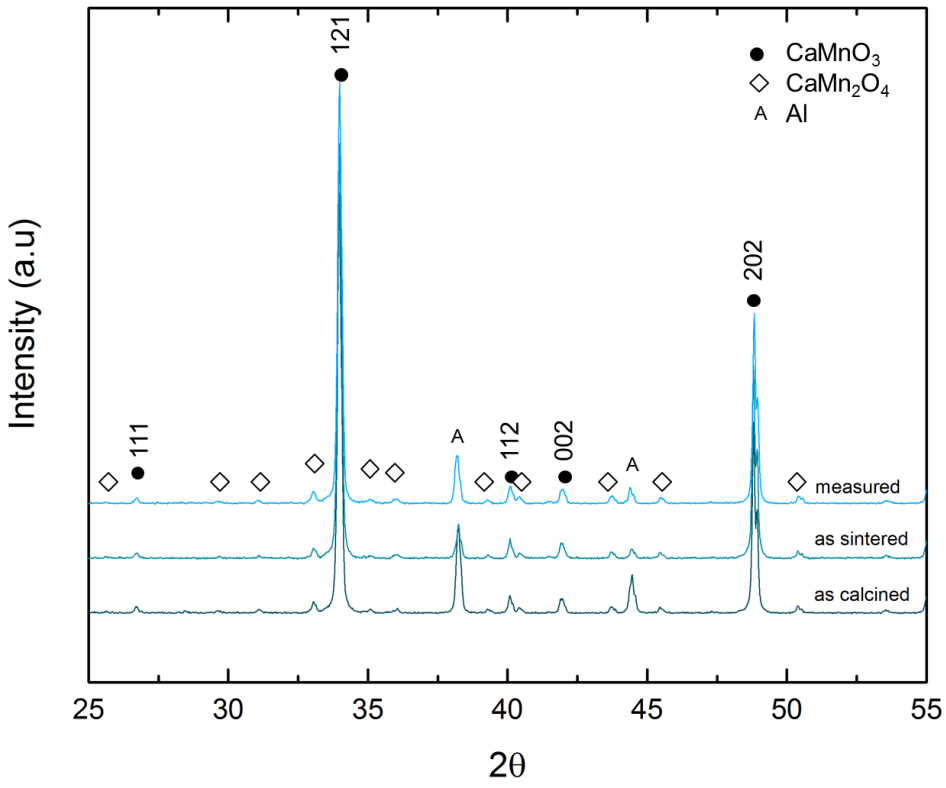

Figure J.1: Phase analysis of sample CMO_UiO_3.66 after calcination, after sintering and after thermoelectric measurements, showing no phase change.

Appendix K

Further TEM studies

Divinations from perfect crystallinity are attempted characterized by several methods. Figure (K.1) show areas where the atomic rows appear weaved or twisted. Marked area is masked and presented in figure (K.1) b) while figure (K.1) c) show extra half atomic planes marked with red arrows from masking of only the (100) reflection. FFT analysis of the undistorted and marked area, figure (K.1) d) and e) respectively, show extra reflexes along the (00 $\bar{1}$) direction corresponding to four times the atomic plane distance of the undistorted lattice. The planar distance is too large for the expected secondary phase $CaMn_2O_4$. It is also larger than that of the near-lying and suspected Ruddlesden Popper phases. This might indicate a superstructure or planar defects such as stacking faults. Sayers et al. reported stacking faults, in a similar system, of one atomic step in several layers showing contrast shifts comparable to those in figure (K.1) allowing speculation of similar faults [101]. The linear defects in figure (K.1) c) might also support an argument of pinned dislocations. Geometric phase analysis (GPA) show strain in the crystal also supporting the speculation of defects.

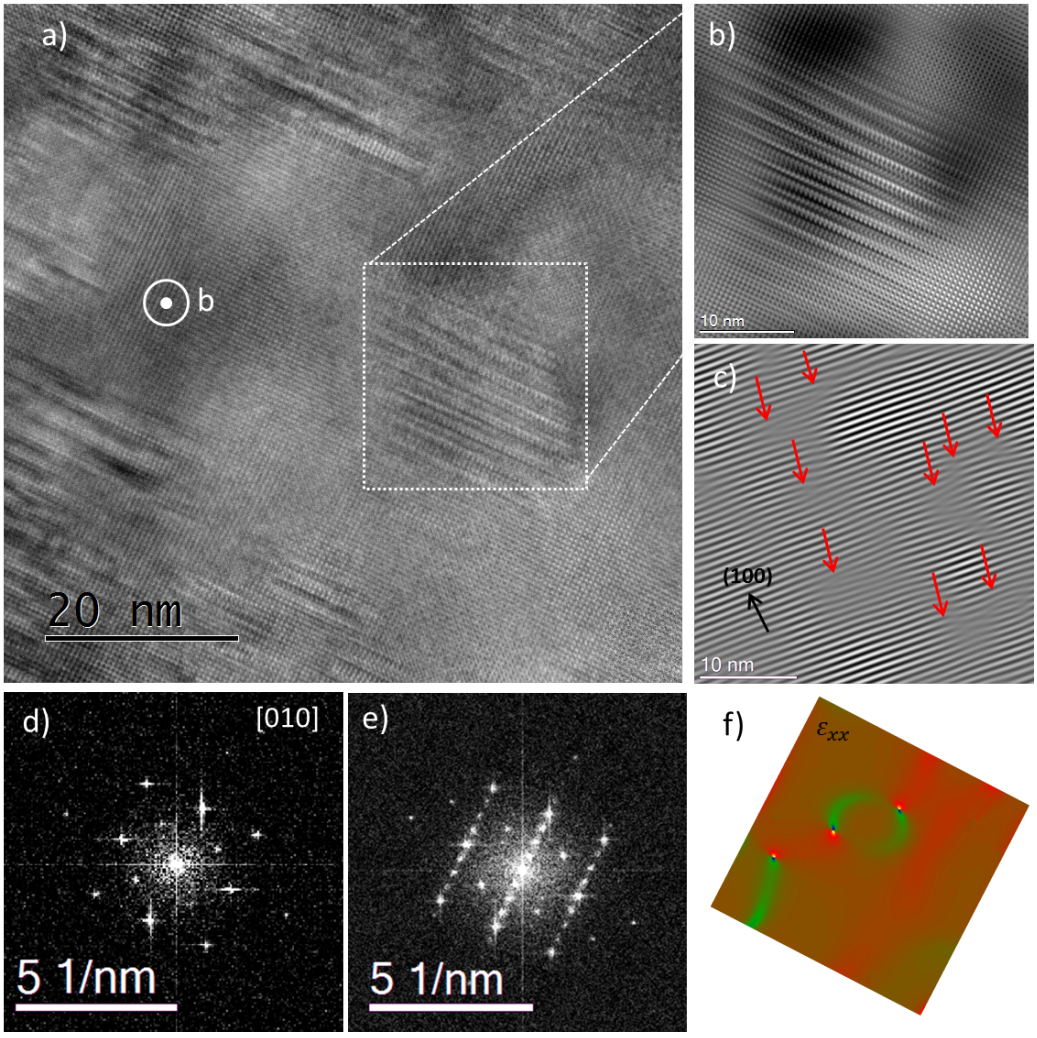

Figure K.1: a) HRTEM image of $CaMnO_3$ along [010] zone axis, b) masked and inverse FFT of marked area in a), c) masked (100) reflection showing extra half planes from d) corresponding FFT from undistorted and e) distorted areas in a) and f) GPA analysis of marked area in a)

Other distorted areas suspected of being stacking faults are shown in figure (K.2) and figure (K.3) by HRTEM images with corresponding FFTs. Even though seemingly similar to those in figure (K.1), the areas are significantly larger. The FFT show additional reflexes when moving across the boundaries. The distance between the extra reflexes, originating from the areas which are distorted, are the same for the areas in figure (K.1) and (K.2) and has not been found, as mentioned, to correlate with known phases expected from the phase diagram. From HRTEM image and corresponding FFTs in figure (K.2), a structural relation on the two sides of the weaved area is found. The top side has $\vec{b}$ oriented in the plane, along an atomic row, while the bottom side has a $\vec{b}$ oriented out of the image plane. A relation is also observed in figure (K.3) where HRTEM image a) and corresponding FFTs b) and d) show what appears to be a

twin grain boundary. The GPA analysis performed c) and e) show analysed strain. Further investigation of these areas are needed. Figure (K.4) and (K.5) show examples of other linear

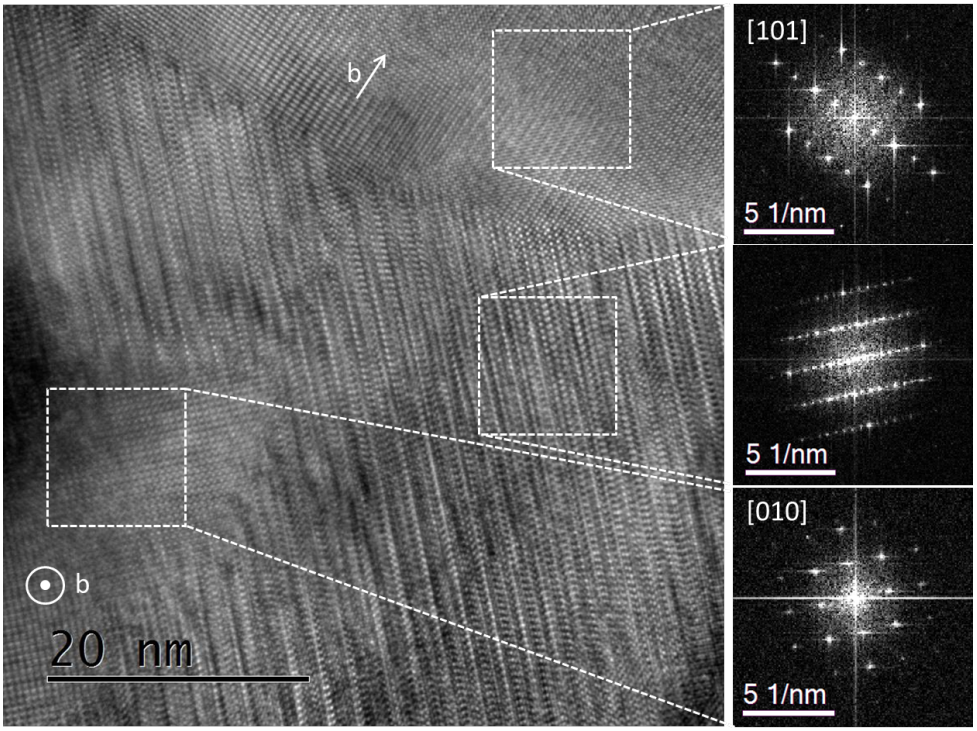

Figure K.2: HRTEM image of $CaMnO_3$ with corresponding FFTs from the three different phases.

defects found within the main phase. Figure (K.4) show HRTEM image from [012] zone axis, with corresponding FFT. Streaking observed in the FFT is marked with an arrow. On the left and right hand side are magnifications of the marked areas in the image, showing an area with no variation (left) and variation (right) of contrast. The contrast change in the right hand enlarged images are suspected of being due to stacking faults. HRTEM images with corresponding FFTs presented in figure (K.5) show an additional, and larger, area suspected of being stacking faults. These areas need further investigation before concluding. However this is beyond the scope of this work and will be included in potential further work.

TEM EDS spot analysis and STEM EDS has been preformed on the features in figure (K.1), (K.2), and (K.3) samples. TEM spot analysis show close to 1:1 ratio but were not able to resolve the changes in the Mn content from the main phase to the distorted areas. When preforming STEM EDS on the particle as a whole a gradient change in intensity is observed. This is most likely due to thickness variations. HR-STEM and EFTEM were attempted, but due to microscope limitations, high quality high resolution images were not obtainable on these samples. When finding a distorted area by HRTEM, STEM EDS were attempted on the area of interest. However, little intensity with reasonable counting times were detected, and the

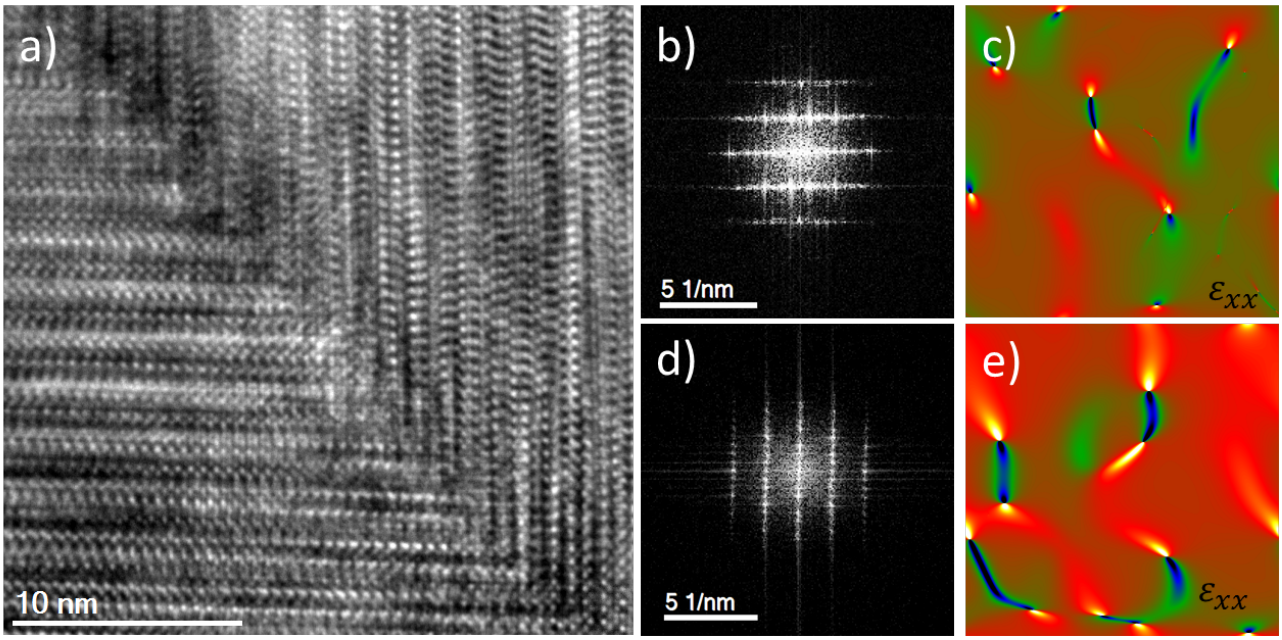

Figure K.3: a) A possible grain boundary of two unknown weaved areas, with corresponding FFTs and GPA analysis where b) and c) are from top/right area and d) and e) from bottom/left area.

technique was not pursued further. This might be a technique to try on a monochromated microscope if the project were to continue. STEM EELS was further attempted at the end of the project, showing a change in Mn edge, and would be reasonable next step to characterize these distorted areas. However, due to the topic being a sidetrack to the project and with the time limitation of the project further training in the technique was excluded. During investigations of FIB samples, no distorted area was observed. This might indicate that defects might have been introduced when preparing powder samples.

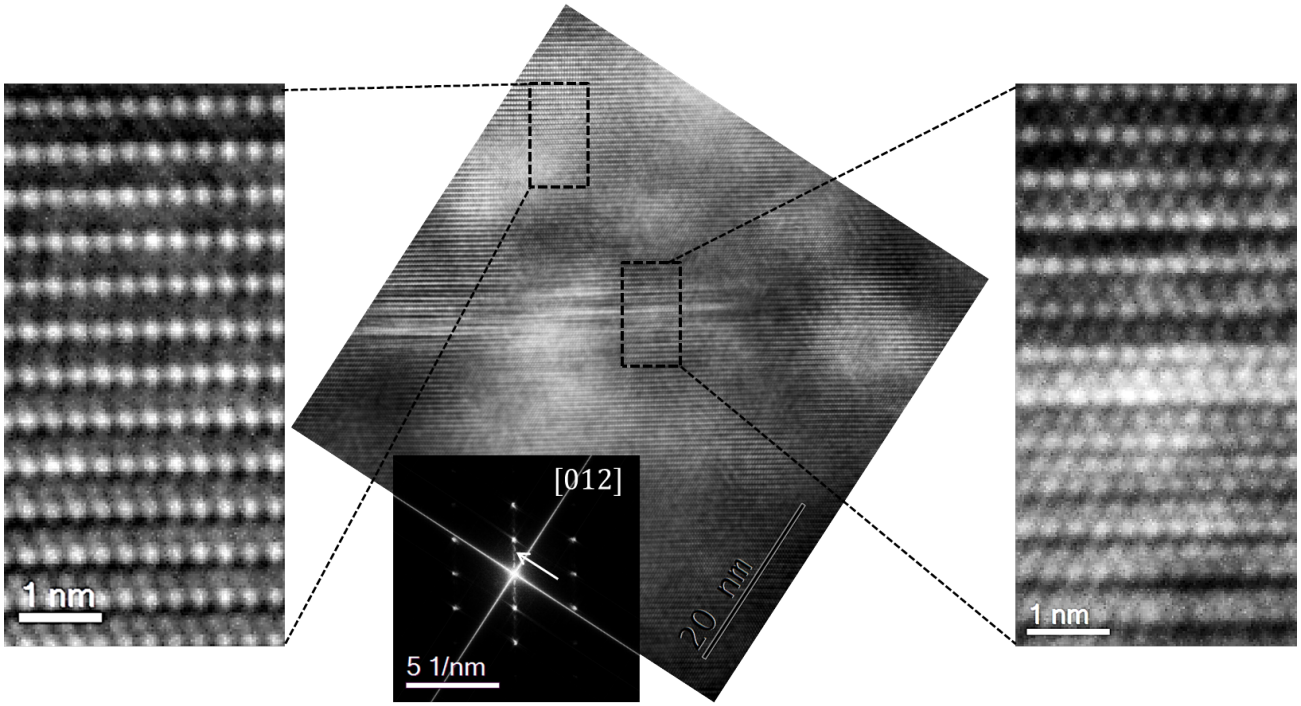

Figure K.4: HRTEM from [012] zone axis with corresponding FFT and magnification of marked areas showing suspected stacking faults

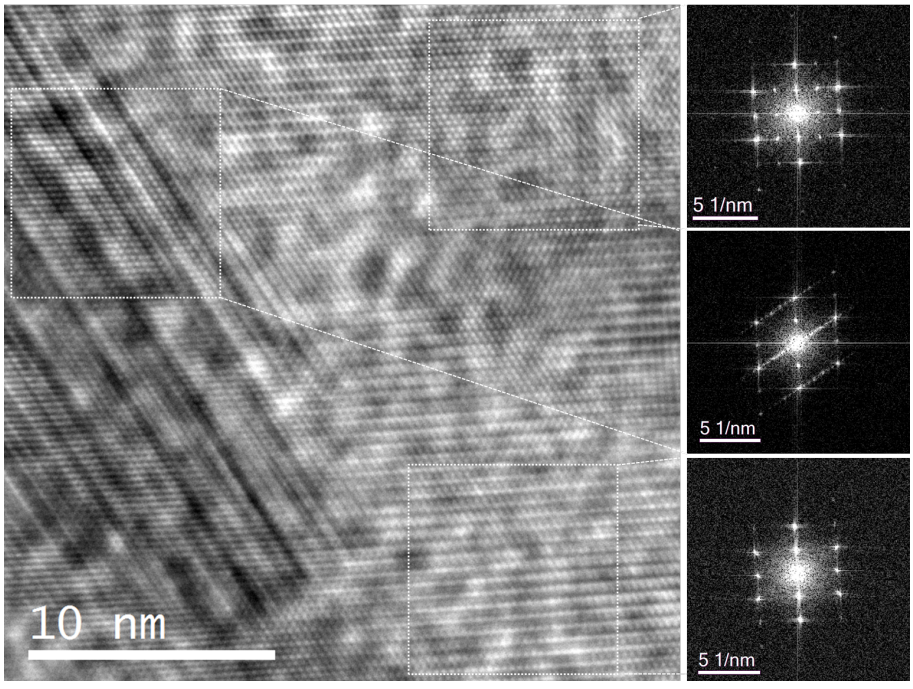

Figure K.5: HRTEM from [012] zone axis with corresponding FFTs showing suspected stacking faults

Appendix L

Image analysis

An estimation of the amount of secondary phase and hence composition, as well as porosity and grain size of main and secondary phase was made from image analysis using imagej [85]. For phase and porosity concentration estimations, the program calculate the area percentage of the image containing contrast up until a chosen threshold. The threshold is chosen by the operator and is therefore highly subjectively and thus quite large uncertainties are associated with the estimation. The program further apply a mask averaging the pixel contrast in the image, before calculating the overall chosen area percentage. The assumptions that the secondary phase and pores are spherical, and that only one Mn exist in main phase unit cell and two in secondary phase unit cell were made. The composition was then found from crystal data from entries in reference [100] presented in table (L.1), by simple calculations. An example of calculation of composition from an analysis with area % of main phase 0.92 and secondary phase of 0.08 is presented as follows

mol Mn in $CaMn_2O_4$ = 2 · area precent $CaMn_2O_4$ · Molar density $CaMn_2O_4$
mol Mn in $CaMn_2O_4$ = 2 ·0.08·2.1542 ·10^{-5} mol/m^3 = 3.5524 10^{-6} mol
mol Mn in $CaMnO_3$ = 1 · area precent $CaMnO_3$ · Molar density $CaMnO_3$
mol Mn in $CaMnO_3$ = 1 ·0.91 ·3.1469 ·10^{-6} = 2.9344 10^{-5} mol

mol Ca in $CaMn_2O_4$ = 1 · area precent $CaMn_2O_4$ · Molar density $CaMn_2O_4$
mol Ca in $CaMn_2O_3$ = 1 ·0.08 · 2.1542 ·10^{-5} mol/m^3 = 1.7762 10^{-6} mol
mol Ca in $CaMnO_3$ = 1 · area precent $CaMnO_3$ · Molar density $CaMnO_3$
mol Ca in $CaMnO_3$ = 1 · 0.91 · 3.1469 ·10^{-6} = 2.9344 10^{-5} mol
Total mol Mn / Total mol Ca = 3.24 · 10^{-4} mol / 3.06 · 10^{-4} mol = 1.06

Which corresponds to a y = 0.06 for $CaMn_{1+y}O_{3-\delta}$.

$CaMnO_3$	
Concentration	4.5 * 0.001 kg/m^3
Molar mass	143 g/mol
Molar density	3.1469 ·10$^-$5 mol/m^3
$CaMn_2O_4$	
Concentration	4.61 * 0.001 kg/m^3
Molar mass	214 g/mol
Molar density	5.1542 ·10$^-$5 mol/m^3

Table L.1: Crystal data obtained from entries in [100]

When finding the average secondary phase particle size, the program identify single particles and calculate the areal of the individual chosen areas. An example from the analysis of CMO_NTNU_3.66 is shown in figure (L.1). Particles located on the edge is disregarded. However, particles which stick together will be regarded as one, and an area which is larger than what is representative for a single particle will be reported. A selection is further done by the operator, disregarding unsuited candidates. This introduces a second subjective selection, thus further uncertainties. The evaluation of average grain size was done by an averaging the distance of random intercept lengths along several vertical lines as described in reference [84].

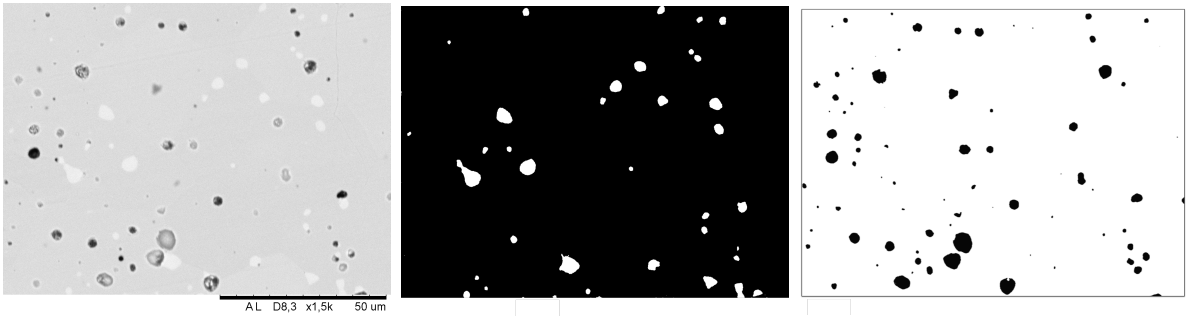

Figure L.1: Basis for image analysis of CMO_NTNU_3.66; original image (left), image with selected secondary phase (middle) and image with selected pores (right), yielding an area % secondary phase of 2.14 and an area % porosity of 2.7.

Appendix M

Precipitate Size Distribution

Rough estimation of particle size distribution of secondary phase in $CaMn_{1+y}O_{3-\delta}$ for y = 3.66 (left) and y = 7.47 (right) for samples synthesised at UiO (top) and NTNU (bottom) from image analysis, figure (M.1).

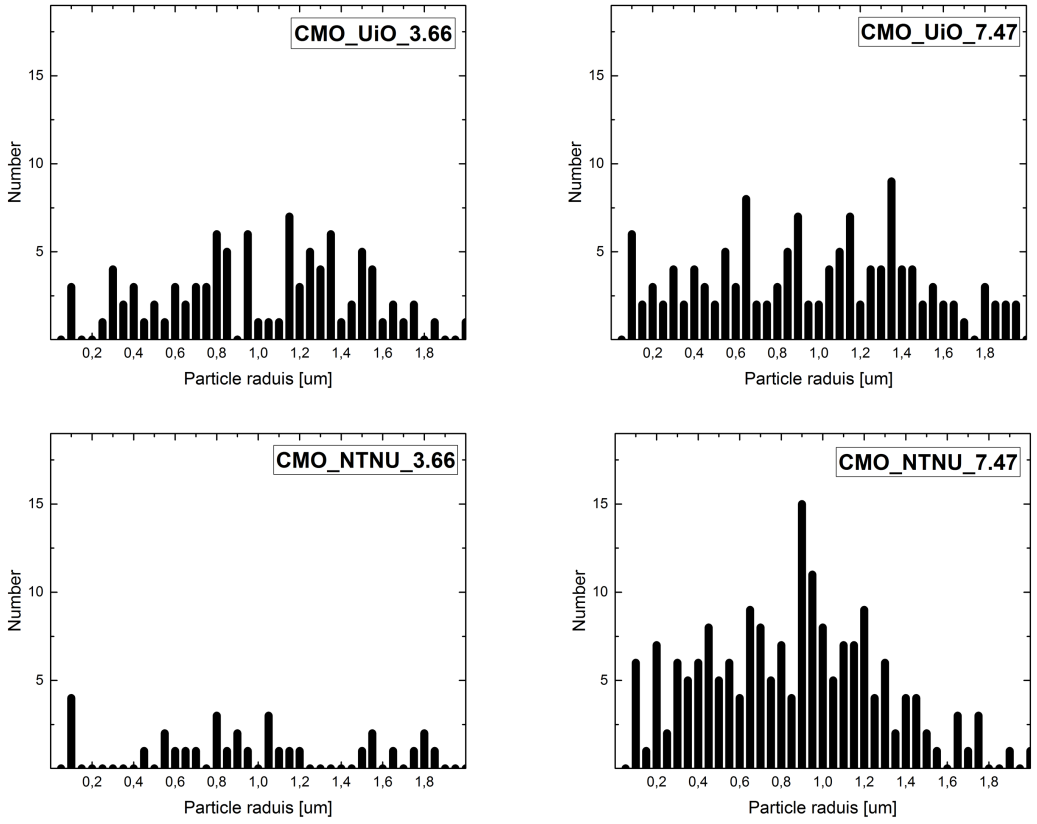

Figure M.1: Size distribution of secondary phase in $CaMn_{1+y}O_{3-\delta}$ for y = 3.66 (left) and y = 7.47 (right) for samples synthesised at UiO (top) and NTNU (bottom).

Appendix N

Calculation of phonon relaxation time

The relaxation time of scattering events in $CaMnO_3$ was calculated following the Callaway model presented in section 2.6.5. For the calculation, several rough approximations were made. The general program was written using matlab and is presented in figure (N.1). A slight modification was made, changing values of T, to calculate the temperature dependence.
For the approximation for speed of sound in the material, the elasticity moduli was approximated from reference [102] and the crystal structure from [100, 103]. The atomic mass and radius were found from SI chemical [104]. The strain parameter used to approximate the impurity scattering was decided as $\epsilon = 10$, through the discussions in reference [105]. The level off defect concentration and crystal size varied. The Gruneisen parameter in the expression for Umklapp scattering, was approximated to $\gamma = 1$ based on the discussion in reference [106]. For the approximation of electron-phonon scattering, the effective mass of an electron, m^*, and the deformation potential, E_{dist}, of the material was decided from discussion in reference [107, 108] and was decided to be 0.36 of the electron mass, while E_{def} to be 2 eV.

```
clear all
x=zeros(50,7);
omega = 1*10^(11);
i = 1;
T=773.15; % Temperature

pi = 3.1416 ; % pi
em0 = 9.10938215*10^(-31) ; % kg - mass of an electron
V = (10.6386*7.4148*5.2093)* ((10^(-10))^3); % volume
N = 3 + 3 + 9; %numbers of atom in unit cell
rho = 4.5800 * 0.001 * (1/0.01^3); % theoretical density
KS = 222*10^(9); % Elastisity modulus

vs = (KS/rho)^(1/2); % speed of sound in CaMnO3

omega_D = (((3*N)/(4*pi*V))^(1/3))*vs; %Debye frequency

kb = 1.3806*10^(-23); % Boltzmanns constant
hbar = 1.0545718 * 10^(-34); %hbar

theta_D = ((hbar*omega_D)/kb) ;%Debye temperautre

MCa = 40.078*0.001 / (6.02214179*10^(23)); %mass Ca
MMn = 54.938*0.001 / (6.02214179*10^(23)); %mass Mn
MO = 15.99*0.001 / (6.02214179*10^(23)); %mass O
m_avA = (1*MCa + 1*MMn + 3*MO)/5; % average mass over all atoms



rCa = 112*10^(-12); % radius Ca
rMn = 64*10^(-12); % radius Mn
rO = 140*10^(-12); % radius O
rAV= (1*rCa+1*rMn+3*rO)/5; % average radius over all atoms


gamma = 1; %gruneisen parameter
Edef = 2 * (1.602176565*10^(-19)); % deformation potential
effm = 0.36 * em0 ; %effective mass of charge carriers in semiconductor
epsilon = 10; % empirical scaling constant for strain variance


%For impurities
impCa = 0; % impurity level Ca
impMn = 0.05; % impurity level Mn
impO = 0; % impurity level O


cCa = 1 - impCa; % consentration of impurity of Ca
cMn = 1- impMn; % consentration of impurity of Mn
cO = 3 - impO; % consentration of impurity of O
Cam_av = cCa*MCa; % average mass in Ca sublattice
Mnm_av = cMn*MMn; % average mass in Mn sublattice
Om_av = cO *MO; % average mass in O sublattice
```

```
Mnr_av = cMn*rMn;

L = 10000 * 10^(-9); %dimension of the crystal


while omega < omega_D
%Umklapp scattering
TuMF = ((hbar * gamma^2 * T) / (m_avA * vs^2 * theta_D)) * (exp((-theta_D)/(3*T))) *
omega^2; %krysset?

%GammaM = ((m_avMn/m_avA)^2 * (cMn * ((MMn - Mnm_av)/Mnm_av)^2)+(cCa * ((MCa - Cam_av)
/Cam_av)^2)+(cO * ((MO - Om_av)/Om_av)^2) )/3 ;
%GammaS = ((m_av/m_avA)^2 * ci * ((rMn - rAV)/rAV)^2)/3 ;%also for first part?

%Impurity scattering
GammaM = ((Mnm_av/m_avA)^2 * ((cMn * ((MMn - Mnm_av)/Mnm_av)^2) +  ((1-cMn) * ((0 -
Mnm_av)/Mnm_av)^2)))/3 ;% mass variance scattering parameter
GammaS = ((Mnm_av/m_avA)^2 * ((cMn * epsilon * ((rMn - Mnr_av)/Mnr_av)^2) + ((1-cMn) *
((0 - Mnr_av)/Mnr_av)^2))) /3 ; % strain variance scattering parameter
TmdMF = ((V/(4 * pi * vs^3)) * (GammaM + GammaS) * omega^4 ) ;

% Electron Phonon
TEPMF = (Edef^2 * effm^2 * omega)/(2 * pi * hbar^3 * rho * vs);



%Boundary scattering
TbMF = vs / L ;

format shortG
TU = 1/TuMF ;
Tmd  = 1/TmdMF ;
Tb = 1/ TbMF ;
TEP = 1/TEPMF;
x(i,1) = omega;
x(i,2) = TU ;
x(i,3) = Tmd;
x(i,4) = Tb;
x(i,5) = TEP;
x(i,6) = TU + Tmd + Tb + TEP;
x(i,7) = T;

i = i + 1;
omega = omega + omega*0.05 ;
end
x
```

Figure N.1: The script written to calculate some relaxation times for phonons in $CaMnO_3$, written in matlab.

Bibliography

[1] R. Zevenhoven and A. Beyene. The relative contribution of waste heat from power plants to global warming. *Energy*, 36(6):3754–3762, 2011.

[2] Alexander S. Rattner and Srinivas Garimella. Energy harvesting, reuse and upgrade to reduce primary energy usage in the USA. *Energy*, 36(10):6172–6183, 2011.

[3] Donna Guillen, Helge Klockow, Matthew Lehar, Sebastian Freund, and Jennifer Jackson. Energy Technology 2011: Carbon Dioxide and Other Greenhouse Gas Reduction Metallurgy and Waste Heat Recovery. *Revista Chilena de Historia Natural*, 60:25–35, 2011.

[4] Thomas Johann Seebeck. *Magnetische Polarisation der Metalle und Erze durch Temperatur-Differenz.* Abhandlungen der Königlichen Akademie der Wissenschaften zu Berlin, 1825.

[5] J. C. Peltier. Nouvelles experiences sur la caloricite des courans electrique. *Annales de Chimie et de Physique*, (56):371–386, 1834.

[6] W Thomson. *On a Mechanical Theory of Thermo-Electric Currents.* Proceedings of the Royal Society of Edinburgh, 3 edition, 1857.

[7] T. Hammel, R. Bennett, and B. Sievers. Evolutionary upgrade for the multi-mission radioisotope thermoelectric generator (mmrtg). In *2016 IEEE Aerospace Conference*, pages 1–8, March 2016.

[8] D M Rowe. Thermoelectrics handbook: macro to nano. *Thermoelectrics Handbook Macro to Nano*, 80(10):1014, 2005.

[9] G Jeffrey Snyder and Eric S Toberer. Complex thermoelectric materials. *Nature materials*, 7(2):105–114, 2008.

[10] Charles Kittel. *Introduction to Solid State Physics, 8th Edition.* John Wiley & Sons, Inc, 2004.

[11] E. Flage-Larsen and Ø. Prytz. The lorenz function: Its properties at optimum thermoelectric figure-of-merit. *Applied Physics Letters*, 99(20):202108, 2011.

[12] Shuo Chen and Zhifeng Ren. Recent progress of half-Heusler for moderate temperature thermoelectric applications. *Materials Today*, 16(10):387–395, 2013.

[13] G. S. Nolas, J. L. Cohn, and G. A. Slack. Effect of partial void filling on the lattice thermal conductivity of skutterudites. *Physical Review B*, 58(1):164–170, 1998.

[14] B C Sales, D Mandrus, and R K Williams. Filled Skutterudite Antimonides: A New Class of Thermoelectric Materials. *Science*, 272(5266):1325–1328, 1996.

[15] Brian C. Sales. Critical overview of recent approaches to improved thermoelectric materials. *International Journal of Applied Ceramic Technology*, 4(4):291–296, 2007.

[16] Woochul Kim, Joshua Zide, Arthur Gossard, Dmitri Klenov, Susanne Stemmer, Ali Shakouri, and Arun Majumdar. Thermal conductivity reduction and thermoelectric figure of merit increase by embedding nanoparticles in crystalline semiconductors. *Physical Review Letters*, 96(4):1–4, 2006.

[17] Kuei Fang Hsu. Bulk Thermoelectric Materials with High Figure of Merit. 818(2004):2000–2004, 2010.

[18] L. D. Hicks and M. S. Dresselhaus. Effect of quantum-well structures on the thermomagnetic figure of merit. *Physical Review B*, 47(19):727–731, 1993.

[19] L. D. Hicks, T. C. Harman, X. Sun, and M. S. Dresselhaus. Experimental study of the effect of quantum-well structures on the thermoelectric figure of merit. *Physical Review B*, 53(16):R10493–R10496, 1996.

[20] Kunihito Koumoto, Ryoji Funahashi, Emmanuel Guilmeau, Yuzuru Miyazaki, Anke Weidenkaff, Yifeng Wang, and Chunlei Wan. Thermoelectric ceramics for energy harvesting. *Journal of the American Ceramic Society*, 96(1):1–23, 2013.

[21] George S. Nolas, Joe Poon, and Mercouri Kanatzidis. Recent Developments in Bulk Thermoelectric Materials. *MRS Bulletin*, 31(March):199–205, 2006.

[22] Kenjiro Fujita, Tadashi Mochida, and Kazuo Nakamura. High-Temperature Thermoelectric Properties of Na x CoO 2-δ Single Crystals. *Japanese Journal of Applied Physics*, 40(Part 1, No. 7):4644–4647, 2001.

[23] Antoine Maignan, Sylvie Hébert, Li Pi, Denis Pelloquin, Christine Martin, Claude Michel, Maryvonne Hervieu, and Bernard Raveau. Perovskite manganites and layered cobaltites: Potential materials for thermoelectric applications. *Crystal Engineering*, 5(3-4 SPEC.):365–382, 2002.

[24] Matthias Schrade, Harald Fjeld, Terje G. Finstad, and Truls Norby. Electronic Transport Properties of $[Ca_2CoO_{3-\delta}]_q$ $[CoO_2]$. *The Journal of Physical Chemistry C*, 118(6):2908–2918, 2014.

[25] I. Terasaki, Y. Sasago, and K. Uchinokura. Large thermoelectric power in $naco_2o_4$ single crystals. *Phys. Rev. B*, 56:R12685–R12687, Nov 1997.

[26] Kunihito Koumoto, Yifeng Wang, Ruizhi Zhang, Atsuko Kosuga, and Ryoji Funahashi. Oxide Thermoelectric Materials: A Nanostructuring Approach. *Annual Review of Materials Research*, 40(1):363–394, 2010.

[27] Kunihito Koumoto, Yifeng Wang, Ruizhi Zhang, Atsuko Kosuga, and Ryoji Funahashi. Oxide Thermoelectric Materials: A Nanostructuring Approach. *Annual Review of Materials Research*, 40(1):363–394, 2010.

[28] A. Weidenkaff, R. Robert, M. Aguirre, L. Bocher, T. Lippert, and S. Canulescu. Development of thermoelectric oxides for renewable energy conversion technologies. *Renewable Energy*, 33(2):342–347, 2008.

[29] Theo Hahn, editor. *International Table for Crystallography*. The International Union of Crystallography, 1983.

[30] Laura Bocher, Myriam H. Aguirre, Rosa Robert, Dmitry Logvinovich, Snejana Bakardjieva, Jiri Hejtmanek, and Anke Weidenkaff. High-temperature stability, structure and thermoelectric properties of CaMn1-xNbxO3 phases. *Acta Materialia*, 57(19):5667–5680, 2009.

[31] Michitaka Ohtaki, Hisako Koga, Tsutomu Tokunaga, Koichi Eguchi, and Hiromichi Arai. Electrical Transport Properties and High-Temperature Thermoelectric Performance of (Ca0.9M0.1)MnO3 (M = Y, La, Ce, Sm, In, Sn, Sb, Pb, Bi), 1995.

[32] Rezaul Kabir, Tianshu Zhang, Danyang Wang, Richard Donelson, Ruoming Tian, Thiam Teck Tan, and Sean Li. Improvement in the thermoelectric properties of CaMnO3 perovskites by W doping. *Journal of Materials Science*, 49(21):7522–7528, 2014.

[33] Nathan Galinsky, Marwan Sendi, Lindsay Bowers, and Fanxing Li. $CaMn_{1-x}B_xO_{3-\delta}$ (B = Al, V, Fe, Co, and Ni) perovskite based oxygen carriers for chemical looping with oxygen uncoupling (CLOU). *Applied Energy*, 174:80–87, 2016.

[34] Philipp Thiel, Sascha Populoh, Songhak Yoon, Gesine Saucke, Kristaps Rubenis, and Anke Weidenkaff. Charge-Carrier Hopping in Highly Conductive $CaMn_{1-x}O_{3-\delta}$ Thermoelectrics. *The Journal of Physical Chemistry C*, 119(38):21860–21867, 2015.

[35] L. Bocher, M. H. Aguirre, D. Logvinovich, A. Shkabko, R. Robert, M. Trottmann, and A. Weidenkaff. CaMn 1 - x Nb x O 3 (x $\leq$ 0.08) Perovskite-Type Phases As Promising New High-Temperature n -Type Thermoelectric Materials. *Inorganic Chemistry*, 47(18):8077–8085, 2008.

[36] Ayelet Graff and Yaron Amouyal. Effects of Lattice Defects and Niobium Doping on Thermoelectric Properties of Calcium Manganate Compounds for Energy Harvesting Applications. *Journal of Electronic Materials*, 45(3):1508–1516, 2016.

[37] Ayelet Graff and Yaron Amouyal. Reduced thermal conductivity in niobium-doped calcium-manganate compounds for thermoelectric applications. *Applied Physics Letters*, 105(18):2012–2017, 2014.

[38] M. Schrade, R. Kabir, S. Li, T. Norby, and T. G. Finstad. High temperature transport properties of thermoelectric $CaMnO3 - \delta$ - Indication of strongly interacting small polarons. *Journal of Applied Physics*, 115(10):0–7, 2014.

[39] Ekaterina V. Tsipis and Vladislav V. Kharton. Electrode materials and reaction mechanisms in solid oxide fuel cells: A brief review : I Performance-determining factors. *Journal of Solid State Electrochemistry*, 12(9):1039–1060, 2008.

[40] C. B. Alcock, R. C. Doshi, and Y. Shen. Perovskite electrodes for sensors. *Solid State Ionics*, 51(3-4):281–289, 1992.

[41] Henrik Leion, Yngve Larring, Egil Bakken, Rune Bredesen, Tobias Mattisson, and Anders Lyngfelt. Use of CaMn0.875Ti0.125O3 as oxygen carrier in chemical-looping with oxygen uncoupling. *Energy and Fuels*, 23(10):5276–5283, 2009.

[42] U. Balachandran, J. T. Dusek, R. L. Mieville, R. B. Poeppel, M. S. Kleefisch, S. Pei, T. P. Kobylinski, C. A. Udovich, and A. C. Bose. Dense ceramic membranes for partial oxidation of methane to syngas. *Applied Catalysis A, General*, 133(1):19–29, 1995.

[43] E Goldyreva, I Leonidov, M Patrakeev, and J Kozhevnikov. Oxygen non-stoichiometry and defect equlibria in CaMnO3 - δ. *Solid State Electrochemestry*, 16(3):1187–1191, 2012.

[44] K. Vijayanandhini and T. R N Kutty. Phase conversions in calcium manganites with changing Ca/Mn ratios and their influence on the electrical transport properties. *Journal of Materials Science: Materials in Electronics*, 20(5):445–454, 2009.

[45] Philippe Ghosez and Jean-marc Triscone. Multiferroics: Coupling of three lattice instabilities. *Nature materials*, 10(4):269–270, 2011.

[46] A. Baranovskiy and Y. Amouyal. Structural stability of calcium-manganate based CaO(CaMnO3)m (m = 1, 2, 3, inf) compounds for thermoelectric applications. *Journal of Alloys and Compounds*, 687:562–569, 2016.

[47] Hsin Wang, Wallace D. Porter, Harald Böttner, Jan König, Lidong Chen, Shengqiang Bai, Terry M. Tritt, Alex Mayolet, Jayantha Senawiratne, Charlene Smith, Fred Harris, Patricia Gilbert, Jeff Sharp, Jason Lo, Holger Kleinke, and Laszlo Kiss. Transport properties of bulk thermoelectrics: An international round-robin study, part II: Thermal diffusivity, specific heat, and thermal conductivity. *Journal of Electronic Materials*, 42(6):1073–1084, 2013.

[48] Han Li, Xinfeng Tang, Qingjie Zhang, and Ctirad Uher. High performance InxCeyCo4Sb12 thermoelectric materials with in situ forming nanostructured InSb phase. *Applied Physics Letters*, 94(10):92–95, 2009.

[49] Yucheng Lan, Bed Poudel, Yi Ma, Dezhi Wang, Mildred S. Dresselhaus, Gang Chen, and Zhifeng Ren. Structure study of bulk nanograined thermoelectric bismuth antimony telluride. *Nano Letters*, 9(4):1419–1422, 2009.

[50] Yanzhong Pei, Nicholas a. Heinz, Aaron LaLonde, and G. Jeffrey Snyder. Combination of large nanostructures and complex band structure for high performance thermoelectric lead telluride. *Energy & Environmental Science*, 4(9):3640, 2011.

[51] C Cardoso, R P Borges, T Gasche, and M Godinho. *Ab-initio* calculations of the ruddlesden–popper phases camno$_3$, cao(camno $_3$) and cao(camno$_3$)$_2$,. *Journal of Physics: Condensed Matter*, (3):035202, 2008.

[52] M. Tokonami and H. Horiuchi. On the space group of spinel, MgAl 2 O 4. *Acta Crystallographica Section A*, 36(1):122–126, 1980.

[53] Brent Fultz and James M. Howe. *Transmission electron microscopy and diffractometry of materials.* 2008.

[54] Richard J. D. Tilley. *Understanding Solids: The Science of Materials, 2nd ed.* John Wiley & Sons Ltd, 2013.

[55] Truls Norby. Defects and transport in crystalline materials. 2016.

[56] F. a. Kröger and H. J. Vink. Relations between the Concentrations of Imperfactions in Crystalline Solids. *Solid State Physics*, 3(I):310–435, 1956.

[57] Lisbeth Rørmark, Kjell Wiik, Svein Stølen, and Tor Grande. Oxygen stoichiometry and structural properties of La1 – xAxMnO3 ± δ (A = Ca or Sr and $0 \leq x \leq 1$). *Journal of Materials Chemistry*, 12:1058–1067, 2002.

[58] Terry M. Tritt. *Thermal Conductivity.* 2004.

[59] Joseph Fourier. Theorie analytique de la chaleur, 1822.

[60] A. Einstein. Die Plancksche Theorie der Strahlung und die Theorie der spezifischen Wärme, 1906.

[61] P. Debye. Zur Theorie der spezifischen Wärmen. *Annalen der Physik*, 344(14):789–839, 1912.

[62] J. Callaway. Model for lattice Thermal Conductivity at Low Temperatures. *Physical Review*, 113(4):1046–1051, 1959.

[63] M. Holland. Analysis of Lattice Thermal Conductivity. *Physical Review*, 132(6):2461–2471, 1963.

[64] D. T. Morelli, J. P. Heremans, and G. A. Slack. Estimation of the isotope effect on the lattice thermal conductivity of group IV and group III-V semiconductors. *Physical Review B - Condensed Matter and Materials Physics*, 66(19):1953041–1953049, 2002.

[65] N. Mingo. Calculation of Si nanowire thermal conductivity using complete phonon dispersion relations. *Physical Review B*, 68(11):113308, 2003.

[66] P. Chantrenne, J. L. Barrat, X. Blase, and J. D. Gale. An analytical model for the thermal conductivity of silicon nanostructures. *Journal of Applied Physics*, 97(10), 2005.

[67] M. Kazan, G. Guisbiers, S. Pereira, M. R. Correia, P. Masri, A. Bruyant, S. Volz, and P. Royer. Thermal conductivity of silicon bulk and nanowires: Effects of isotopic composition, phonon confinement, and surface roughness. *Journal of Applied Physics*, 107(8), 2010.

[68] A. Ward and D. A. Broido. Intrinsic phonon relaxation times from first-principles studies of the thermal conductivities of Si and Ge. *Physical Review B*, 81(8):085205, 2010.

[69] P. G. Klemens. The Thermal Conductivity of Dielectric Solids at Low Temperatures (Theoretical). *The Royal Society London A*, 1951.

[70] P G Klemens. The Scattering of Low-Frequency Lattice Waves by Static Imperfections. *Proceedings of the Physical Society. Section A*, 68(12):1113–1128, 1955.

[71] H.B.G. B G Casimir. Note on the conduction of heat in crystals. *Physica*, 5(6):495–500, 1938.

[72] AI Hochbaum, Renkun Chen, and RD Delgado. Enhanced thermoelectric performance of rough silicon nanowires. *Nature*, 451(7175):163–167, 2008.

[73] John M. Ziman. *Electrons and phonons : the theory of transport phenomena in solids.* Clarendon Press, 2001.

[74] James G. Berryman. Thermal conductivity of porous media. *Applied Physics Letters*, 86(3):1–3, 2005.

[75] K. W. Schlichting, N. P. Padture, and P. G. Klemens. Thermal conductivity of dense and porous yttria-stabilized zirconia. *Journal of Materials Science*, 36(12):3003–3010, 2001.

[76] Boris Shafiro and Mark L. Kachanov. Anisotropic effective conductivity of materials with nonrandomly oriented inclusions of diverse ellipsoidal shapes. *Journal of Applied Physics*, 87(12):8561–8569, 2000.

[77] J. C. Maxwell. *A treatise on electricity and magnetism.* Clarendon Press, Oxford, 1904.

[78] P. G. Klemens. Thermal conductivity of inhomogeneous media. *High Temp. High Pressures*, 23(6):241, 1991.

[79] H. Szelagowski, I. Arvanitidis, and S. Seetharaman. Effective thermal conductivity of porous strontium oxide and strontium carbonate samples. *Journal of Applied Physics*, 85(1):193–198, 1999.

[80] Igor Sevostianov. Thermal conductivity of a material containing cracks of arbitrary shape. *International Journal of Engineering Science*, 44(8-9):513–528, 2006.

[81] Mark Kachanov and Igor Sevostianov. On quantitative characterization of microstructures and effective properties. *International Journal of Solids and Structures*, 42(2):309–336, 2005.

[82] M. Kachanov, I. Sevostianov, and B. Shafiro. Explicit cross-property correlations for porous materials with anisotropic microstructures. *Journal of the Mechanics and Physics of Solids*, 49(1):1–25, 2001.

[83] David B Williams and C Barry Carter. *Transmission Electron Microscopy*. 2009.

[84] David Brandon and Wayne D. Kaplan. *Microstructural Characterization of Materials, 2nd Edition*. John Wiley & Sons, Ltd, 2008.

[85] Rueden C. T. & Hiner M. C. Schindelin, J. The ImageJ ecosystem: An open platform for biomedical image analysis. *Molecular Reproduction and Development*, 2015.

[86] Miloslav Klinger and Aleš Jäger. Crystallographic Tool Box (CrysTBox): Automated tools for transmission electron microscopists and crystallographers. *Journal of Applied Crystallography*, 48(2015):2012–2018, 2015.

[87] Matthias Schrade, Harald Fjeld, Truls Norby, and Terje G. Finstad. Versatile apparatus for thermoelectric characterization of oxides at high temperatures. *Review of Scientific Instruments*, 85(10), 2014.

[88] Truls Norby. EMF method determination of conductivity contributions from protons and other foreign ions in oxides. *Solid State Ionics*, 28-30(PART 2):1586–1591, 1988.

[89] L J van der Pauw. A method of measuring the resistivity and hall coefficient of discs of arbitrary shape. *Philips Research Reports*, 13(1):1–9, 1958.

[90] W. J. Parker, R. J. Jenkins, C. P. Butler, and G. L. Abbott. Flash method of determining thermal diffusivity, heat capacity, and thermal conductivity. *Journal of Applied Physics*, 32(9):1679–1684, 1961.

[91] International Centre for Diffraction Data (ICDD). 2016.

[92] NETZSCH. Laser flash apparatus lfa457 *MicroFlash* - catalogue.

[93] Kasper A Borup, Johannes De Boor, Heng Wang, Fivos Drymiotis, Bo B Iversen, and G Je. Environmental Science Measuring thermoelectric transport properties of materials. pages 423–435, 2015.

[94] G. B. Ansell, M. A. Modrick, J. M. Longo, K. R. Poeppeimeler, and H. S. Horowitz. Structure of calcium manganese oxide $Ca_2Mn_3O_8$. *Acta Crystallographica Section B*, 38(6):1795–1797, Jun 1982.

[95] Ekaterina I. Goldyreva, Ilya A. Leonidov, Mikhail V. Patrakeev, and Victor L. Kozhevnikov. Temperature activated electron transport in CaMnO3. *Solid State Ionics*, 262:678–681, 2014.

[96] D. Platzek, G. Karpinski, C Stiewe, and E Muller. Potential-seebeck-microprobe psm: Measuring the spatial resolution of the seebeck coefficient and the electric potential. *Conference Paper, Thermoelectrics 2005, ICT 2005, 24th*, 2005.

[97] E. Alleno, D. Bérardan, C. Byl, C. Candolfi, R. Daou, R. Decourt, E. Guilmeau, S. Hébert, J. Hejtmanek, B. Lenoir, P. Masschelein, V. Ohorodnichuk, M. Pollet, S. Populoh, D. Ravot, O. Rouleau, and M. Soulier. Invited article: A round robin test of the uncertainty on the measurement of the thermoelectric dimensionless figure of merit of co0.97ni0.03sb3. *Review of Scientific Instruments*, 86(1):011301, 2015.

[98] Yang Wang, Yu Sui, Xianjie Wang, and Wenhui Su. Effects of substituting La3+, Y3+ and Ce4+ for Ca2+ on the high temperature transport and thermoelectric properties of CaMnO3. *Journal Of Physics D-Applied Physics*, 42(5):55010, 2009.

[99] H.S. Horowitz and J.M. Longo. Phase relations in the $camno_3$ system. *Materials Research Bulletin*, 13(12):1359 – 1369, 1978.

[100] P. Villars and K. Cenzual. Pearson's Crystal Data: Crystal Structure Database for Inorganic Compounds, Release 2016/17, ASM International, Materials Park, Ohio, USA.

[101] R. Sayers, N. L. O. Flack, J. Alaria, P. A. Chater, R. G. Palgrave, S. R. C. McMitchell, S. Romani, Q. M. Ramasse, T. J. Pennycook, and M. J. Rosseinsky. Epitaxial growth and enhanced conductivity of an it-sofc cathode based on a complex perovskite superstructure with six distinct cation sites. *Chem. Sci.*, 4:2403–2412, 2013.

[102] A.S. Verma. Elastic moduli of orthorhombic perovskites. *Solid State Communications*, 158:34 – 37, 2013.

[103] K. R. Poeppelmeier, M. E. Leonowicz, J. C. Scanlon, J. M. Longo, and W. B. Longo. Structure determination of $CaMnO_3$ and CaMnO_{2.5} by X-Ray and Neutron methods. *J. Solid State Chem.*, 45:71–79, 1982.

[104] G. H. Aylward and T. J. V. Findlay. *SI Chemical Data, 6th Edition*. John Wiley & Sons, Ltd, 2007.

[105] J. Yang, G. P. Meisner, and L. Chen. Strain field fluctuation effects on lattice thermal conductivity of zrnisn-based thermoelectric compounds. *Applied Physics Letters*, 85(7):1140–1142, 2004.

[106] Hanhui Xie, Heng Wang, Yanzhong Pei, Chenguang Fu, Xiaohua Liu, G. Jeffrey Snyder, Xinbing Zhao, and Tiejun Zhu. Beneficial contribution of alloy disorder to electron and phonon transport in half-heusler thermoelectric materials. *Advanced Functional Materials*, 23(41):5123–5130, 2013.

[107] Christian A. Niedermeier, Sneha Rhode, Keisuke Ide, Hidenori Hiramatsu, Hideo Hosono, Toshio Kamiya, and Michelle A. Moram. Electron effective mass and mobility limits in degenerate perovskite stannate $basno_3$. *Phys. Rev. B*, 95:161202, Apr 2017.

[108] Orson L. Anderson. Thermoelastic properties of mgsio 3 perovskite using the debye approach. *American Mineralogist*, 83(1-2):23–35, 1998.